University of Crete

Department of Material Science and Technology

Optical systems for imaging ultra-cold atoms

Thesis submitted in partial fulfillment of the requirements for the

Master of Science

Mylonakis Mikis

Supervising Committee

Dimitris G. Papazoglou

Assistant Professor, Department of Materials Science and Technology, UoC

Wolf von Klitzing

Cretan Matter Waves research group leader, IESL-FORTH

Peter Rakitzis

Associate Professor, Department of Physics, UoC

Abstract

This master thesis focuses on the optimization of optical systems that image ultra-cold and quantum degenerate atomic cloud (including Bose-Einstein condensates). Two independent optical systems, exploiting different imaging approaches, were designed and tested both in the optical and in the opto-mechanical level. The first optical system employs absorption and fluorescence imaging of small cold atomic clouds, while the second uses an innovative, non-destructive method, based on Faraday's non-destructive optical rotation, capable of measuring the number of atoms in an ultra-cold atomic cloud. A main goal of the thesis was to extend the resolution and field of view of such optical systems. In this perspective, various optical design techniques are analyzed taking into account optical aberrations by the various components of the experimental device. An important result of this analysis was the introduction of a novel, and counterintuitive, analytic optical design approach, where a flat glass plate can be used to cancel out the spherical aberrations introduced by the glass windows used to optically access the of the vacuum cell where BECs are generated. The optical design and optimization process was performed by using commercial raytracing software (ZEMAX). The opto-mechanical design was performed using CAD software (Inventor Autodesk).

The optimized optical systems were designed to use commercially available optical components. The first system exhibits excellent diffraction-limited optical performance at the maximal possible photon collection efficiency for the specific experimental configuration. The second optical system is designed to optimally extract the atom number information from the cloud, by optimizing the light-atom Faraday interaction and recording with minimal losses the probe light.

Περίληψη

Η παρούσα μεταπτυχιακή εργασία επικεντρώνεται στη βελτιστοποίηση οπτικών συστημάτων που απεικονίζουν υπερ-ψυχρά ατομικά νέφη, συμπεριλαμβανομένων των συμπυκνωμάτων Bose- Einstein(BEC) . Δύο ανεξάρτητα οπτικά συστήματα, αξιοποιώντας διαφορετικές προσεγγίσεις απεικόνισης, σχεδιάστηκαν και ελέγχθηκαν τόσο στο οπτικό όσο και στο οπτικο-μηχανικό επίπεδο. Το πρώτο οπτικό σύστημα είναι ικανό για απεικόνιση απορρόφησης και φθορισμού των υπερ-ψυχρών ατομικών νεφών ενώ το δεύτερο χρησιμοποιεί μια καινοτόμο, μη καταστροφική μέθοδο απεικόνισης, βασισμένη στην μη καταστρεπτική οπτική περιστροφή του Faraday, ικανή να μετρά τον αριθμό των ατόμων σε ένα υπερ-ψυχρό ατομικό σύννεφο. Ένας κύριος στόχος της διατριβής ήταν να επεκταθεί η διακριτική ικανότητα και το οπτικό πεδίο θέασης τέτοιων οπτικών συστημάτων. Από την άποψη αυτή, αναλύονται διάφορες τεχνικές οπτικού σχεδιασμού, λαμβάνοντας υπόψη τις οπτικές εκτροπές που εισάγονται από τα διάφορα μέρη της πειραματικής διάταξης. Ένα σημαντικό αποτέλεσμα αυτής της ανάλυσης ήταν η εισαγωγή μιας νέας προσέγγισης οπτικής σχεδίασης, όπου μπορεί να χρησιμοποιηθεί μια επίπεδη γυάλινη πλάκα για την εξουδετέρωση των σφαιρικών εκτροπών που εισάγονται από τα γυάλινα παράθυρα που χρησιμοποιούνται για την οπτική πρόσβαση στο κελί κενού όπου τα BECs δημιουργούνται. Η διαδικασία οπτικής σχεδίασης και βελτιστοποίησης εκτελέστηκε χρησιμοποιώντας το εμπορικό λογισμικό raytracing (ZEMAX). Ο οπτικο-μηχανικός σχεδιασμός εκτελέστηκε χρησιμοποιώντας το λογισμικό CAD (Inventor Autodesk).

Τα βελτιστοποιημένα οπτικά συστήματα σχεδιάστηκαν χρησιμοποιώντας εμπορικά διαθέσιμα οπτικά στοιχεία. Το πρώτο σύστημα παρουσιάζει βέλτιστη οπτική απόδοση, δεδομένου ότι είναι σχεδιασμένο να φτάνει το όριο περίθλασης ενώ παράλληλα επιτυγχάνει τη μέγιστη ικανότητα συλλογής φωτονίων για τη συγκεκριμένη πειραματική διάταξη. Το δεύτερο οπτικό σύστημα έχει σχεδιαστεί για να εξάγει κατά βέλτιστο τρόπο την πληροφορία του αριθμού ατόμων από το σύννεφο, βελτιστοποιώντας την αλληλεπίδραση Faraday μεταξύ φωτός-ατόμων και ανιχνεύοντας με ελάχιστες απώλειες το επισκοπικό φως.

Acknowledgements

I would like to thank the supervising professor, but most of all my teacher, Dimitris Papazoulou for the excellent guidance he provided to me during this thesis. I am grateful for the time he spent, the knowledge he wanted to share with me, and the patience he showed to me.

I would also like to express my thanks to Dr. Wolf von Klitzing who gave me the opportunity to work in a high-level working environment. He really taught me a lot of things and his well-intentioned criticism helped me greatly in completing the project.

I would also like to thank Professor Petros Rakitzis, who accepted to be a member of the three-member committee for the examination of this dissertation.

In addition, I want to thank all the members of the BEC lab for the excellent collaboration we had. Everybody helped me in their own way. In particular, I thank G. Drougakis, K. Mavrakis, S. Pandey, V. Bolpasi, H. Maas. I especially thank Premjith Thekkeppatt for his significant contribution to the project.

The curiosity of what is happening around me and how it can be explained was something I remember to characterize me from my very young age.

My family and friends not only did not try to suppress this feature (which was sometimes proved to be dangerous), but on the contrary they cultivated in many ways this feature in me and made it evolve and mature in me and around me. They supported me all those years in many ways.

Nothing would have been accomplished, if I had no great teachers. Fortunately, I had many, and I can see their figures or shadows from the side banks shedding light like lanterns all the time.

I thank my family very much for their support and patience, but basically because they made the delicate-difficult years easy.

I am particularly thankful to Petros Lyberakis for all that he has shown and taught me in life, and also for the special and substantive relationship that we have.

I thank Angelos Pothoulakis as one of the most honest and authentic personalities I have ever met in my life. The influence he exerted on me through our disputes has been decisive in my path. He was and still is a hidden hero.

I thank very much my friends Odysseus, Giorgos, Manolis. The times we were hanging out, what we said, what we saw, what we thought played a very important role in achieving the goal, this one and the others.

Finally, special thanks go to Giorgos Vasilakis. His patience, his knowledge and his eagerness to transfer it to me were decisive factors for the completion of this dissertation. I would also like to thank this true friend of mine for what we have discussed and analyzed in our quest for the essence.

This thesis is dedicated to Petros Lyberakis.

« Ξανά πολυσκοτίστηκες για να προκαταβάλεις τους φόβους που εξαγόραζες μοχθώντας μια ζωή· μάθε πώς κάθε ποταμός μονάχα όταν εκβάλλει θωρεί για πού ξεκίνησε σα βγήκε απ' την πηγή.»

Άγγελος Ποθουλάκης, *Κύκλος ,ανοιχτός*

Table of Contents

Introduction

Since their first observation in 1995[1] Bose–Einstein condensates have been used as powerful tool to study novel physics. Cold atoms and in particular Bose-Einstein condensates form a clean and well controlled system for studying many-body quantum phenomena [2]. In addition, ultra-cold atoms have shown great potential for both technological and fundamental science applications. For instance, precise time keeping is currently based on cold atoms. Further areas of scientific endeavour that will profit from advances in ultra-cold atom technology are gyroscopes, telecommunications, gravimeters, tests of relativity and gravitational-wave detectors.

To fully exploit the potential of cold-atom physics, it is essential to develop precise, low noise and high-resolution imaging techniques. In the majority of the performed measurements with ultra-cold atoms the information to be extracted from the system is encoded ultimately in images of the atomic density distribution. High resolution imaging also plays a key role for creating complex optical potentials for quantum gas studies [3], [4], [5] and in particular for trapping and imaging single atoms[6],[7],[8],[9].

The goal of this thesis is to develop techniques that optimize, from the optical design perspective, the imaging experiments performed in the Cretan Matter-Waves group. The development goes in two directions: we improve the optical resolution that can be achieved with absorption/fluorescence imaging whilst maximizing the collection efficiency in fluorescence experiments. Furthermore, we introduce a new minimally-destructive technique for measuring the atom number.

In the first chapter, we describe the basic theoretical background for designing an optical system. In the second chapter we describe the optical and the opto-mechanical design process of the two optical systems developed and we study their performance. Finally, at the last chapter we summarize the results of the thesis and provide an outlook.

1 Theory

1.1 BEC Imaging

1.1.1 Existing imaging techniques

Several imaging techniques based on light-atom interaction have been developed in order to extract useful information about cold atoms. These imaging techniques can be divided in two main categories depending on the effect on the atomic cloud [10]. The first category includes imaging techniques that destroy the quantum state of the atomic cloud. These techniques are based on the absorption of resonant light from the atoms. This interaction localizes the atoms to the resolution of the optical system and thus destroys any coherence the atomic ensemble used to have. The most common destructive imaging techniques are for cold atoms experiments: light absorption [11], resonant diffractive dark-ground imaging [12] and atomic cloud fluorescence imaging[13]. In the second category, the imaging techniques are minimally destructive to the atomic state and have negligible effect on the temperature. These are based on the dispersive interaction of the atomic ensemble with off-resonant light: the refractive index of the atoms induces a phase change in the probe light, which is then detected by converting into measurable intensity modulation. These techniques include dark field [14] and phase contrast imaging [15]. Both are well-known in microscopy and utilize a mask in the Fourier imaging plane to either block or phase shift respectively the part of light that has not interacted with the atoms. Minimally destructive imaging techniques for cold atoms have also been developed based on the anisotropic response of different magnetic atomic levels, which results in changes in the polarization state of the probe light [16],[17].

Absorption imaging

The most common imaging technique used in any cold atom laboratory is absorption imagin of the photons of the probe beam is absorbed by the atomic cloud there is a dip in the collected intensity signal on the CCD sensor as it is described by the equation below. :

$$T = \frac{1+\delta^2}{s_0} W\left[\frac{s_0}{1+\delta^2}\exp\left(\frac{s_0 - n\sigma_0}{1+\delta^2}\right)\right] \quad (1)$$

where, $T=I_T/I_0$ is the transmittance, I_0 is the initial intensity and I_T the transmitted intensity, W is the first kind Lambert function [12],δ =(f-f$_0$)/Δf is the detuning of the probe laser (frequency f) from resonance (at frequency f_0) normalized with the half-width at half maximum linewidth Δf of the transition, s_0 is the saturation parameter, n is the atomic density and σ_0 is the resonant cross-section at law saturation parameters.[12] .

1.1.2 Polarized light-atomic cloud interactions

The estimation of the atomic number is based on the Faraday paramagnetic effect [17]. When off-resonant, linearly polarized light is travelling through an atomic ensemble, it experiences an optical rotation; where the angle of rotation is proportional to the total spin component along the direction of light propagation. For an ensemble of atoms with well-defined spin state, as is typically the case in magnetic traps [18], the total spin is proportional to the number of atoms, so that the rotation of light polarization reflects the total number of atoms.

On a quantitative level, the Hamiltonian that describes the interaction between off-resonant light and an atomic ensemble, in the low saturation regime, is given by[19] :

$$\hat{H} = \alpha_1 \hat{S}_3 \hat{F}_z, \quad (2)$$

where α_1 is the vector (first rank) polarizability, $\hat{S}_3$ is the Stokes component that measures the degree of circular polarization and the operator $\hat{F}_z = \sum_{i=1}^{N_{at}} \hat{f}_{z,i}$

describes the sum of all atomic spins $\hat{f}_{z,i}$ in the z direction of light propagation. In writing Eq. 2 we neglected the second rank tensor part of the Hamiltonian, which is typically $\frac{\Delta_{hf,exc}}{\Delta}$ times smaller than the vector part, where $\Delta_{hf,exc}$ and Δ are the hyperfine splitting in the excited atomic state and the detuning of light from the atomic resonance respectively. We also did not include the contribution of scalar (zero rank) polarizability to the Hamiltonian, since this is zero (for the polarization evolution) due to the fact that it does not affect the polarization state of the probe light.

As a result of the interaction described by Eq.2 the probe light experiences optical rotation which is given by: $\phi = \frac{1}{2}\alpha_1 F_z$. When all atoms in the ensemble are in the same m_F spin eigenstate then the optical rotation is directly proportional to the number of atoms:

$$\phi = \frac{1}{2}\alpha_1 m_F N_{at}. \tag{3}$$

with the vector polarizability:

$$\alpha_1 = \frac{\Gamma}{8A\Delta}\frac{\lambda^2}{2\pi}\tilde{a}_1, \tag{4}$$

where Γ is the spontaneous emission rate, A is the area of interaction, λ is the light wavelength, and $\tilde{\alpha}_1$ is a number of order unity (originating from the fact that the atoms have an excited state structure with different hyperfine levels) that has a small dependence on the detuning Δ. From Eqs. 3 and 4 we find:

$$\phi = \frac{\Gamma}{16A\Delta}\frac{\lambda^2}{2\pi}\tilde{a}_1 m_F N_{at} = \frac{\Gamma}{16\Delta}\tilde{a}_1 m_F \sigma_0 nL, \tag{5}$$

where $\sigma_0 = \frac{\lambda^2}{2\pi}$ is the cross section on resonance, n is the atomic density, and L is the length of the ensemble in the direction of light propagation.

Before proceeding, we emphasize that the m_F describes the spin projection along the quantization axis of the probe light propagation: $m_F = \vec{F} \cdot \hat{z}$, where $\vec{F}$ is the spin vector. If the spin dynamics are such so that the z projection of $\vec{F}$ is changing in time then the optical rotation signal is also changing in time.

Alternatively, the Faraday rotation can be explained [20] by the difference in refractive indices for right and left circularly polarized light when travelling through a spin polarized medium. Linearly polarized light can be thought as a superposition of left and right circularly polarized light, whose relative phase difference is determined by the polarization axis of the light. As the light travels through an atomic spin ensemble (with an inhomogeneous population distribution among the magnetic m_f states), the left and right circular components experience different refractive indices and therefore acquire an additional relative phase shift, which is manifested as optical rotation.

We can detect the optical rotation of light using the balanced polarimeter scheme: light goes through an analyzing polarizer at 45° with respect to the incoming polarization axis of light before the interaction with the atoms. Two photodiodes detect the power of the analyzed beams and the signal is taken as the difference of the two photodiodes. It can be shown (using for instance the Jones matrix algebra) that the measured signal is given by:

$$\Phi_0 \sin(2\phi) \approx 2\Phi_0 \phi, \tag{6}$$

where Φ_0 is the photon flux of the incoming light and the approximation holds for small angles, which is typically the case for the atomic densities and sizes that can be achieved in the lab.

In the experiment under consideration, a Gaussian light beam interacts with an atomic ensemble of spatially inhomogeneous density determined by temperature and the trapping potential. In this case Eqs. 5 and 6 should be modified to take into account the spatial variation of the atomic density and the light power, so that the measured signal is proportional to the integral: $\int d\vec{r}\, n(\vec{r}) I(\vec{r})$, where $I(\vec{r})$ is the intensity of light. For the case of a Gaussian beam

with waist w, a harmonic trap with frequencies $\omega_x, \omega_y, \omega_z$ in the three Cartesian directions, and thermal atomic temperature T the integral takes the form:

$$S = \frac{2\Phi_0 N_{at}}{\pi\sqrt{\left(\frac{4k_B T}{m\omega_x^2} + w^2\right)\left(\frac{4k_B T}{m\omega_y^2} + w^2\right)}} \quad , \tag{7}$$

where k_B is the Boltzmann constant and we assumed ideal gas density distribution with no Bosonic enhancement.

The atoms are confined in a magnetic Time Orbiting Potential trap (TOP) [21], formed by a static quadrupole field $\vec{B}_q$ and a quasi-static field $\vec{B}_T(t)$ that is rotating slowly (typically on the order of a few kHz) with respect to the Larmor frequency of the atoms. The varying magnetic field does not cause transitions between the magnetic levels, but the atomic spin adiabatically follows the direction of the total magnetic field, determined at the trap position by the slowly rotating magnetic field. In our case, $\vec{B}_T(t)$ is rotating around an axis perpendicular to the direction of light propagation, so that the spin projection along the light propagation axis and therefore the optical rotation oscillates in time with the characteristic frequency of the rotating magnetic field. Accordingly the signal is detected in this frequency.

1.2 Optical system design

1.2.1 Introduction to optical instrumentation

Optical design is the process of designing an optical system in order to comply with the required specifications that can include performance goals or dimensional constrains and compatibility issues. To a large extent the complexity of the of optical design process depends on balance between the goals and the constrains d introduced by the system specifications. As with any other design process, the goal is to achieve the best possible result with the lowest possible

complexity. Since the process can asymptotically reach to a solution, or even many variations of a solution, other aspects like financial and human resources are critical for the finalization of the optical design process. .

The optical design process is usually performed in several consecutive steps.

- The first step is to clarify the constrains and the required performance specifications of the system.
- Following, a basic optical system using ideal thin lenses and paraxial approximation that complies with the magnification, field of view and NA specifications is designed.
- Based on this primary design the optical elements and the type of materials that will be used is selected.
- The primary design, implemented using the selected optical elements, is used as a starting point in the ray tracing design process. After a sequence of computationally intensive, ray tracing cycles where various parameters of the system, like distances between the lenses, radii of curvature are chanced, the system performance is optimized. This process is not fully automated since it involves the use of several design strategies that are based on the identification of qualitative features of the optical aberrations of the system.

Finally, there are some important quantitative parameters that characterize the performance of the designed system.[22] The most important are:

- Optical Resolution. because it provides information on how small objects the optical system can detect,
- Image illumination,
- The numerical aperture (NA) since it affects the resolution and illumination,
- The field of view.

  Below is a brief description of each of the above quantities.

Resolution

The resolution refers to the smallest object size that can be resolved by an optical system. It is determined by the numerical aperture NA and the wavelength λ of the light used to illuminate the object. The numerical aperture (Figure 1.1) is defined as the product:

$$NA = nsina\ , \tag{8}$$

where n is the refractive index of the medium in object space (for air n ≈1), and α is the half angle of the cone of rays that the optical system collects from the object. The resolution R of an optical system, defined as the smallest distance of two point sources on the object that is distinguishable in the final image, is given by the relationship:

$$R = \frac{0.61\lambda}{NA} \tag{9}$$

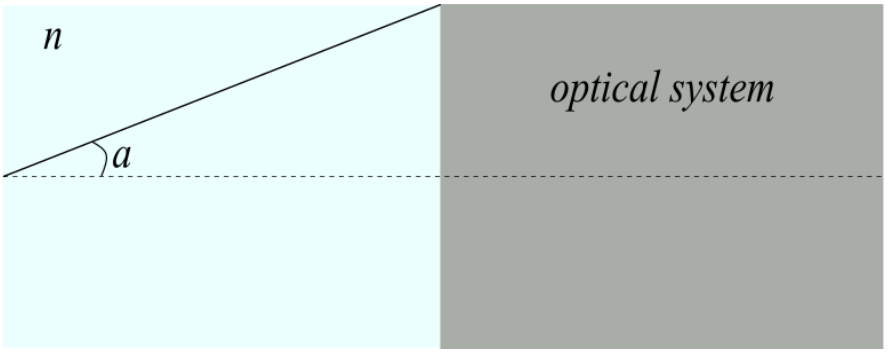

Figure 1.1. Numerical aperture.

Image illumination

Image illumination refers to brightness and the intensity distribution of the image and depends on the physical dimensions of the optical system apertures that control which portion of the light emitted from the object is collected (Figure 1.2) In more detail, image brightness depends on the focal distance of the lens f and the diameter of D entrance pupil.

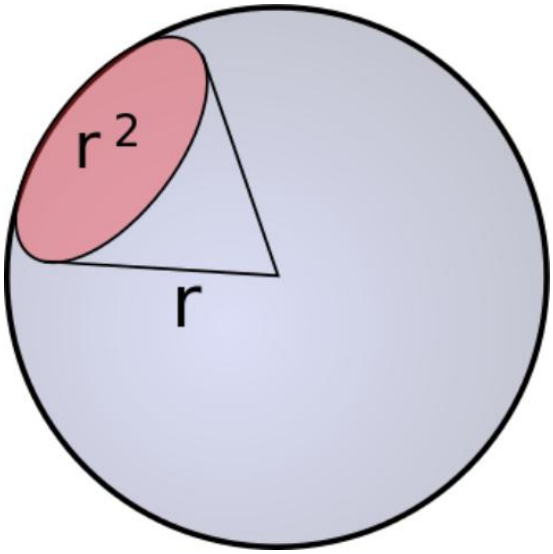

Figure 1.2 Object light emission is the gray shadowed area and the portion of this that the imaging system can collect is the red shadowed area. Taken from Wikipedia.

An important figure of merit that defines image illumination is the f-number (#F=f/D)[23]. The image illumination I is inversely proportional to the square of the #F of the lens:

$$I \sim \frac{1}{(\#F)^2} \tag{10}$$

At the paraxial regime the F-number is inversely analogous to two times the NA. So finally the Illumination is proportional to the squared Numerical aperture of the optical system.

Another phenomenon that is related with the image illumination is the vignetting effect. Vignetting describes the reduction in brightness as we move towards the edge of the image. Vignetting results from the finite size of optical elements in a many-element optical system and is linked to the entrance pupil[24].

Field of view

. The field of view *Field Of View (FOV)* of an optical system is determined as the maximum object's angular size as seen from the entrance pupil[25]. In other words field of View (FOV) directly defines the size of the object field which can be imaged by an optical system. Any limitations in the image height, like for example the sensor size, also affect the FOV. The optical system's FOV can be affected by many parameters like maximum object size, detector size, or by the field over which the optical system performs within the specs. The maximum FOV for an optical system is typically:

$$FOV(mm) = \frac{sensor\ size(mm)}{Magnification} \tag{12}$$

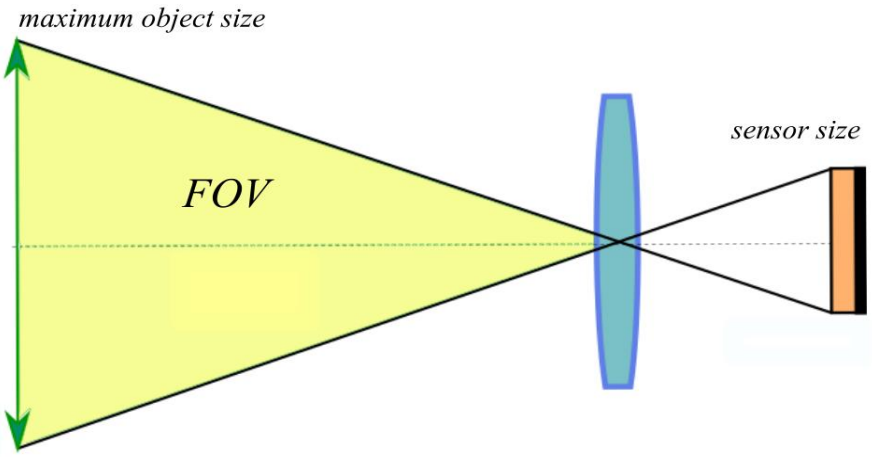

Figure 1.3. Field of view

Another way to characterize the field of view this is the *Angle Of View (AOV).* In more detail, (AOV) refers to the angular extent of the object . The angle of view is determined by the focal length of the optical system and the form/size of the camera's sensor, so the angle of view of an optical system varies when changing sensors. The angle of view is given by the formula:

$$\mathrm{AOV(degrees)} = 2\sin^{-1}\left(\frac{\text{sensor width}}{2\cdot\text{focal lenght}}\right) \quad (13)$$

1.2.2 Optical aberrations

Optical aberrations refer to any deviation, of the performance an optical system, from stigmatic imaging, i.e. from the ideal paraxial conditions. As a result of optical aberrations the wavefront exiting the optical system is deformed from it's ideal paraxial shape. All optical elements introduce aberrations in the non-paraxial regime that depend on the lens / mirror geometry, the geometry of the beam. Optical aberrations also emerge from imperfections in the optical component manufacturing.. Furthemore, different lenses, like for example converging and diverging lenses, suffer from optical aberrations of opposite sign. This is exploited in the optical design process where using a combination of optical elements the designer tries to balance the optical aberration in the whole optical system. Optical aberrations are divided into two categories: Monochromatic or Seidel aberrations and chromatic aberrations [24],[26],[27]. A description of the main optical aberration presented below.

Spherical Aberration

Spherical aberration is caused by the inability of the optical system to focus all the light rays of an axial object, on the same point of the optical axis. Figure 1.4 shows typical the effect of spherical aberration on the image. The lens at the periphery is more powerful than at its center thus the peripheral rays are focused stronger than the paraxial ones. Spherical aberration can be characterized as longitudinal or transverse. The longitudinal aberration refers to the focus elongation on the optical axis while the transverse refers to the transverse focus spread on the the paraxial image plane. Spherical aberration depends on the lens shape. Since all single lenses suffer from spherical aberration we use combinations of lenses (negative and positive) to reduce the spherical aberration. The minimization of spherical aberrations is the first

priority if we want to minimize the remaining monochromatic errors (Comma, Astigmatism, Field curvature, Distortion).

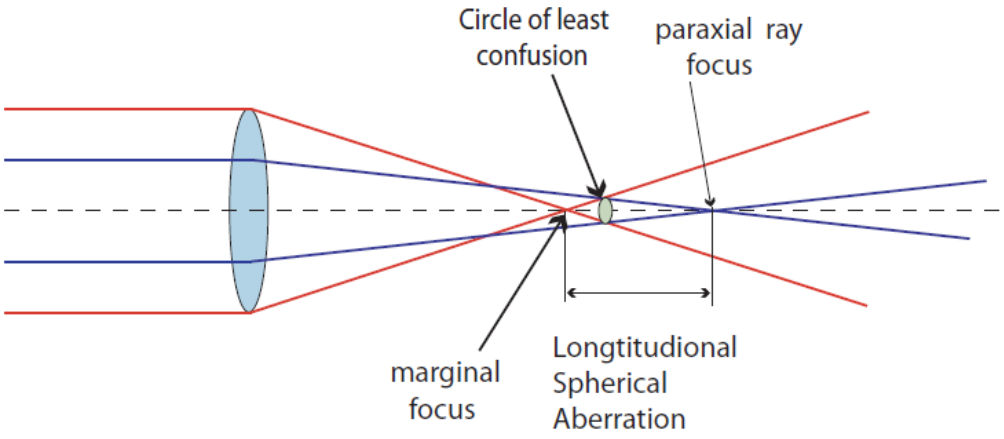

Figure 1.4. Spherical aberration. The periphery of the lens has shorter focal length than the center. Figure taken by [10]

An optical system suffers from positive spherical aberration when the paraxial focal length is longer than the marginal focus. In the opposite case when the marginal focal length is longer the optical system suffers from negative spherical aberration.

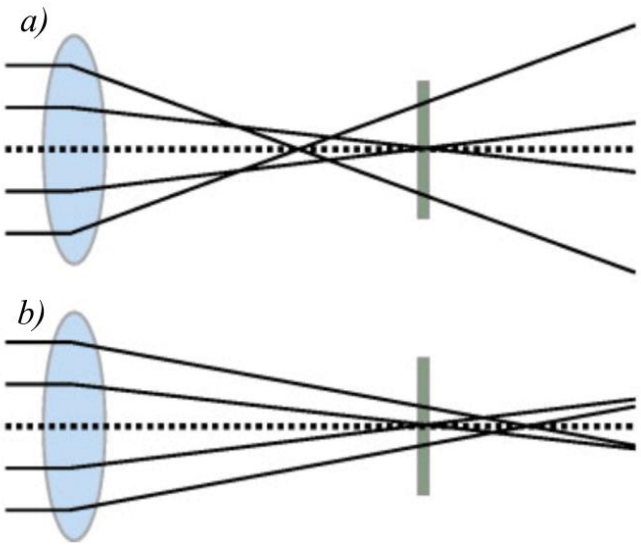

Figure 1.5 a)Possitive b)negative spherical aberration

Coma aberration

Coma aberration originates from the different transverse magnification between the paraxial and peripheral rays and emerges only for non-axial objects. Coma aberration degrades the image quality since instead of a point in the image plane a comet tail is formed as shown in Figure 1.6. This aberration can be corrected with a symmetric combination of lenses or with tilting one lens or the whole optical system. Coma aberration, like spherical aberration, depends strongly on the lens shape. Usually coma aberration is corrected after the spherical aberration has been corrected.

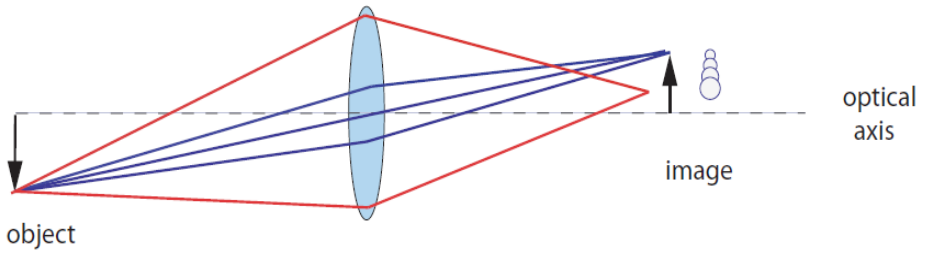

Figure 1.6. Coma aberration. The coma tail is obvious at the image plane. Figure taken by [10]

Astigmatism

Another aberration that appears for non-axial objects is Astigmatism. As shown in Figure 1.7.This aberration originates from the asymmetry between meridional and sagittal ray bundles. This results in a single point in the objects being imaged as two longitudinally separated, normal to each other, line segments. These two line images make up a blurry image, a cloudy circle, also known as the cycle of minimal confusion. Astigmatism can emerge also from misalignments of the optical elements.

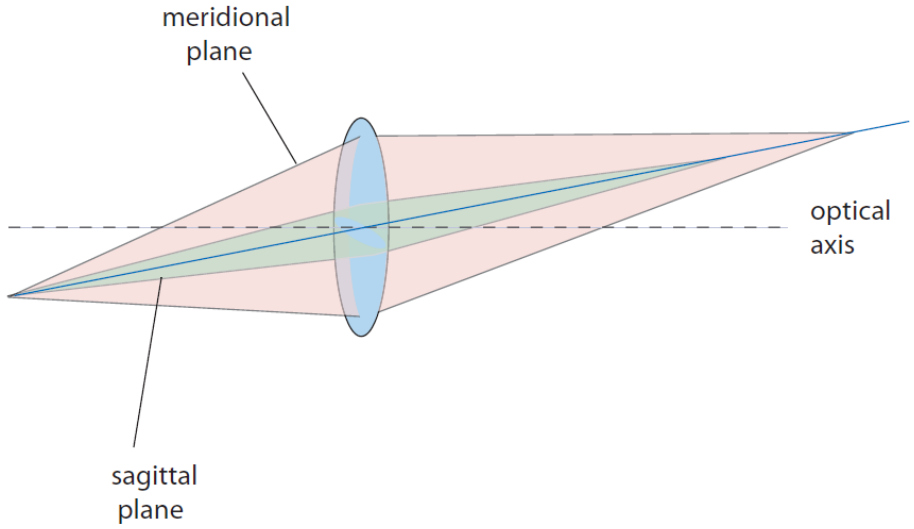

Figure 1.7. Astigmatism aberration. The focal length at the meridional plane is larger than the sagittal. Figure taken by[10]

Field curvature

In an astigmatism free system, the focus in the meridional plane coincides with the one in the sagittal plane However, an extended flat object is focused typically on a curved (non-flat) surface, called the Petzval surface. This effect gives rise to the field curvature aberration (see Figure 1.8). In the case of a camera detector, field curvature can compromise significantly the resolution of the optical system when imaging extended objects, due to the flatness of the detector.

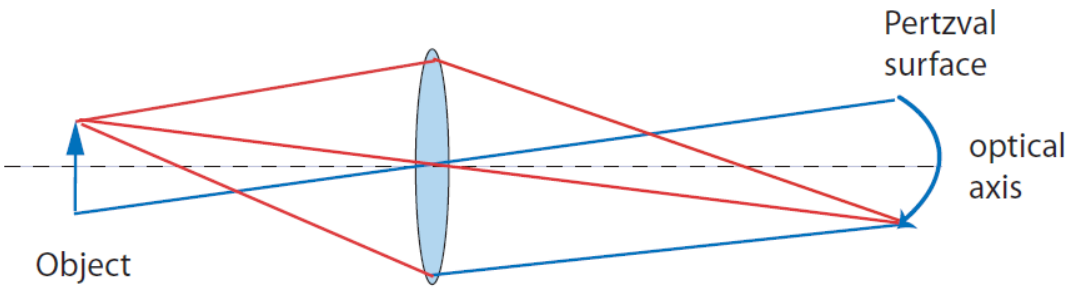

Figure 1.8. Field curvature aberration. Figure taken by [10]

Distortion

Distortion is a form of optical aberration, according to which a rectangular grid object is imaged to a curved grid in the image plane. This is because, in a system suffering from the distortion aberration, the transverse magnification varies with the distance from the optical axis. If the magnification decreases as the distance increases from the optical axis, the grid image has barrel-like shape; if the magnification increases when the distance from the optical axis increases, the shape of the grid image will have a "Pincushion" form (see Figure 1.9). A way to balance this aberration is to use combination of doublet lenses in the optical design process.

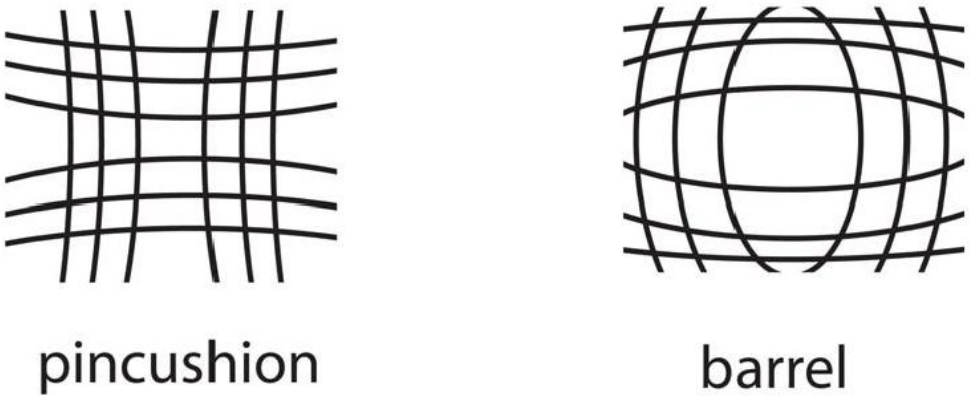

Figure 1.9. Pincushion and Barrel Distortion. Figure taken by [10]

Chromatic aberrations

The next category of the Primary aberrations is the Chromatic. Chromatic aberrations occur due to the dispersion (i.e., the refractive index of the material depending on the wavelength of the light beam passing through the material). Unlike the primary monochromatic aberrations chromatic aberration occurs also in the paraxial regime. As shown in Figure 1.10, there are two ways to

characterize chromatic aberration. The first is the longitudinal chromatic aberration that refers to the dependence of the focal length on wavelength On the other hand, transverse chromatic aberration refers to the dependence of image height, i.e. transverse magnification, on the wavelegth. When the chromatic aberration is detected in an optical system, the only way to reduce it is to combine optical elements manufactured by materials of different dispersion (achromatic doublets for instance). A characteristic figure of merit of the dispersion in a material is the Abbe Number (V):

$$V = (n_D - 1)/(n_F - n_C) \tag{14}$$

, where n_d, n_F, n_C are the refractive indices of the material at the wavelengths of Fraunhofer spectral lines (589.3nm, 486.1nm and 656.3nm respectively.). If Abbe Number is large, the dispersion is small, and as it goes smaller, dispersion increases. So, for instance, in order to design an achromatic optical system that consists of two lenses (i.e. without chromatic aberrations), the following condition should fulfilled:

$$f_A V_A + f_B V_B = 0 \tag{15}$$

,where f_A, f_B are the focal lengths of the lenses and V_A, V_B the Abbe numbers of the respective lenses.

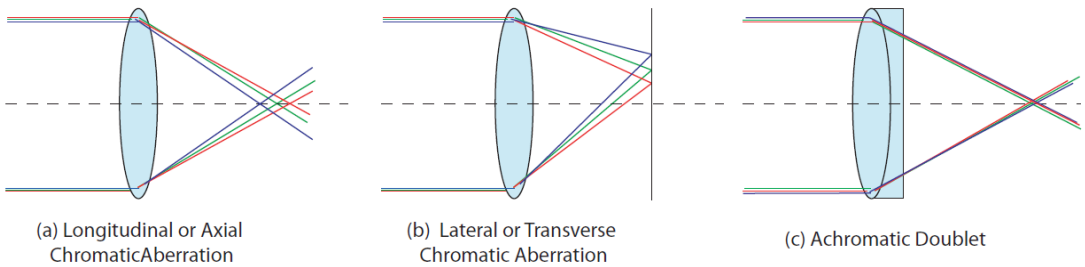

Figure 1.10. Chromatic aberration. Longitudinal (a) and Lateral (b) chromatic aberration. The way that an achromatic doublet focuses the different wavelengths. Figure taken by [10]

1.2.3 Optical design strategies

Elimination of spherical aberration

A flat parallel plate is the simplest refractive optical element. Flat parallel plates are often encountered as optical windows, cover glasses beam splitters etc. in a wide range of applications (biology, atom physics, imaging throw a cell etc.). In the majority of the cases, the optical window is introduced as a constraint of the experimental setup and cannot be avoided. Many optical designs are developed without taking into account the existence of such optical windows. As a result, the presence of a flat plate compromises the achieved image resolution by introducing spherical aberrations. There are advanced optical systems (e.g. microscope objectives), which are designed by taking into account the presence of specific flat windows (e.g. microscope slides of particular thickness). However, these systems are not flexible and their optimal imaging performance is achieved only through a narrow range of windows. Furthermore, generally speaking, one often encounters situations where the available imaging system suffers from spherical aberrations. In these cases, we would like to have an easily implemented way of correcting for spherical aberration. In this section we present a versatile, easily adapted method for correcting positive of spherical aberrations. The method consists of introducing a flat glass plate of specific thickness at the imaging space. The idea behind the method is that the flat window introduces aberrations that counter-act the existing spherical aberration of the rest of the imaging system. Although the flat plate technique only corrects positive spherical aberration, this in fact is not very limiting; in the majority of the cases, the designer can easily modify the optical system (e.g. by adjusting the distance between the optical elements) to have this particular class of spherical aberration.

A simple way to understand why a glass plate, inserted in a converging (or diverging) beam, induces spherical aberration is the scheme below. If it is

assumed that there is a parallel pate with refraction index *n* which width is *d* and is inserted in a converging beam. Two rays of the beam are shown, the paraxial and the marginal ray. The angle in which the paraxial ray enters the plate is about zero (paraxial approximation). From the other side the angle for the marginal ray is larger enough and its value is "γ". After simple geometrical calculations and using Snell's law, one can see that the plate causes a parallel shift in the ray and hence a longitudinal displacement *Δs* (Eq.16) of the point that the marginal ray crosses the optical axis i.e. a focus displacement for the marginal rays:

$$\Delta s(\gamma, n, d) = d\left(1 - \frac{n_m \cos(\gamma)}{\sqrt{n^2 - n_m^2 \sin(\gamma)^2}}\right) \qquad (16)$$

, where d is the width of the glass window, n is the refractive index of the plate and n_m the refractive index of the surrounding medium.

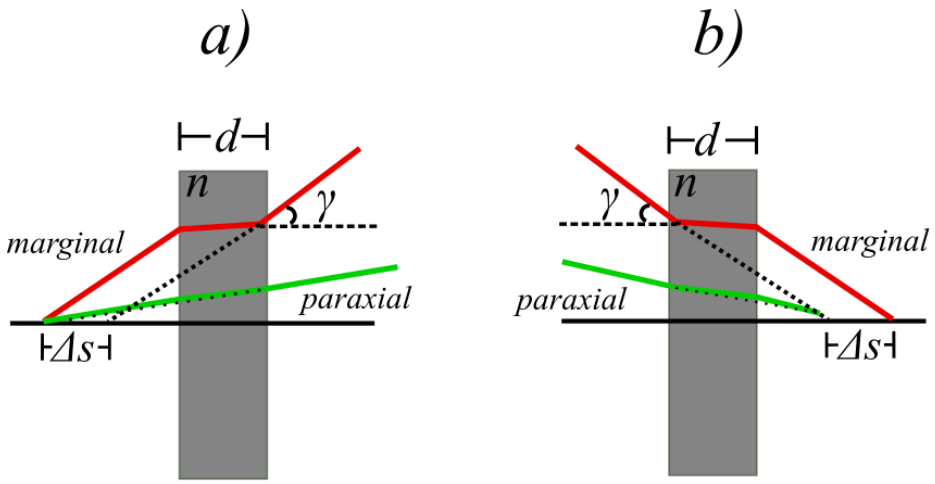

Figure 1.11. A flat plate installed in a a) diverging and b) converging beam. The plate in both cases causes a parallel displacement of the beam. Due to the refraction of the two parallel surfaces the marginal ray reaches the optical axis at a different point than the paraxial ray. The distance between these two points is Δs.

The same can be written as a function of the numerical aperture of the system. Since $NA=n_m \sin(\gamma)$, where n_m is the refractive index of the surrounding medium eq. 16 takes the form:

$$\Delta s(NA, n, d) = d\left(1 - \frac{\sqrt{n_m^2 - NA^2}}{\sqrt{n^2 - NA^2}}\right) \quad (17)$$

According to this formula, the larger the NA, the longer the longitudinal displacement for a specific ray. This effect is essentially spherical aberration's by definition, since this simple optical system bends marginal rays differently than the paraxial ones. As it obvious, for small NA (paraxial approximation) the paraxial rays focus is displaced by:

$$\Delta s(NA \to 0, n, d) = \frac{d(n - n_m)}{n} \quad (18)$$

Consequently, if this is subtracted from the *Δs(NA,n,d)* formula the result is :

$$\Delta s_1(NA, n, d) = d\left(1 - \frac{\sqrt{n_m^2 - NA^2}}{\sqrt{n^2 - NA^2}}\right) - \frac{d(n - n_m)}{n} \quad (19)$$

So this is the longitudinal distance between the paraxial and the marginal ray focus that the inserted plate causes. At the graph below can be seen how the normalized displacement $\Delta s_1/d$, that the plate causes, evolves as the numerical aperture of the system increases for a plate with refractive index *n=1.5* and variable width *d.*

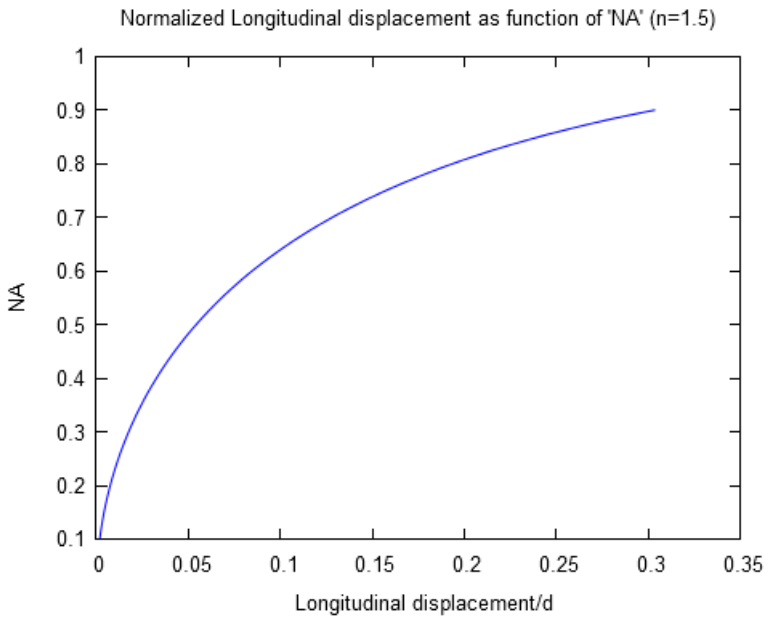

Figure 1.12 Normalized longitudinal displacement for a plate with refractive index n=1.5 as a function of the Numerical aperture of the optical system. The displacement increases as the numerical aperture reaches larger values.

We can correlate this analytic result to the formal definition of spherical aberration of an optical system. The wave aberration is given by the difference in the optical path lengths between the chief ray and another ray that reaches the exit pupil at height r and angle θ(polar coordinates) from the optical axis [28]. The h referred to an off axis point located along the optical axis at a height h from the optical axis. The primary wave aberrations can be described as[28]:

$$W(r,\theta;h) = a_s(r^4 - 4hr^3\cos\theta + 4h^2r^2cos^2\theta + 2h^2r^2 - 4h^3rcos\theta) \quad (20)$$

Especially for a flat parallel plate the coefficient α_s is given from [26]:

$$a_s = \frac{(n^2-n_m^2)d}{8n^3S^4} \quad (21)$$

, where S is the distance of the object from the first surface. The aberration coefficient α_s is related to the Seidel spherical aberration coefficient S_1 by:

$$S_1 = 8a^4a_s = \frac{a^4(n^2-1)d}{n^3S^4} \quad (22)$$

, where α is the radius of the exit pupil. The equation above can be rewritten as a function of the numerical aperture of the system:

$$S_1 = tan^4(\arcsin(NA))\frac{(n^2-n_m^2)d}{n^3} \quad (23)$$

Thus the Seidel spherical aberration coefficient of a known a glass plate can be estimated or vice versa the one can calculate the width of the glass plate that induces this aberration.

$$d = \frac{(NA^2-1)^2 n^3 S_1}{NA^4(n^2-n_m^2)} \quad (24)$$

Or

$$S_1 = \frac{NA^4(n^2-n_m^2)}{(NA^2-1)^2 n^3}\, d \quad (25)$$

,where *NA* is the image space numerical aperture of the setup and *n* is the refractive index of the glass plate and n_m that refractive index of the surrounding medium .

Ray tracing simulations

If an optical system suffers from positive spherical aberration, a glass plate can be inserted at the back of the system in order to correct them. The flat plate is possible to correct only positive spherical aberrated systems since its effect is that the marginal rays reach the optical axis farther away than before. This means that a glass plate could be a useful tool at optical design process. For a given optical system, with an optical design software ,information as numerical aperture(image and object space), Seidel coefficient for primary spherical aberration and the longitudinal distance between the focus of paraxial and marginal rays at image space can be easily obtained. Since the longitudinal distance between the rays in optical axis and the Seidel coefficient for primary spherical aberration that the plate induces (Eq. (19) and (25)) are known, we can induce opposite spherical aberrations in a given setup.

Two examples, which consist of two commercially available high precision aspherical lenses, are presented below in order to be clear that even in simple optical systems the spherical aberration can be corrected with a flat glass

plate of a specific width. The main difference between the two examples is the NA of the systems since the first is composed by 1" optics (small NA) while the second by 2" lenses (larger NA). Their common feature is that both of them exhibit positive spherical aberration. Optical design software, Zemax, was used in order to simulate these two simple examples. Information about the diagnostics of this software can be found at Appendix C.

• *First example: 1" aspherical lenses, 49116, Edmund optics*

The first example is a simple optical system that images a point source on the optical axis, through a glass window. It consists of two identical aspheric lenses (commercially available, Edmund optics, part num. *49116)* (Figure 1.13).

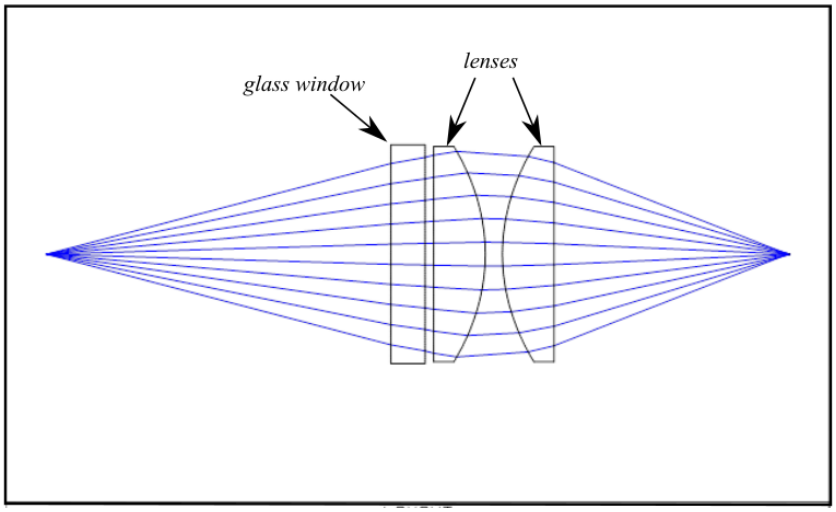

Figure 1.13 Layout of optical setup with two 49116 lenses from Zemax software .The simple setup images a point source throw a glass window. The distance between the point source and the glass window is 40mm .

After the spot optimization, in order to make the spot size as small as possible the spot size is about 36μm in radius (Figure 1.14). Furthermore the Seidel coefficient for spherical aberration, S_1, is 0.131806 for this optical system. This is actually the optimal performance for this 2 lens setup.

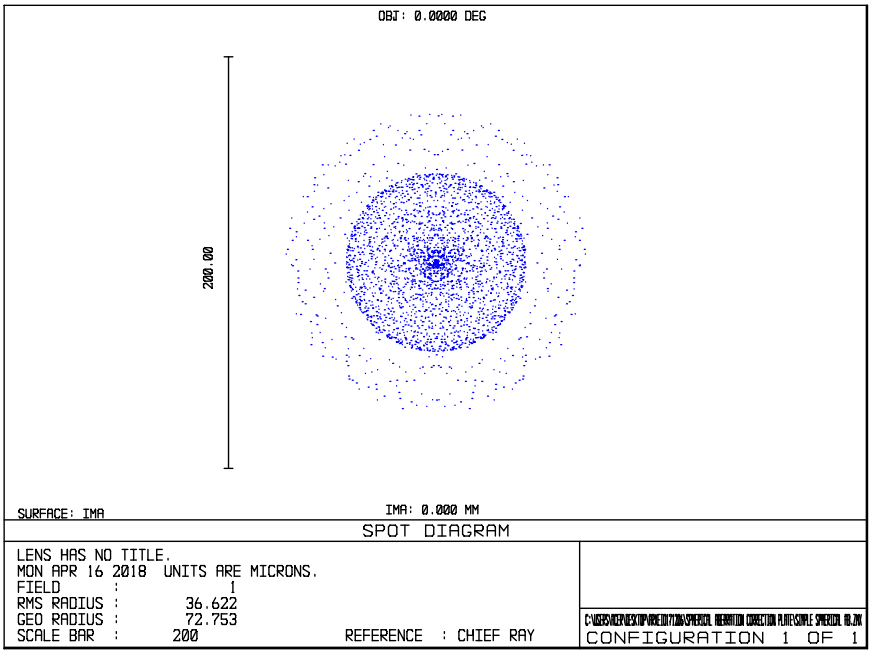

Figure 1.14 Spot diagram of optical setup of two 49116 lenses from Zemax software. The rms spot radius is 36.622μm

Our novel approach is to eliminate this residual spherical aberration by inserting a flat plate at the exit of the optical system. According to the equation (24), it is possible to estimate the required width of a glass plate that balances the first order spherical aberrations of the system. In this case the image space numerical aperture, calculated by Zemax, is 0.3655068 thus the estimated optimal plate width is: 14,968mm (for n=1.5)(Figure 1.15).

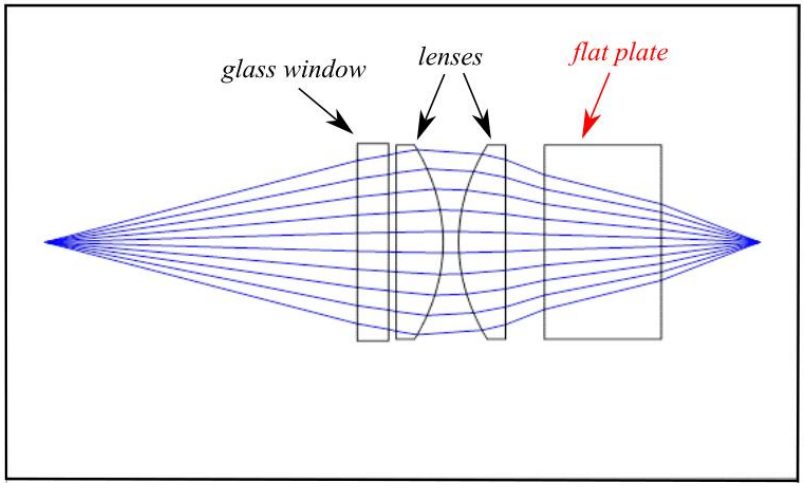

Figure 1.15 Layout of optical setup with two 49116 lenses and a flat plate at the back of the setup extracted by Zemax software. The calculated width flat plate is inserted at the image space of the system. It must be noted that every position in image space is equivalent.

After the inserted flat plate the S_1 spherical aberration coefficient is reduced by about 3 orders of magnitude to 0.000287. There is a clear improvement at the spot size radius that reduces to11.1μm as well (Figure 1.16).

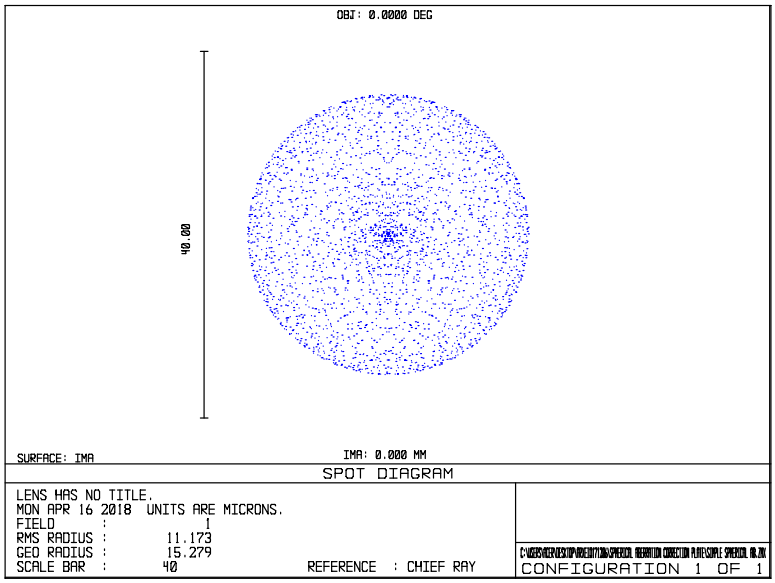

Figure 1.16.Spot diagram of optical setup with two 49116 lenses and a flat plate from Zemax software. The rms spot radius is 11.171μm after the addition of the glass plate.

The optical system performance can be further improved since the analytically estimated plate width eliminates only the primary spherical aberration while, higher order aberrations still remain. Although it is impossible to retrieve an analytical solution for the elimination of the higher order aberration terms we can use the know longitudinal distance between the points that the paraxial and the marginal rays cross the optical axis. Using now the equation (19) we can find the plate's width that induces the opposite longitudinal displacement between the rays. Plate's width is d=20.1347mm in this case. Although the foci of the paraxial and the marginal ray are closer now this doesn't ensure that the spot size now is as small as possible. In order to

minimize the spot size one should search the circle of least confusion at image plane. By slightly varying the plate's width in a numerical raytracing it is possible to optimize it's value in order to eliminates the radius of the circle of least confusion. In this case the system is close to diffraction limited (Figure 1.17) and the spot size at image plane now is about 18 times smaller than the initial setup.

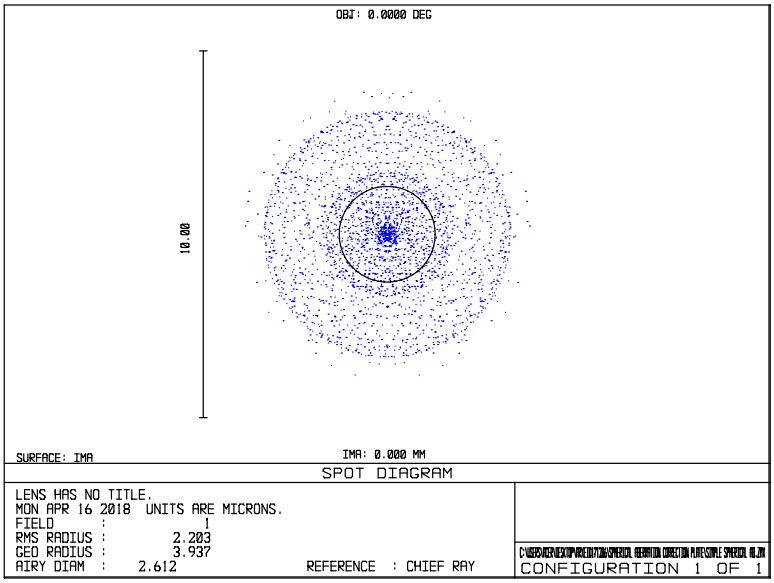

Figure 1.17 Spot diagram of optical setup with two 49116 lenses and the second flat plate from Zemax software .The rms spot radius now is almost diffraction limited ,2.203 μm .The black circle is the diffraction limit of this optical setup.

•*Second example: 2" aspherical lenses, 67254, Edmund optics*

The second example is similar as the previous but the main difference is that now the diameter of the lenses is 2 inch. It consists of two identical, commercially available high precision aspheric lenses. These lenses are from Edmund's optics and the product's model is *67254*(Figure 1.18).

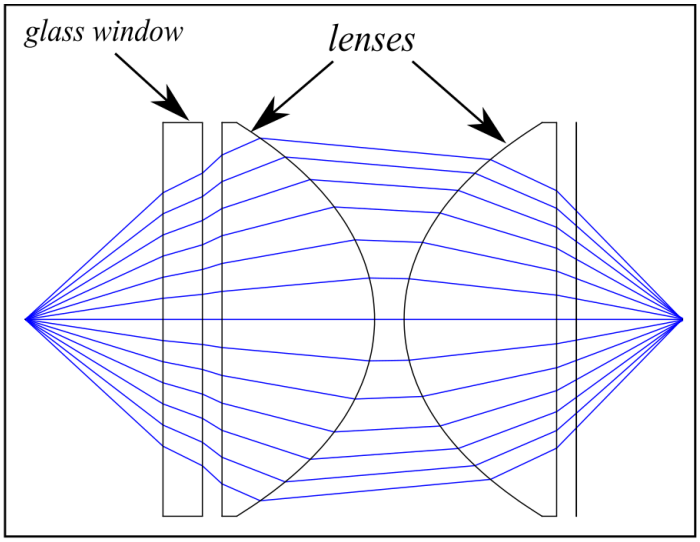

Figure 1.18. Optical layout of optical setup with two 67254 lenses. The optical system images a point source throw a glass window. The distance between the source and the glass window is 14mm

The optimization process is the same as before. The rms radius spot size at image plane is about 60μm.(Figure 1.19) and the Seidel coefficient S_1 is 1.600464.Finally the Numerical aperture at image space is 0.797.

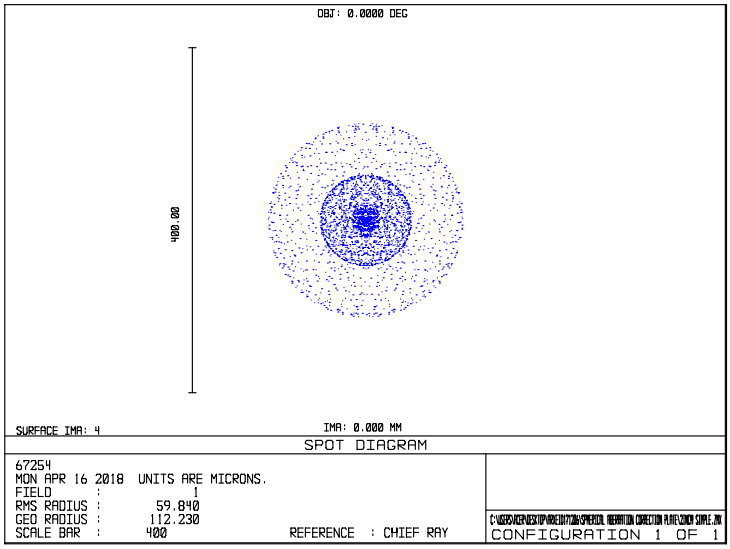

Figure 1.19 Spot diagram of optical setup of two 67254 lenses by Zemax software. The rms spot radius is 59.84μm

As the previous case, we can estimate the plate width that eliminates primary spherical aberration, which in this case is d=1.423mm. After the

addition of a flat plate with this width the Seidel coefficient S_1 is equal to -0.000872 and the rms spot radius is about 38μm (Figure 1.20& Figure 1.21).

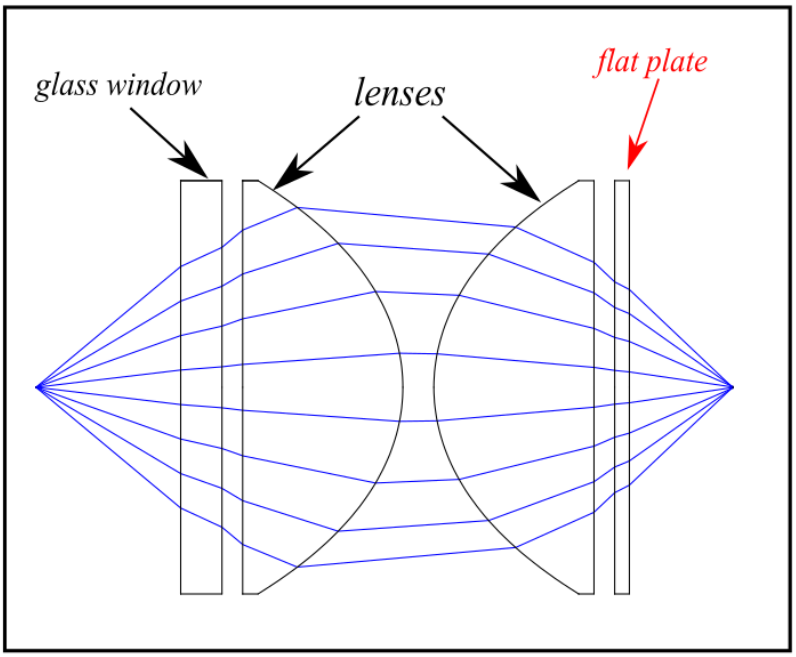

Figure 1.20. Layout of optical setup with two 67254 lenses and a flat plate from Zemax software. The calculated width flat plate is inserted at the image space of the system. It must be noted that, as the previous example, every position in image space is equivalent.

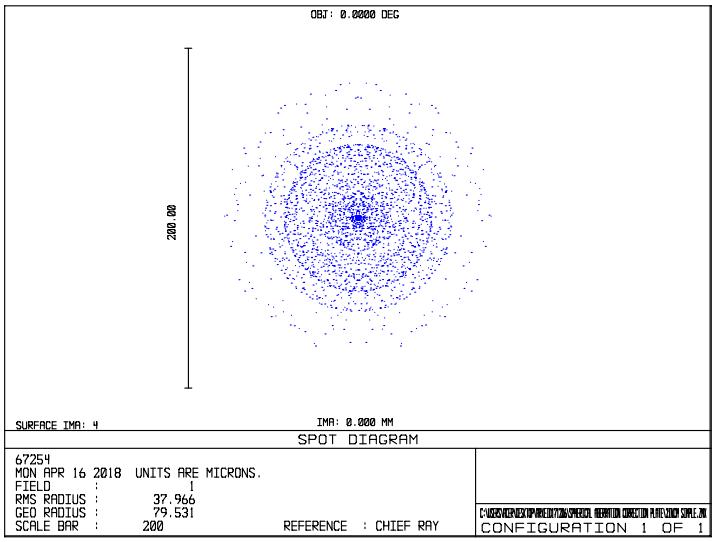

Figure 1.21. Spot diagram of optical setup with two 67254 lenses after the addition of the flat plate from Zemax software. The rms spot radius in this case is 37.966μm.

Furthermore, by using the optical system parameters, retrieved from the optical design software, in equation (19) we can estimate to plate width that minimizes the distance between the focus of the paraxial and the marginal rays. The result is d=2.809mm and this has as a result that the spot size radius now is about, five time smaller than the initial, 12.651μm. To conclude, all the previous results for both systems are summarized in Table 1 below.

Optical Setup	*Object space NA*	*Initial Seidel coefficient S_1*	*Initial radius spot size(μm)*	*After 1st plate radius spot size(μm)(Eq(1)).*	*After 2nd plate radius spot size(μm)(Eq.(2))*
2x 49116	0.25	0.131806	36.622	11.173	2.203
2x 67254	0.73	1.600464	59.840	37.966	12.651

Table 1. Spot size radius performance comparison between the initial systems and the same systems after the addition: i) of the flat plate that Eq.(1) determines ii)of the flat plate that Eq.(2) determines, correspondly.

As we have demonstrated in the previous examples the insertion of a flat glass plate at the exit of an optical system exhibiting spherical aberration can improve considerably the optical resolution. Although the improvement can be dramatic, there are limitations on this technique. The first and most important is that the optical system should exhibit positive spherical aberration. The glass plate cancel this out by adding negative spherical aberration .Another important parameter is that the numerical aperture at the image space should be large in order observe an important enhancement. This technique doesn't substitute the optical design process but can dramatically improve the performance of an optical system.

1.2.4 Gaussian beams

The most basic form of a laser beam is that in which the intensity distribution into a plane perpendicular to its propagation is Gauss form[29]. The distribution of the amplitude of the electrical field of a perfect Gaussian beam is given by:

$$E(x,y;z) = E_0(\mathrm{z})\, exp\, (-\frac{x^2+y^2}{w^2(z)}) \tag{26}$$

where w(z) is the waist of the beam[23]. The simplest-ideal beam shape that can be resulting from a laser resonator is the one that presents radial symmetry. A drawing that presents the main characteristics of a Gaussian beam [23] can be shown below (Figure 1.22)

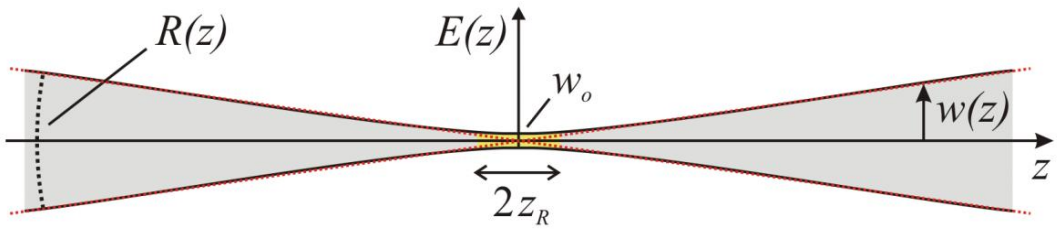

Figure 1.22 The main characteristics of a Gaussian beam. Taken by [23]

Two parameters fully define a Gaussian beam, it's wavelength λ and it's waist (minimum radius of the beam) w_0.[30]. Based on these parameters, we can estimate all other beam characteristics s: the beam radius w(z) and the radius of curvature of the beam wave R (z) along the propagation axis in a position z. The beam radius w(z) is defined as the distance from the z-axis to the points where the intensity of the beam drops to the $1/e^2$ (13.5%) of its value.

The above parameters are related to each other according to the following equations:

$$w(z) = w_0\sqrt{1 + (\frac{z}{z_R})^2} \tag{27}$$

, where z_R is equal to $\pi w^2_0/\lambda$ and λ is the wavelength of the beam. The distance z_R is called Rayleigh range and is equal to 1/2 of the solenoid focus length. The second one relates the radius of curvature R(z) with the Rayleigh range and the distance z :

$$R(z) = z + (\frac{z}{z_R})^2 \quad (28)$$

Now let's assume that there is a converging lens that is placed at the waist of a diameter *D* Gaussian beam as it shown at the Figure 1.23.

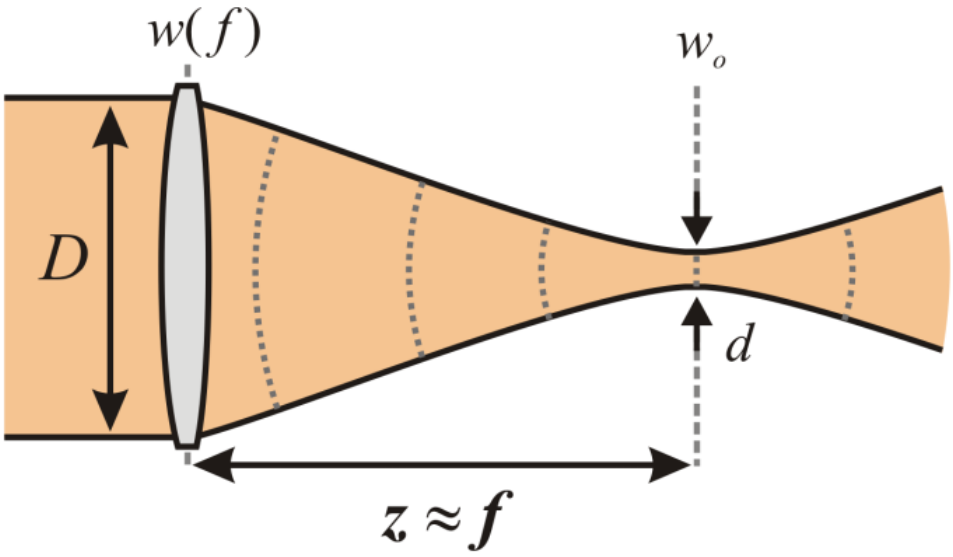

Figure 1.23. A positive power lens is putted at the waist of a Gaussian beam and focuses it. Figure taken by [23]

Since of the beam diameter *D*=2w(*f*) and using Eq. 27 we get [23].

$$D = 2w(f) = 2w_0\sqrt{1 + (\frac{f}{z'_R})^2} \cong \frac{2w_0}{z'_R}f = \frac{2\lambda}{\pi w_0}f \rightarrow \boldsymbol{d = 2w_0 \cong \frac{4\lambda}{\pi D}f} \quad (29)$$

From this equation is obvious that for a Gaussian beam with standard wavelength there is a lowest waist that can be achieved and depends on the ratio *f/D*. In other words if the diameter of the beam *D* is constant, a more powerful converging lens will focus the beam in a smaller area than a less powerful lens. Respectively if a standard converging lens be used in order to focus a Gaussian

beam the focus area depends inversely on the diameter of the beam. The smaller the beam diameter the larger the focus width and vice versa.

1.2.5 Opto-mechanical design

After the end of the optical design process follows the opto-mechanical design process. The opto-mechanical design is intimately linked to the application requirements for which the optical design is intended. In each individual case the requirements and the restrictions are different. For example, the requirements of an opto-mechanical design for space missions are specific [31],[32] and different from the design of a mount for binoculars [33]. In most cases, requirements and constraints are conflicting. A successful opto-mechanical design is what manages to achieve the best possible result, bearing in mind the specific limitations. In any case, the opto-mechanical design must ensure or enable the necessary alignment of the optical elements [34]. In applications such as those of cold atoms experiments, the required optical resolution is usually high. In order to achieve this, the optics should be mounted with great precision and without tilts. The mechanical support of the optical system must be a solid and robust construction in order to prevent any displacement of the optics from the designed positions [35]. Such displacements effect the optical resolution. In this sense, vibrations are also detrimental to the optical system performance.

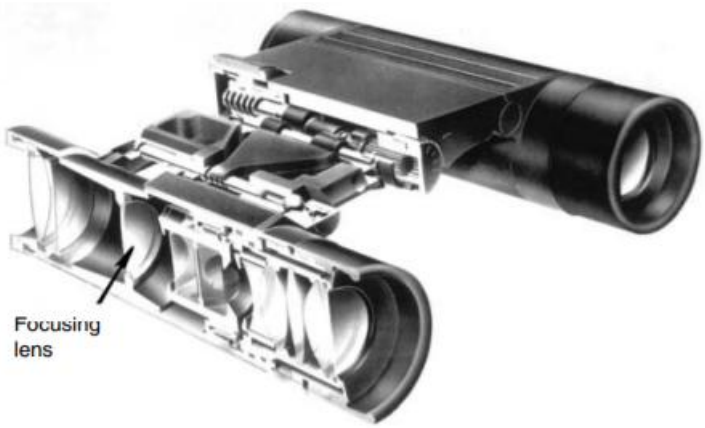

Figure 1.24. Opto-mechanical design for binoculars. A robust mount keeps the lens at their specific positions.

The construction should be handle and light while in this case thermal expansion does not play an important role so the used material is metal. Figure taken from [35]

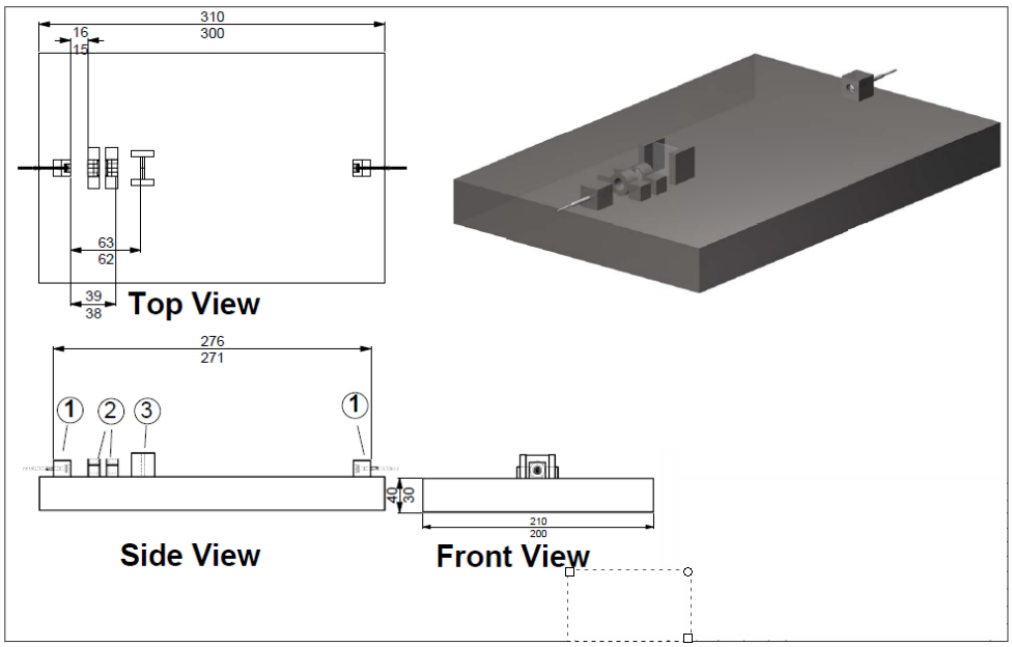

Figure 1.25. Optomechanical design for space missions. This breadboard will be assembled in the earth and after that will be sent to the space. Thermal expansions are crucial in this case so the used material is Zerodur glass. Figure taken by[32]

In our case, there are no significant changes in the ambient temperature, so the thermal expansion coefficient of the materials used in the mechanical parts is of minor importance. In cold atom experiments, optical systems are often placed close to strong magnetic fields. This means that the mounts of the lenses should not be metallic in order to avoid eddy currents. Eddy currents increase the temperature of electrically conductive materials, resulting in heat deformation. Under these conditions, the relative positions of the optics are possible to change. As a result of this, non-conductive materials should be used for lens mounting in order to avoid eddy currents.

For the opto-mechanical design we used CAD (Computer-aided design) software that enables the high precision designing of mechanical parts. This of software allows the design of individual parts of the opto-mechanical design. Furthermore enables the user to place all parts together and check their compatibility when placed together in order to identify errors made during

design process. CAD software also makes it possible to export mechanical drawings, something particularly useful as it saves the user valuable time.

All mechanical designs presented in this thesis were made using *Inventor Autodesk* CAD software (Student version). This is a state of the art 3D –CAD software that gives a lot of possibilities as new shape generation, parametric modeling, assembly modeling, and mechanical drawing creation. .

2 Implementation

At this chapter briefly described the motivation, the optical design process for, the achieved performance and the opto-mechanical design process for both optical systems.

2.1 Upgrading the imaging setup for the main experiment of BEC lab

2.1.1 Description and aim of this project

The main goal of this project was the theoretical design and the implementation of a high resolution and high photon collection efficiency optical system that will be used in cold atoms imaging experiments. In such experiments a great amount of quantitative information is extracted from images of the cold atomic cloud. Some of these information are the size and the shape of the atom cloud, its temperature, the number of atoms that apart this cloud and finally its expansion in the trap. Under these circumstances is obvious that the optical resolution is crucial.

The optical system described below is a custom designed optical system that will be used to Bose-Einstein condensation and cold atomic cloud imaging in BEC laboratory of the I.E.S.L on Crete. The optical system was designed in order to serve some specific requirements of this laboratory and it will replace the presently used optical system. This optical set up is designed to be used in cold atom experiments capable of switching seamlessly from absorption to fluorescent imaging.

2.1.2 Optical setup Specifications.

The opto-mechanical design should comply to certain restrictions, which lead to the necessity for developing a custom optical and mechanical design.. The excepted characteristics of the system came up after the detailed study of the restrictions.. Our goal was to achieve the bestpossible performance under the specific circumstances. All the important limitations and optical system's specifications are briefly presented at the table below. Furthermore In the following pages, we present in detail all the limitations that we had to face and how they affected the final characteristics of the new optical system.

Wavelength(λ)	780nm
Physical total length	(200-250)mm
Minimum working distance	37mm
Numerical aperture	0.30
CCDs' pixels sizes(i-Kon& i-Xon)	(13x13)μm & (16x16)μm
CCDs' sensors sizes(i-Kon& i-Xon)	(13.3x13.3)mm & (8.2x 8.2)mm
First optics diameter(maximum)	25.4mm
Design approach	Doubly telecentric

Table 2. Overview of optical setup specifications.

Device

The main dimensional restrictions are introduced by the experimental setup as a consequence of the limited space provided between the other components as coils, optical elements, cables etc. The experimental setup, in which the optical system under design is going to integrate, is a custom assembly that consists of homemade and commercially available parts. (Figure 2.1& Figure 2.2)

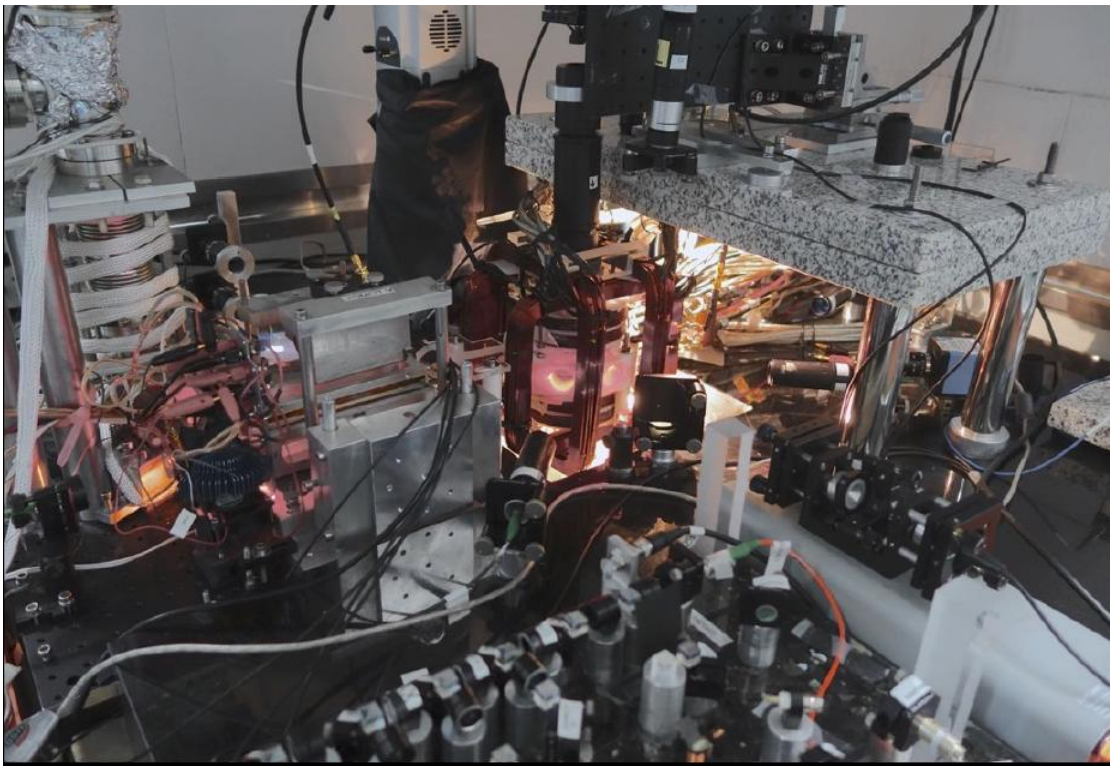

Figure 2.1 A photograph of the main part of experimental setup in BEC laboratory at I.E.L.S. Some optics, fibers, coils, ccd cameras and many other components that are necessary for the experiment, are shown. Photo by W.

von Klitzing.

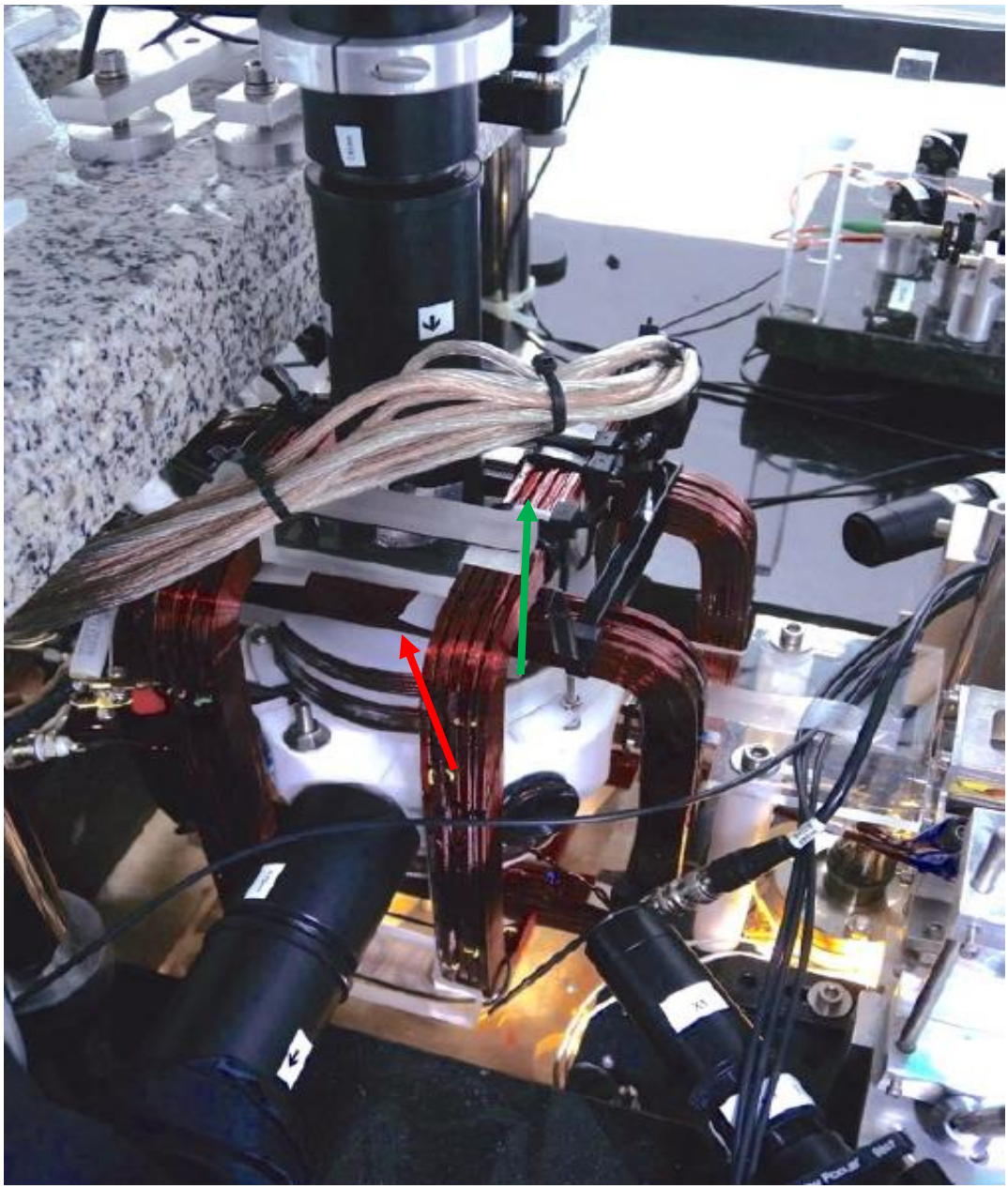

Figure 2.2. A photograph of the experimental setup, zoomed at the position where the new optical system wi fit ,replacing the existing optical system(indicated by a red arrow). The white structure (macor) contains the vacuum cell in which the BEC is created.(indicated by a green arrow).Edited photo by W. von Klitzing.

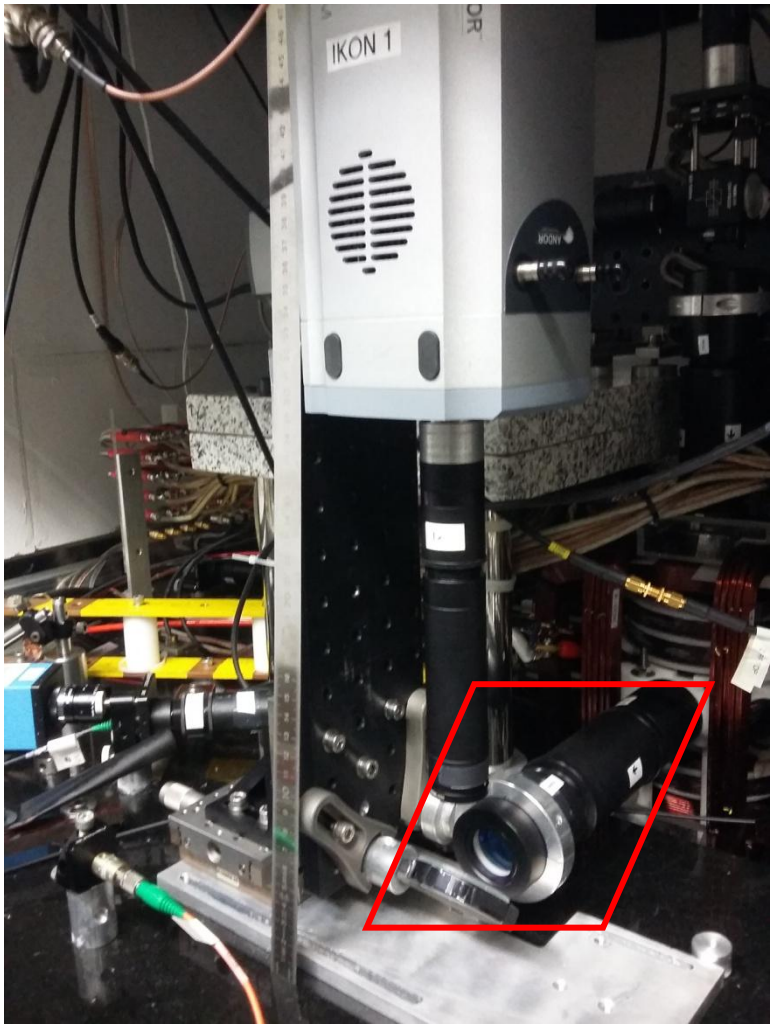

Figure 2.3 At this photo of the experimental setup the space that was available for optics (red polygon) is roughly shown

The total physical length of the optical setup under design was determined by the available space. Thus total length should not exceed 250mm. All the dimensions of interest were measured. Most of them were measured with a mechanical caliper but there were dimensions such as the clear space in macor's hole or the distance between the macor and the vacuum cell that were not accessible. In these cases the dimensions were retrieved using the mechanical drawings of the installation.

The next constraint was that the optical system should image the atomic cloud through the glass window of the vacuum cell. This limits the working distance to be larger than 37mm. Furthermore this window, in combination to the geometry of the vacuum cell, sets the upper limit of system NA to 0.31.

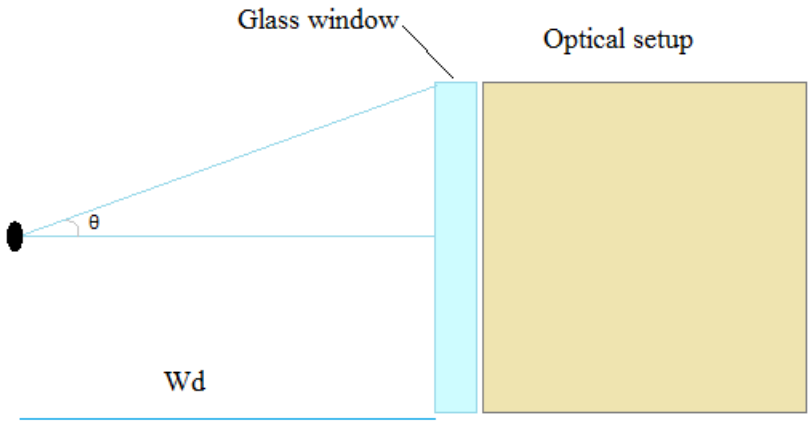

Figure 2.4 Graphical representation of basic experimental constrains. The position of the atomic cloud in vacuum cell affects the Numerical aperture of the optical system.

Using the vacuum cell geometry (W_d=37mm, glass window diameter=25.4mm) with simple mathematical calculations:

- $Numerical\ aperture_{max} = sin(\theta) = \frac{25{,}4mm/2}{\sqrt{(37mm)^2 + (25.4mm/2)^2}} \approx 0.31$

A photograph of the vacuum cell is presented at the figure below. At this figure, the shape and the form of the vacuum cell are shown without the macor structure surrounds it.

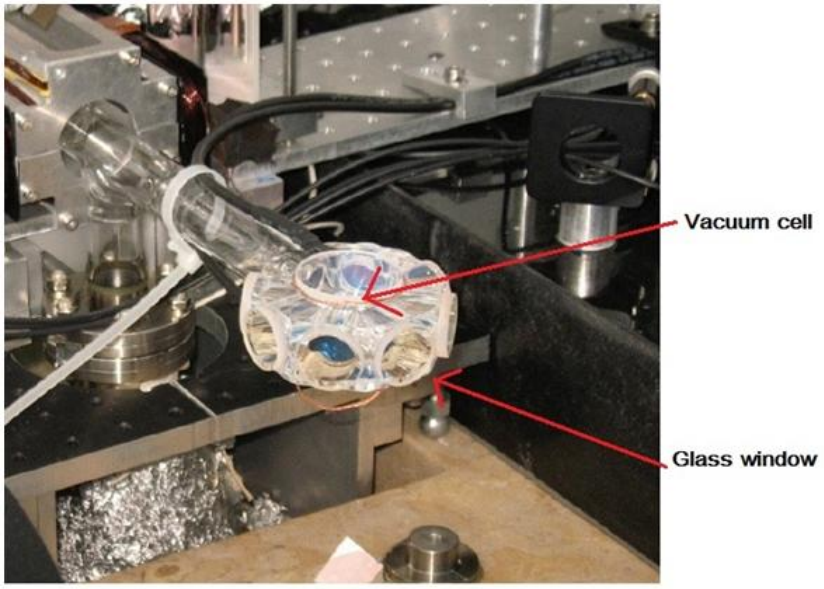

Figure 2.5 A photo of the vacuum cell in which the BEC is created. Vacuum cell is an octagonal structure made of coated silica glass. Each side of the structure is a circular window made of silica which diameter is 25.4mm. Typically the pressure in the cell can be 10-12 Torr.

The macor structure (the white structure depicted in the Figure 2.2) is an octagonal structure that surrounds the vacuum cell .At each side of the macor there are threaded holes (Figure 2.6).This was a very restrictive configuration because any optics should fit in one of these threaded holes. This limits the maximum diameter of the optics to 25.4mm (1 inch).

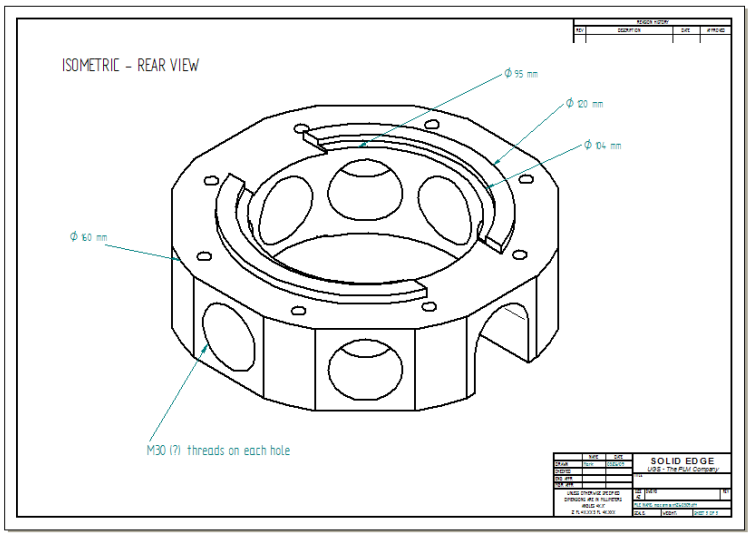

Figure 2.6. Mechanical drawing of the white cup-(macor) . The optical system should be inserted in one of these threaded holes in order to be achieved as larger Numerical Aperture as possible

Cameras

The optical and the mechanical design was designed to be compatible with two different cameras. The most important parameters for the optical design in both cases were the pixel size and the sensor size. As it referred below the dimensions played a key role in mechanical design.

- The first camera that comprises the detection part of the experimental setup is an *iKon-M 934BR DD* by *Andor.* The specifications of this camera are given in the table below:

Specifications	***iKon-M 934BR DD***
Active Pixels	1024x1024
Pixel Size(W x H; μm)	13x13
Sensor size (mm)	13.3x13.3
Quantum efficiency	>90% at 800nm
Frame Rate(frames per sec)	Up to 4.4
Read noise	As low as 2.9 e^-
Pixel readout Rates	5.3.1.0.05 MHz

Table 3 . iKon-M 934BR-DD key specifications.

Figure 2.7. iKon-M 934BR-DD camera

- The second camera is an *iXon Ultra 897* by *Andor.* The specification of this camera are given in the table below:

Specifications	***iXon Ultra 897***
Active Pixels	512x512
Pixel Size(W x H; μm)	16x16
Sensor size (mm)	8.2x8.2
Quantum efficiency	>90% at 800nm
Frame Rate(frames per sec)	56-11074 fps
Read noise	< 1 e^- with EM gain
Max readout Rates	17 MHz

Table 4. i-Xon Ultra 897 key specifications.

Figure 2.8. i-Xon Ultra 897 camera.

Optics

The most important point in optical design process is the usage of suitable lenses and other optical elements. By using custom designed optical components we increase the degrees of freedom in the optical design process. However, custom lenses have the disadvantage of increased financial cost. Another choice is to use commercially available lenses. In this case the cost is kept relatively low, but is difficult to find suitable lenses and appropriately combine them. Considering the advantages and the disadvantages of both approaches we ended up to use commercially available lenses.

Furthermore, in order to achieve as larger as possible numerical aperture the optical system should be inserted in one of macor's structure threaded hole (M30). Since the cell window is 25.4mm in diameter, we chose the first lens to be also 25.4mm. Likewise, the minimum working distance of 37mm is large enough for a medium NA system and in the bibliography is referred[36] to as "super long working distance". So the choice of the first lens of the system should be a lens that combined large numerical aperture and short enough effective focal length. Finally the paraxial transverse magnification of the setup should be about 5 in order to serve the needs of the experiments.

So the two most important system's characteristics ought to be the high resolution and the high photon collection ability, from cold atomic cloud emission. Expect from the important constraints that were referred above, including the length and diameter of the system, the paraxial magnification, , the large working distance that ought to be combined with large numerical aperture (0.30) there are another two constraint that make the used lenses choice more complicated. The first is the (double) telecentric approach for the design. An optical system is double telecentric when the chief rays are parallel to the optical axis both in object and image plane. The telecentricity is fulfilled when the Fourier plane of the first lenset constitutes the object plane for the second lens. Telecentricity makes the system handier since it provides focus stability and ensures the almost constant magnification over a wide range of working distances.

The second is the total number of lenses that comprise the system should as low as possible in order to avoid transmission losses. The signal in cold atoms imaging experiments is weak and is crucial to minimize transmission losses. This can be achieved by using antireflective lenses.

2.1.3 Optical design process

In order to have a thorough overview of the system's characteristics and ray-tracing simulations optical design software was used (Zemax). This software is an invaluable tool for the optical design which offers the capability for simulation, optical aberration calculation, diagnostic graphs, a large catalog with commercially available lenses and many other options. The most important, though, is the optimization process of the system. The performance and the characteristics of the optical systems presented through Zemax software's diagnostics graphs. More information about Zemax diagnostics graphs can be shown at Appendix C.

After performing an initial theoretical analysis, based on paraxial optics, and the application various optical design techniques in a series of raytracing simulations, where combinations of commercially available lenses on different configurations, were optimized in Zemax software, we reached to final system that fulfills all the required specifications. Below the optical design process from the first steps until the final setup is presented.

Existing optical system

Although the constraints the goal of this project is the design of an upgraded optical system that will displace the existing one at Cretan matter waves laboratory. The new optical system should exhibit better performance than the existing one at some specific domains, since that is the reference for us. Simulations in Zemax software gave us information about the characteristics and the performance. An optical layout of the optical system that the matter wave's laboratory uses now can be shown at the figure below.

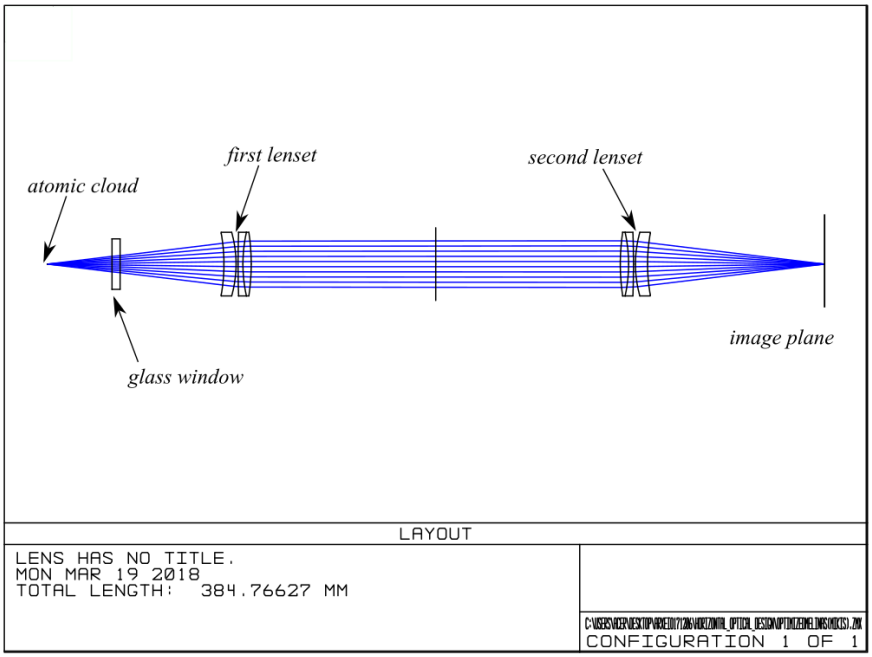

Figure 2.9. An optical layout of the existing imaging system.

The existing optical system consists of two same lensets. Each lenset consists of two lenses, a positive meniscus and an achromatic lens. The effective focal length of each lenset is 91.5mm so the numerical aperture of this system is about 0.11. The spot size diagram at image space can be shown at the figure below. This spot diagram referred to the central field, i.e. rays that start from a point on the optical axis.

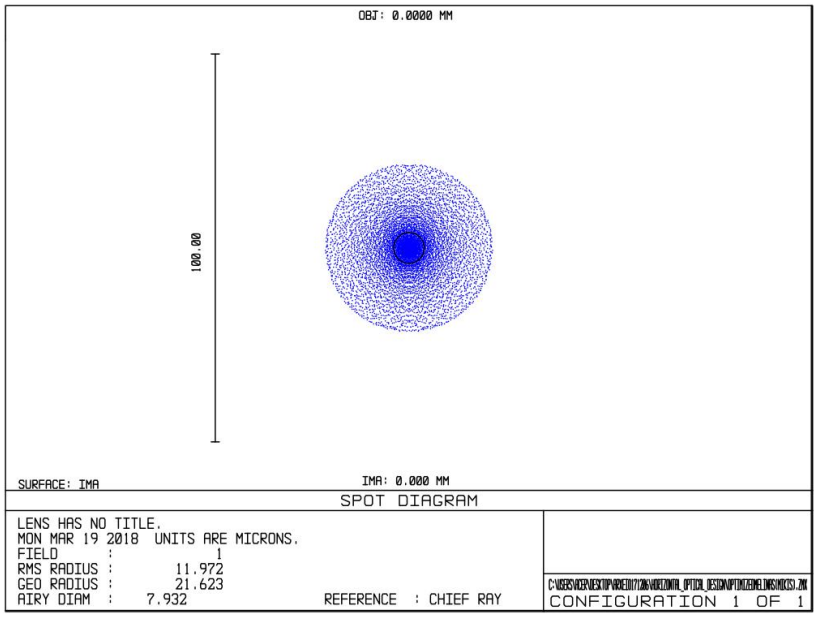

Figure 2.10 .Spot size diagram of the existing optical system. The resolution of the optical system is about 12μm, 3 times larger from the diffraction limit.

The paraxial transverse magnification of this setup is -1(one) so the resolution of the existing optical system at the object space is about 12μm. The diffraction limit is 3 times lower. From the other side the system does not exhibit significant drop at the resolution as it images points that are not on the optical axis. The behavior of the system as the object's distance from the optical axis increases presented at the Figure 2.11.

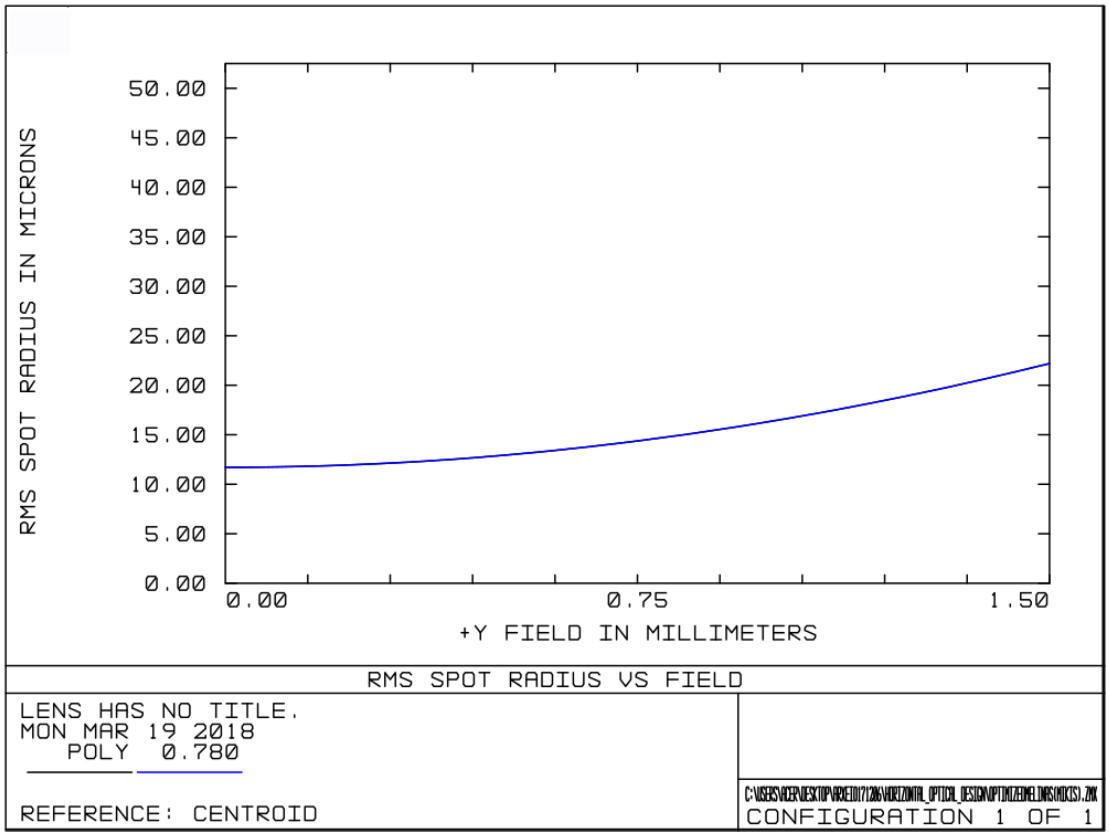

Figure 2.11 Rms vs field. The spot size radius at the image plane as the field increases. One can observe that the resolution does not change dramatically.

These simulations gave us an impression about the expected performance of the new optical system and helped us to reach some conclusions for the optical design process. It was clear that in order to achieve better photon collection efficiency the numerical aperture of the new setup should be higher than 0.11. This means that the effective focal length at the object space of the new optical system should be shorter. Except of the increment at the photon collection efficiency, higher numerical aperture can increase the resolution of an

optical system. Finally, the goal was the design of an optical setup with resolution at object space better than 12μm.

Early steps

Zemax software gives the option to use ideal thin lenses that image paraxially thus stigmatically. That is very helpful at the first steps of the optical design process .The concept is that an object (the cold atomic cloud) emits photons and the optical setup should collect and relay the light on the ccd sensor. In fact this is valid for fluorescence imaging. In absorption imaging method the cold atomic cloud absorbs photons and the optical system should image the localized drop in intensity. After including the basic limitations of the optical design such as the total length of the setup, the diameter of the lenses, the desirable field of view and the paraxial magnification, utilizing this ability that Zemax gives, we planned a first simple design with thin lenses. We set the lenses and after that we optimized the system.

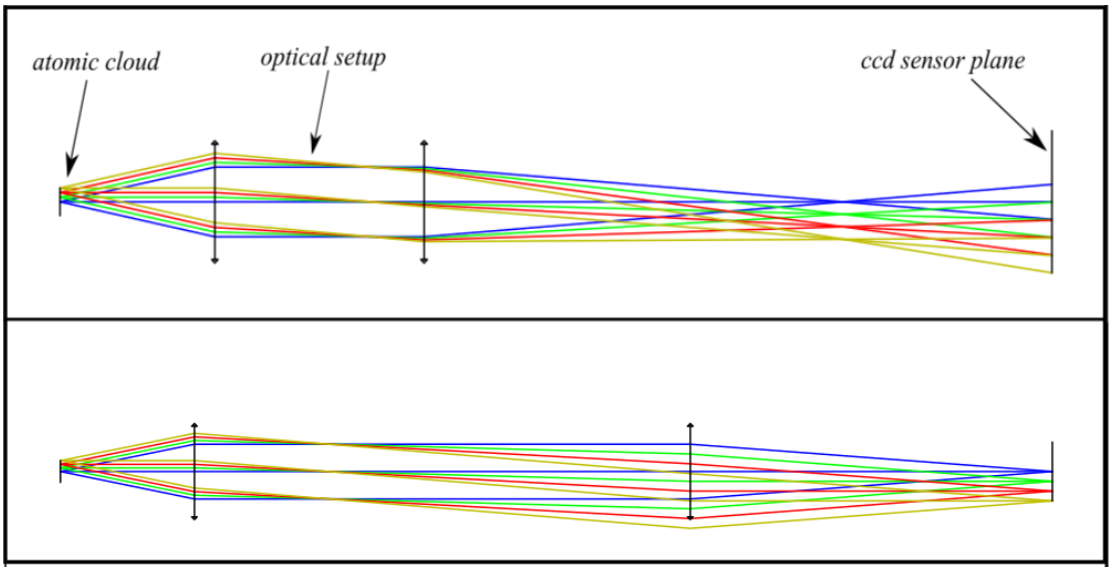

Figure 2.12. .Simple first design with thin lenses before and after optimization. Different colors stand for rays that start from different height at the object space. Red: rays start from highest distance from optical axis, green: rays start from medium height relative to the optical axis, blue: rays start on the optical axis.

This was very important because it gave us a good starting point for the setup layout and the specifications of the lenses, i.e. diameters, spacing, and effective focal length. Even in this simple example one can see how important the optimization of the optical system is. The relative position between the lenses is optimized in order to fulfilled the telecentricity approach and simultaneously the system focuses the rays at the ccd sensor palne.

After that the second step was to add the glass window in the first thin lens design as it is shown in the figure below. The spot size diagram stands for an on optical axis point.

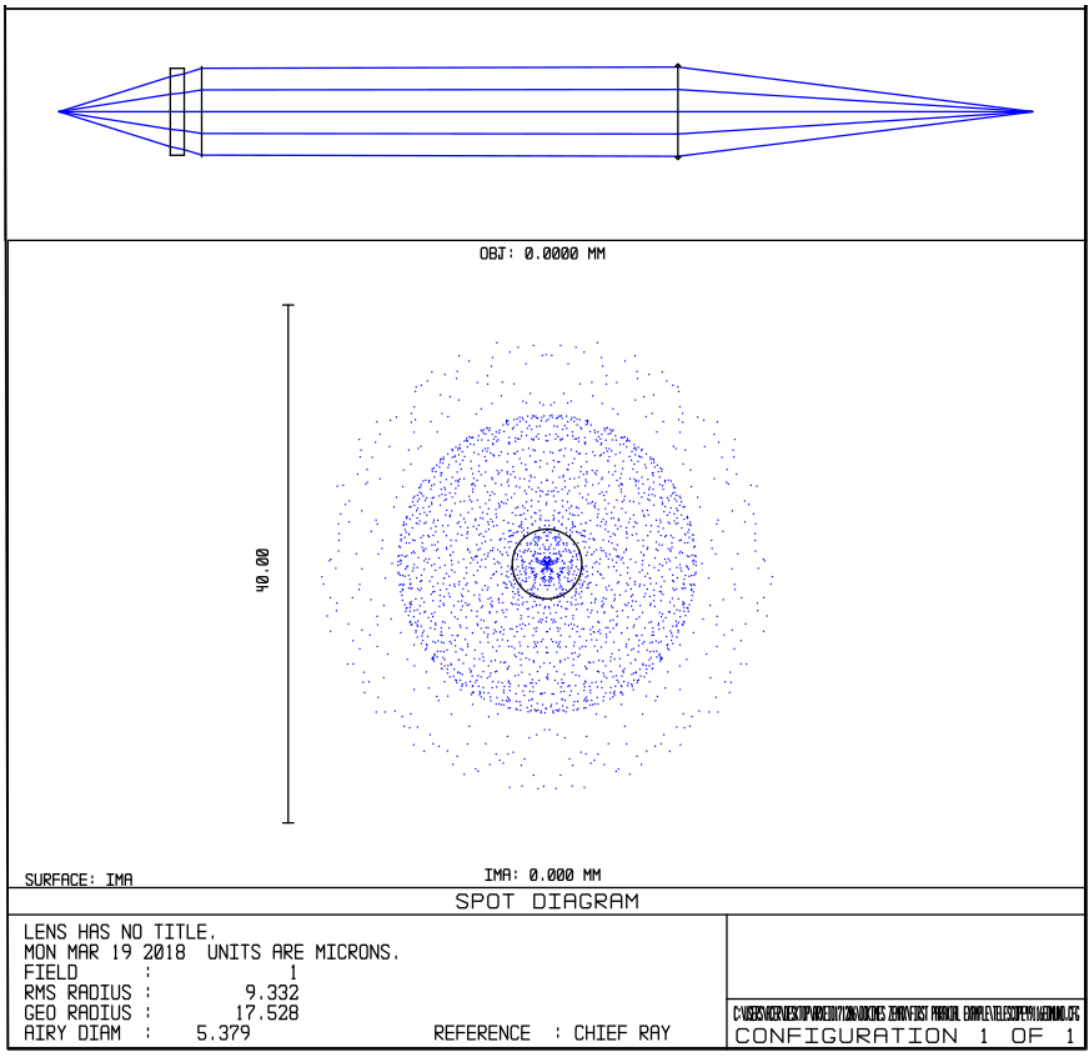

Figure 2.13. The first simple design with the glass window. The spot of the on optical axis point at the image plane is shown at the bottom diagram. The black circle in the center represents the of the Airy disk of a diffraction limited system.

From these early steps it was obvious that the glass window strongly affects the resolution of the system by introducing spherical aberration. Even if the designed optical system consists of perfect lenses the resolution is far from diffraction limit of 2.9 μm radius in this case. This clearly shows that the glass window in such systems is an important optical element of the setup, and should be taken into account in the design process.

At optical design process the first step is the choice of the suitable lenses and the second step is the optimization of the relative positions between them. The facing side that each lens will be placed at optical design process is very important as it strongly affects the resolution of the setup. The optical aberrations that a specific lens induces are dependent on the position and the side that will be placed. After searching different possible system's configurations and combination between the available lenses we reached a final form of the optical system. This configuration has better performance from anyone other than we tested.

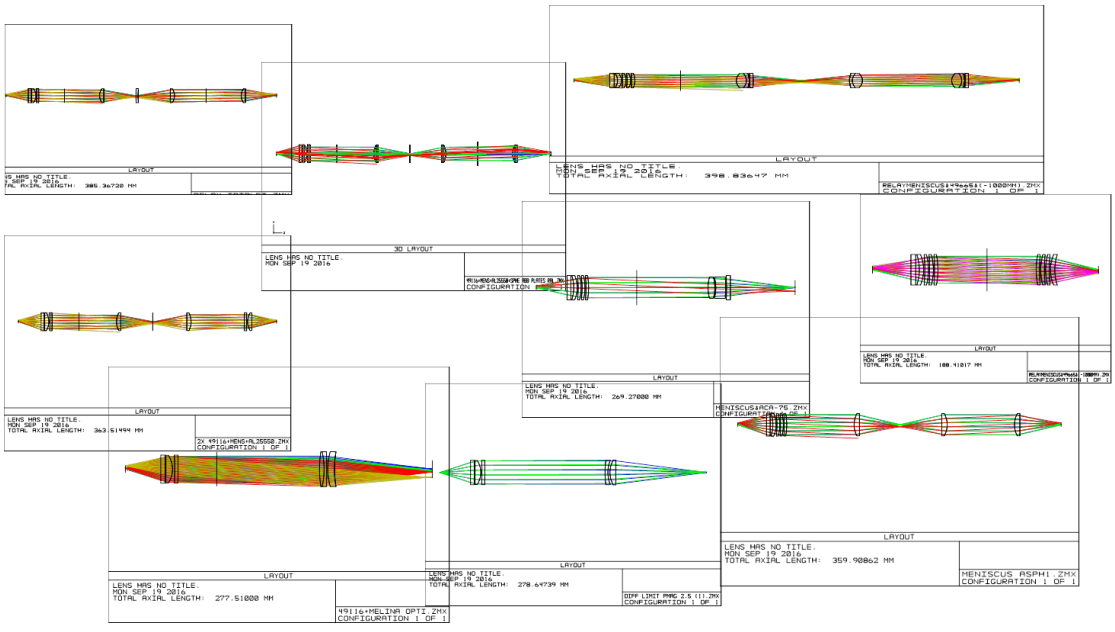

Figure 2.14. Optical layouts of simulated optical systems. Each of them rejected for different reasons.

Some of the configurations that we simulated achieved diffraction limited resolution but they consist of more than 9 lenses. For example an approach that we tried was to design the objective part of the system as a combination of

affordable positive and negative power commercially available meniscus lenses(Figure 2.15).

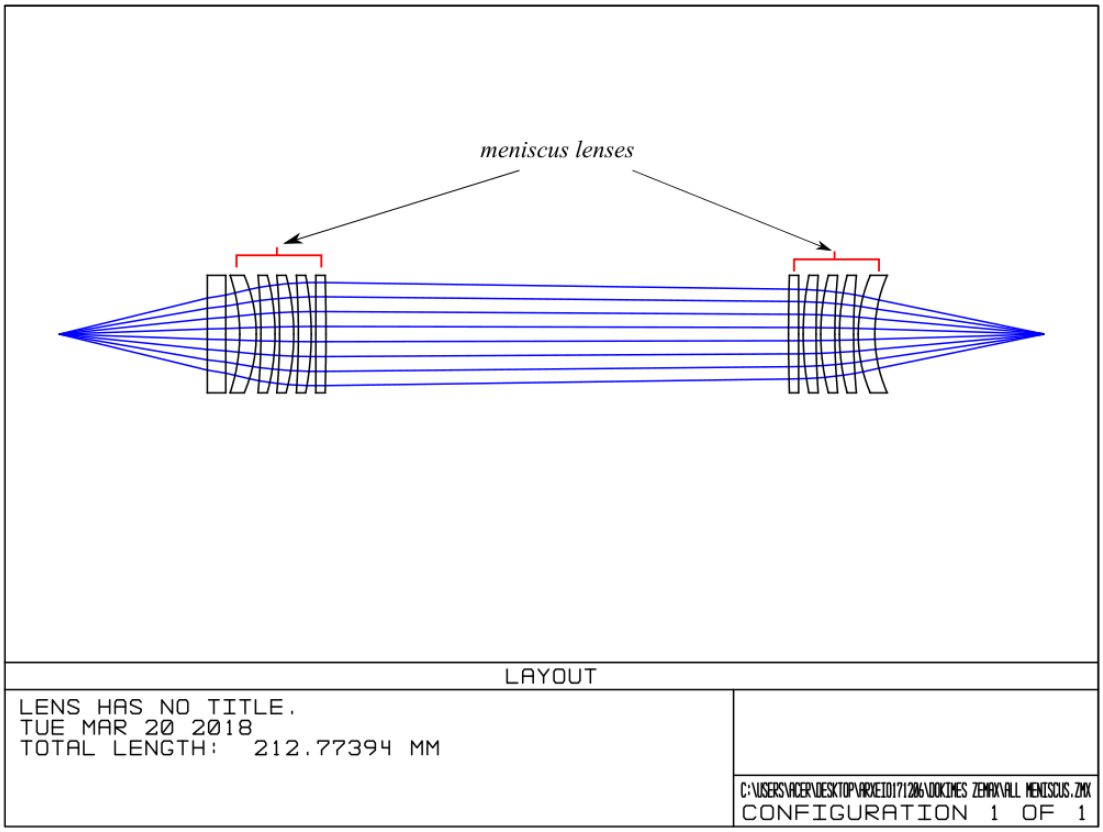

Figure 2.15. An optical design approach for the new optical setup. It consists of meniscus lenses

This configuration gives the option to balance optical aberrations as spherical aberration and field curvature since there are a lot of options at the relative positions between the lenses. This ensures that after optimization process the resolution of the system doesn't have significant variations as it images off axis points of the object. Its resolution is similar to the existing system(14μm). Furthermore the numerical aperture of this system is about two times larger(0.22) than this that achieves the existing optical setup. That configuration was rejected because the number of lenses is large so the signal losses due to the reflections from each lens surface make the optical system inappropriate for fluorescence imaging.

Another configuration that we simulate was to design the optical system with aspherical lenses. This approach is completely different than the previous

one. The system consists of five lenses. Four of them are high precision aspherical lenses (four times the same lens) and a negative power meniscus lens that increases the effective focal length of the objective part of the system. (Figure 2.16). The paraxial transverse magnification is about 1.

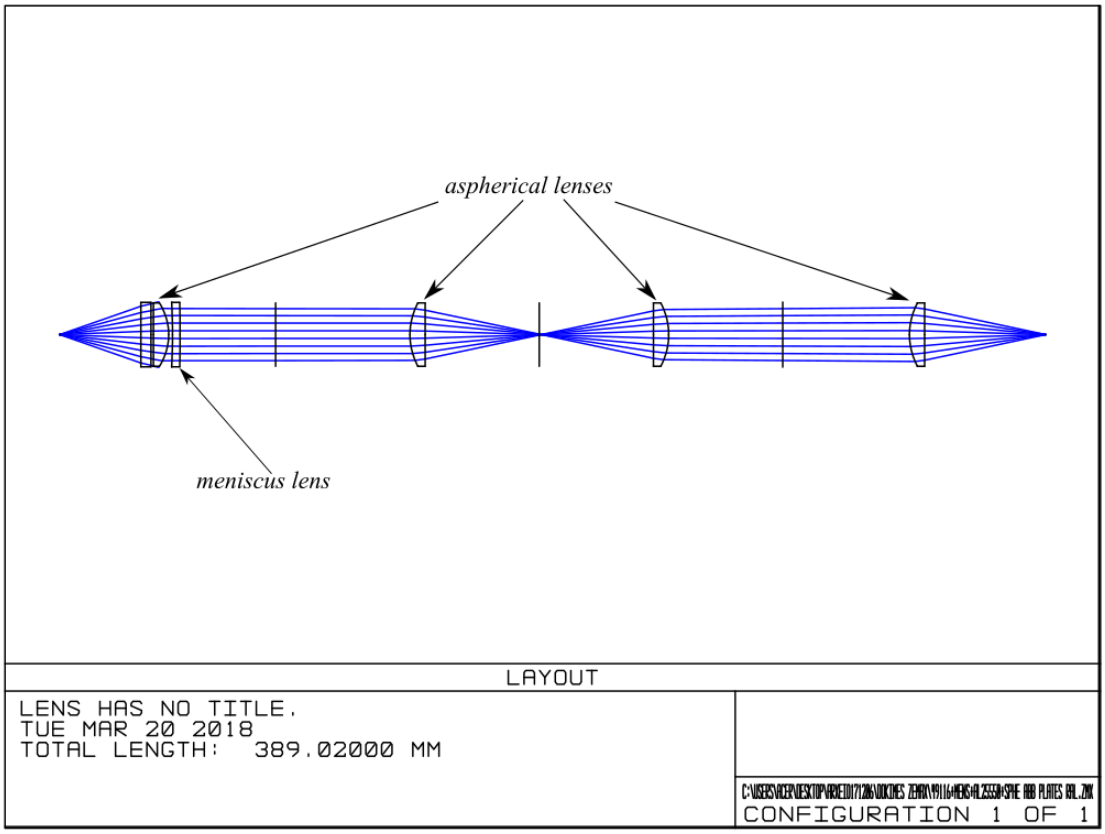

Figure 2.16. A configuration for the new optical system. This optical setup consists of high precision aspherical lenses and a negative meniscus lens

The performance of this system is satisfying at the most of the domains that we were interested about. The resolution at central field is 6.5 μm and the numerical aperture is 0.29. The number of lenses makes the system appropriate for fluorescence imaging experiments. From the other hand, except of the high cost for its implementation, this setup has a great disadvantage. Its resolution drops fast as the field increases. At 1mm radius of field the resolution at object space is about 70μm and at 2mm field is up to 225μm.(Figure 2.17).

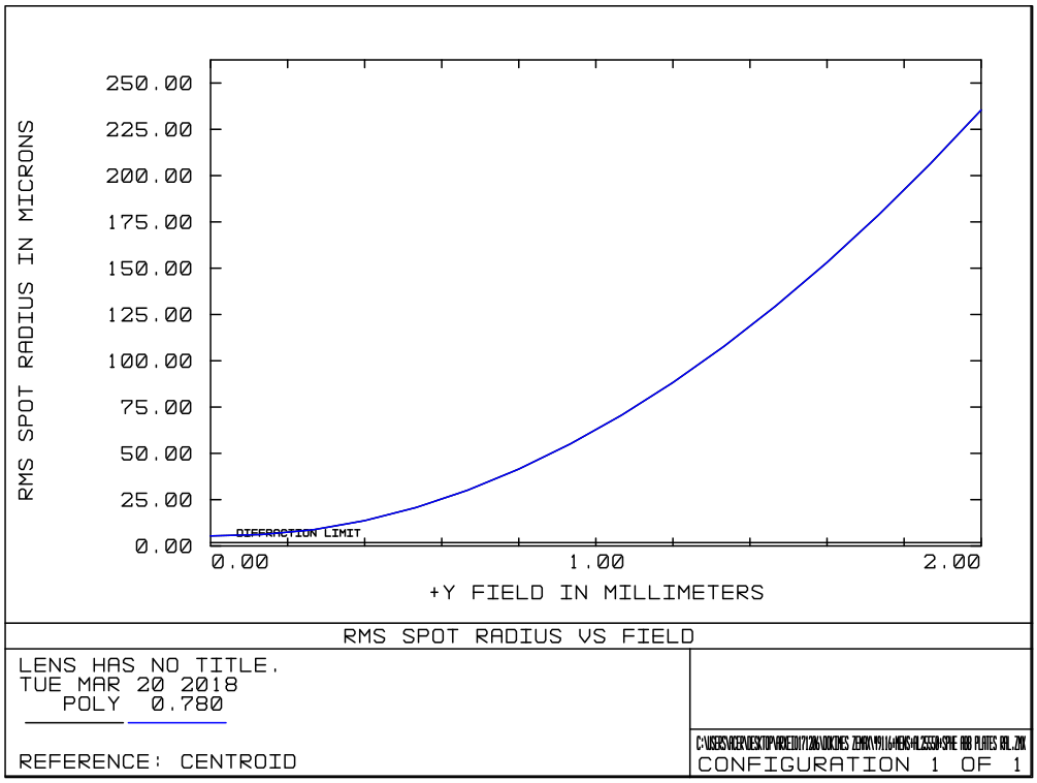

Figure 2.17. Rms vs field diagram. At this diagram can be shown the resolution of the optical system as the field increases

Layout of the final optical system

Finally we reached an optical setup that exhibits satisfying performance and simultaneously fulfills the constraints described above. Its characteristics and performance described in details below. An optical layout of the final setup presented at the Figure 2.18.

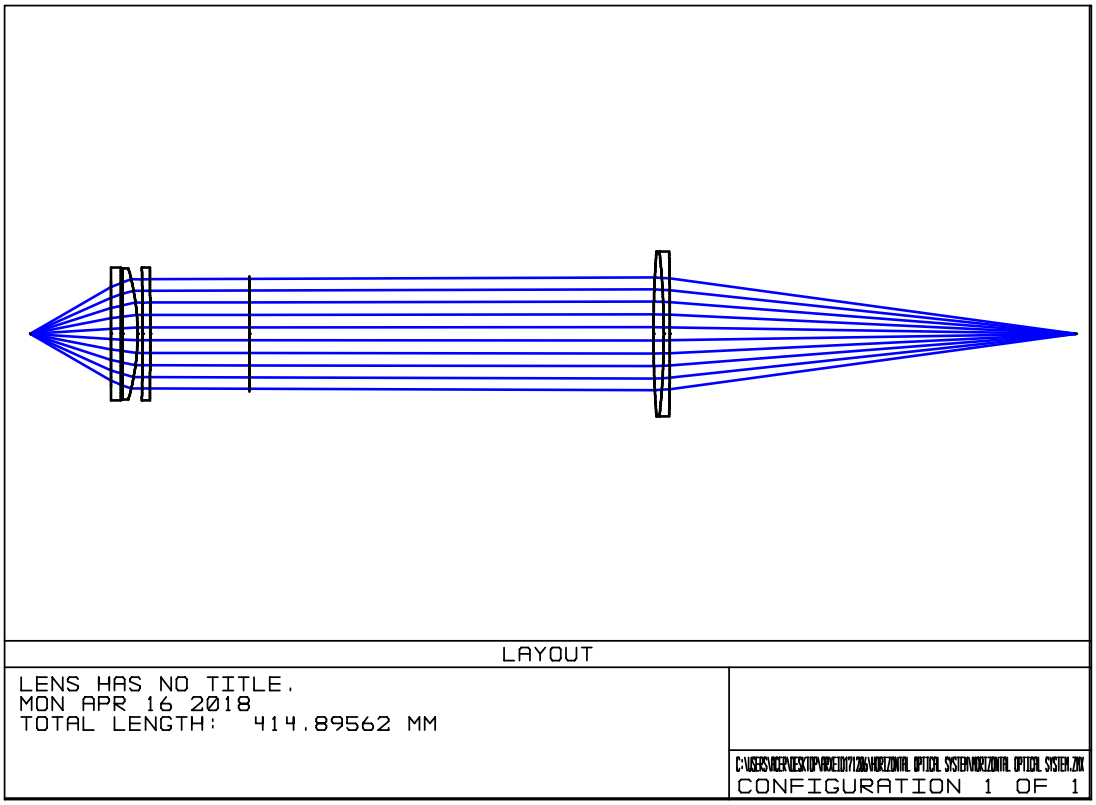

Figure 2.18. A schematic of the final optimized setup taken from Zemax. At this figure appears the glass window that exists before the optical system(first element).

At the table below briefly presented the new optical system's characteristics and its performance. At the pages below there is an analytically discussion about them.

Total length(first lens until image plane)	378.23
Physical total length	217.25mm
Working distance	37mm
Numerical aperture	0.30
Transverse paraxial magnification	-4.1
Resolution	Diffraction limited
Number of used lenses	Three
Design approach	Doubly telecentric

Table 5 . Performance and characteristics of the new optical setup.

As it is shown at the Figure 2.18 the system consists of three lenses. The first lens is an aspherical with effective focal length of 37.5mm and the two others are meniscuses of effective focal lengths are -400mm and 160mm respectively. Before the first lens there is the vacuum cell in which the atomic cloud is created. The total length of the setup from the first lens to the image plane and the length from the first lens to the last lens of the setup are 378.23mm and 217.25mm respectively. The numerical aperture that this configuration achieves is 0.3.

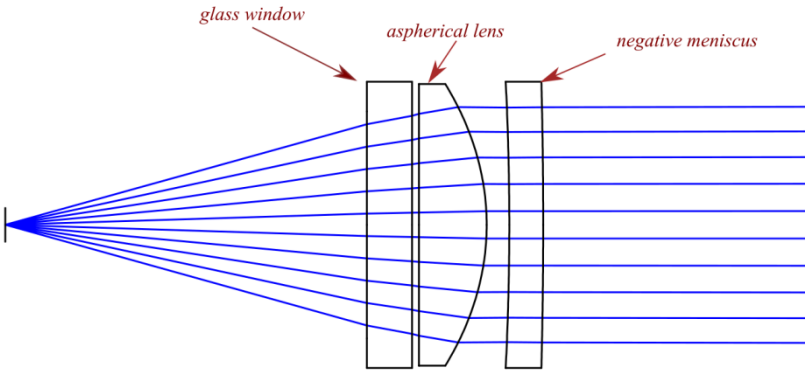

Figure 2.19 A more zoomed optical layout that shows the first part of the optical setup.

The first lenset consists of a powerful aspheric plano-convex lens, which ensures high photon collection ability, and a meniscus that helps us reduce optical aberrations. This configuration enables the optical system to be placed as closer as possible to the vacuum cell, thus maximizing the NA which is limited to 0.31 due to the geometrical characteristics of the device.The optical system's configuration is double telecentric.

Finally, the effective focal length of the first lenset and the second lens is 39.41mm and 160mm respectively so (due to the telecentricity) the transverse paraxial magnification of the system is about -4.1. A script of Zemax for the designed optical setup presented at the figure below. At this script all the characteristics of the lens and the distances between them can be shown.

	Surf:Type	Comment	Radius	Thickness	Glass	Semi-Diameter		Conic
OBJ	Standard		Infinity	32.000000		1.500000		0.000000
1*	Standard		Infinity	4.000000	SILICA	10.063534	U	0.000000
2*	Standard		Infinity	0.600000		12.700000	U	0.000000
3*	Standard		Infinity	6.000000	L-BAL35	12.500000	U	0.000000
4*	Even Asphere	49116	-22.092000	2.000000		12.500000	U	-2.271309
5*	Standard		-253.190000	3.000000	N-BK7	12.700000	U	0.000000
6*	Standard	LF1141-B	-500.000000	39.410000		12.700000	U	0.000000
STO*	Standard	iris	Infinity	160.340000		11.000000	U	0.000000
8*	Standard	LAO 155	106.070000	4.100000	SSK4A	15.750000	U	0.000000
9*	Standard		-72.690000	2.400000	SF8	15.750000	U	0.000000
10*	Standard		-484.140000	161.049574		15.750000	U	0.000000
IMA	Standard		Infinity			6.438365		0.000000

Figure 2.20. Zemax script for the new optical setup. All the information about the lenses and the distances are included.

A 3-D representation of the optical system placed next to vacuum cell can be shown at the figure below.

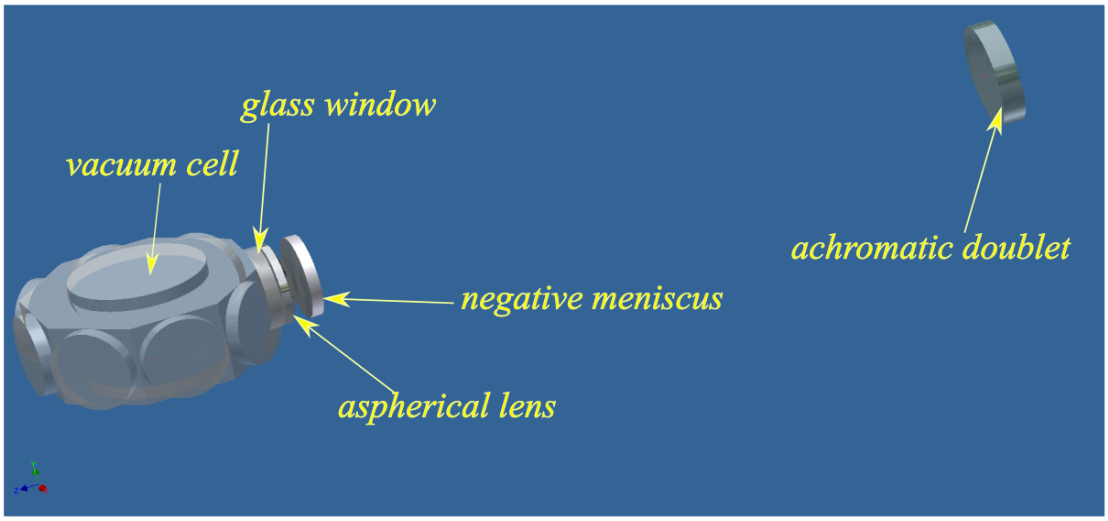

Figure 2.21. A 3-D representation of the optical setup. Yellow labels notice the optical elements in the setup.

Optical System's performance

At this section we present the performance of the designed optical setup. Zemax software has a plethora of diagnostics graphs and computational methods, providing the ability to a depth evaluation of setup's performance. Firstly is presented the resolution performance and after that the photon collection ability of the setup.

Resolution Performance

At the graph below the spot diagram of the system at image plane is shown which, in our case, is the ccd's sensor plane. The spot diagram shows the image of a point object source. The spots refer to four different point objects located at different heights on the object plane (0.0 mm, 0.4mm, 1mm, and 2mm). Since the optical system is spherically symmetric, the tests were performed using fields in the vertical direction.

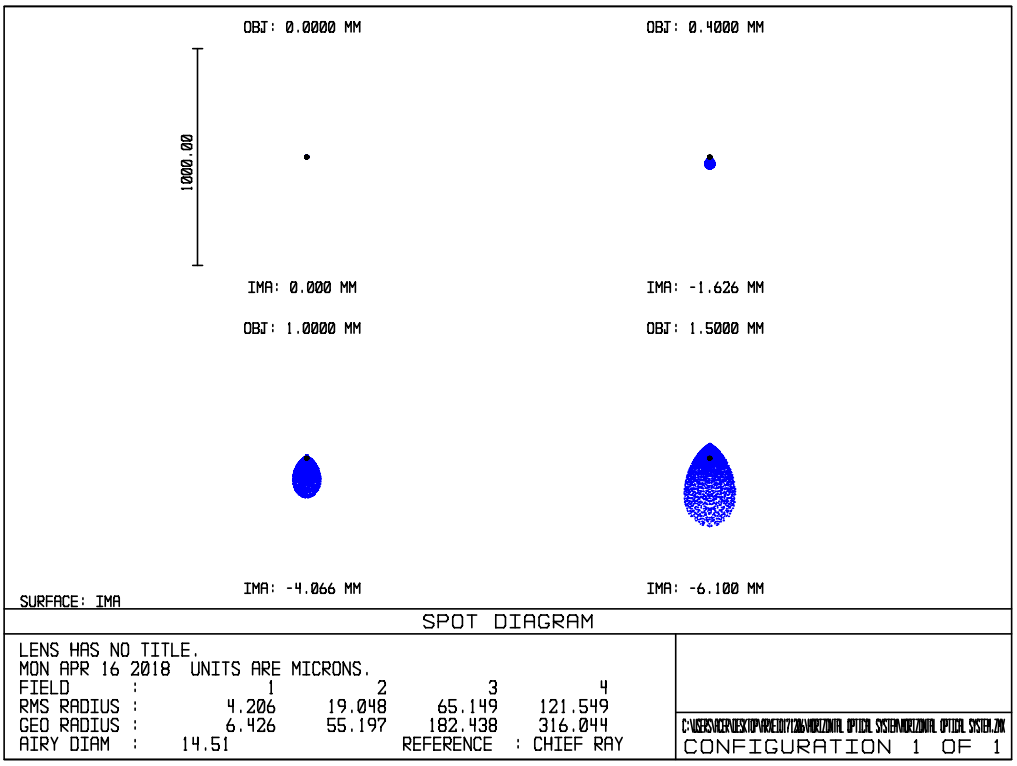

Figure 2.22 Spot diagram of the setup. Especially the spot diagram for: zero field, 0.4mm, 1mm, and 2mm respectively. It must be noted that at the zero (and near zero) field the spot is diffraction limited. The scale is 1000um (1mm).

The resolution of the system at object space is about 1.2 μm as estimated by the ratio of the spot size image plane to the paraxial magnification of the optical system. This refers to the resolution of the system at the zero field where it is diffraction limited.

At the next diagram is shown how the spot size evolves as the object height increases. The black line at the bottom of the graph denotes the diffraction limit.

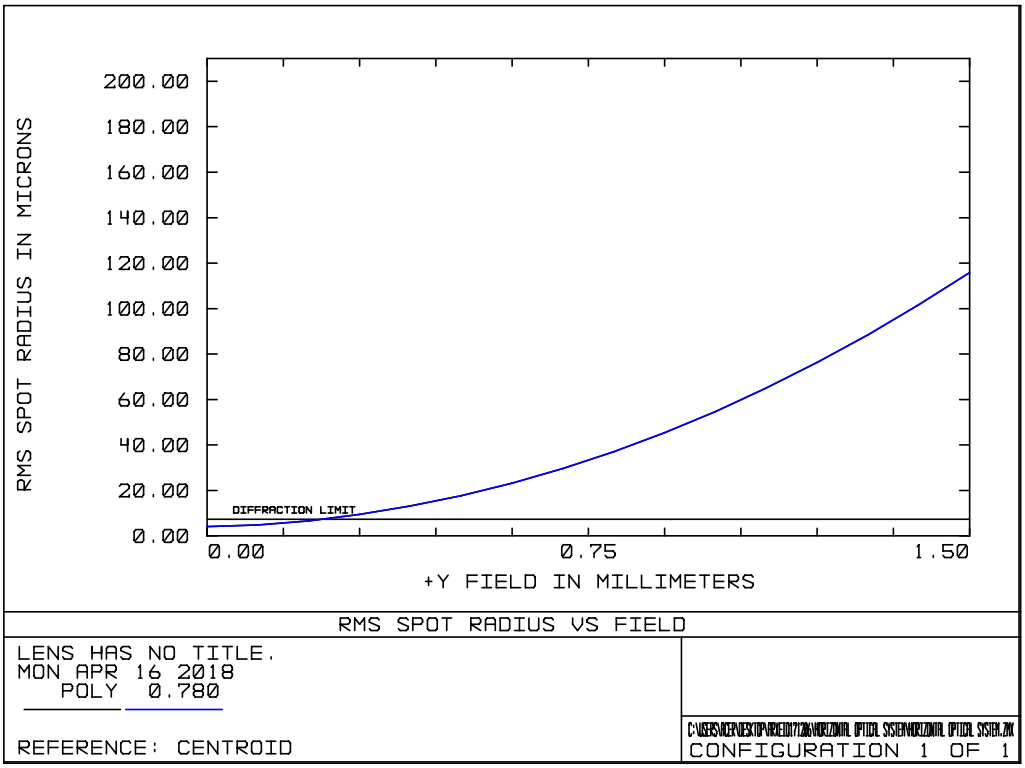

Figure 2.23. RMS spot radius vs field. At this graph is shown how the spot radius changes as the object's height increases.

At the next diagramm one can see the Seidel aberration analysis diagram .This diagram shows the main optical aberrations with maximum scale 500μm, induced from each lens' surface and their total contributions to the system. At this diagram one can see the optical aberrations (especially spherical aberration) that the glass window induces (surface 1&2) and how these were reduced after optical design process. An idea is to apply the technique that is described at chapter 1.2.3, the use of a flat glass plate in order to reduce further the spherical aberration of this system. Actually the Numerical aperture of this system at image plane is small (about 0.07) and the gain at resolution is will be negligible.

At the diagram below it can be seen how the resolution evolves as the field increases for the existing and the new optical setup that we designed. At small fields the resolution of the new optical setup is much better (about 8 times) while at the large fields is lower.

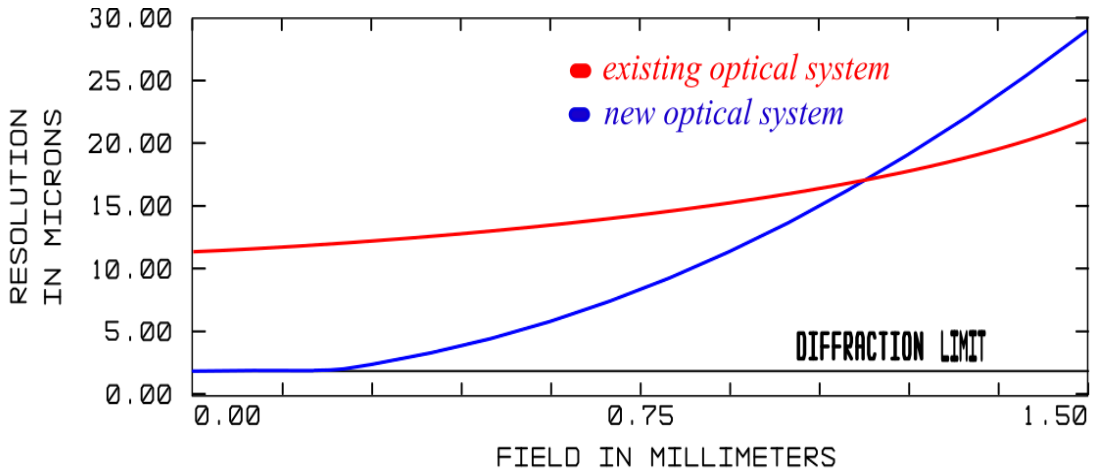

Figure 2.24. Resolution of each optical system as a function of the field. The blue line stands for the new optical setup when the red stands for the existing one. The black line at the bottom is the diffraction limit for the new optical system.

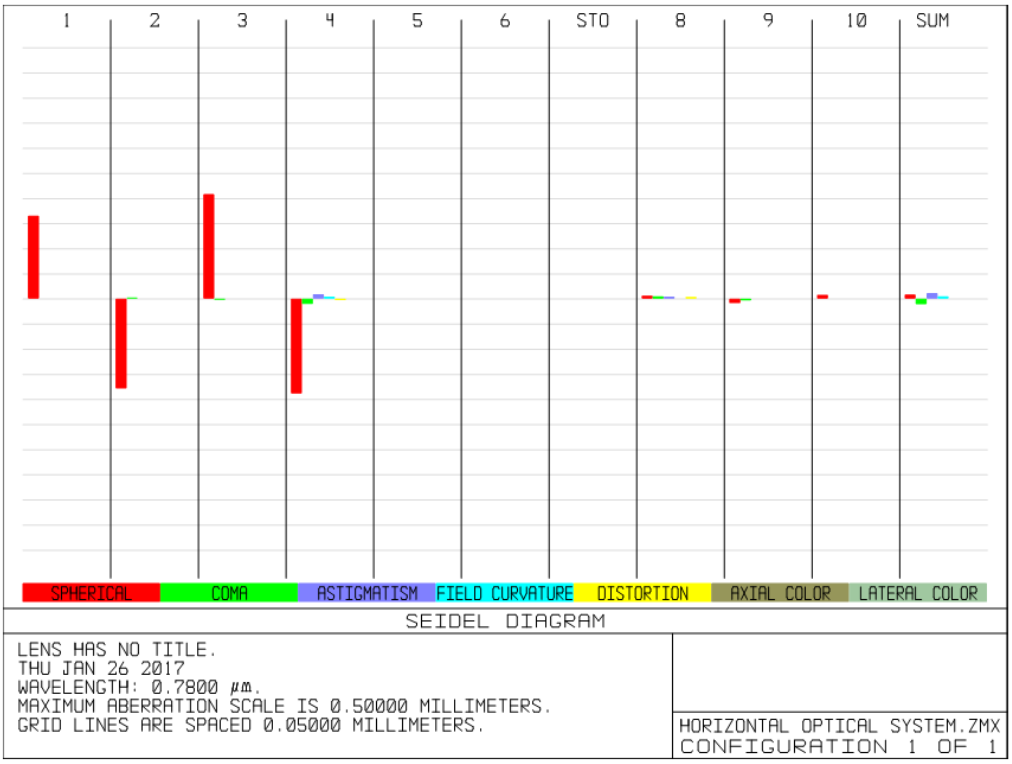

Figure 2.25. Optical aberration diagram. Aberration that each surface induces . Right side of the diagram shows the summed aberration after the optical design process.

Finally, Figure 2.26 shows the footprint diagram (ray projections for all object heights 0 mm, ± 0.4mm, ±1mm, ±1.5mm on the sensor). The black square displays the actual size of the ccd sensor.

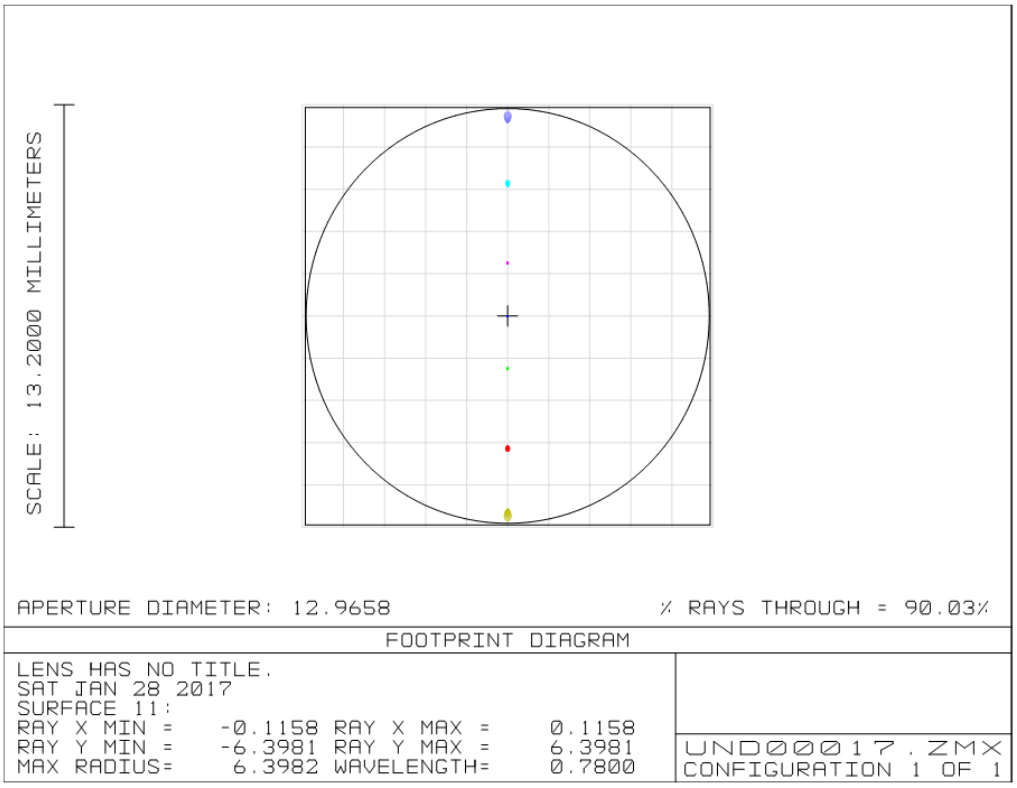

Figure 2.26. Footprint diagram of the setup. The different colors correspond to focused rays at ccd sensor (black square) for different fields.

Photon collection Performance

As mentioned above the system will be used for atomic cloud imaging and for fluorescent imaging simultaneously so the performance at atomic cloud emission photon collection was crucial. The achieved numerical aperture of the setup is ~ 0.3. At the next plot the vignetting effect as the field increases is shown. Until 1.2mm radius of field all the emitted light, passing through the optical system without losses.. At the following vignetting diagram a comparison of the new and the existing optical system presented. At this diagram can be shown that for fields up to 300μm the vignetting effect is more intense at the existing optical system. At 1.5 mm filed new optical setup ensures that the 92% of the emitted rays reach the ccd sensor while this number is 79% for the existing optical system.

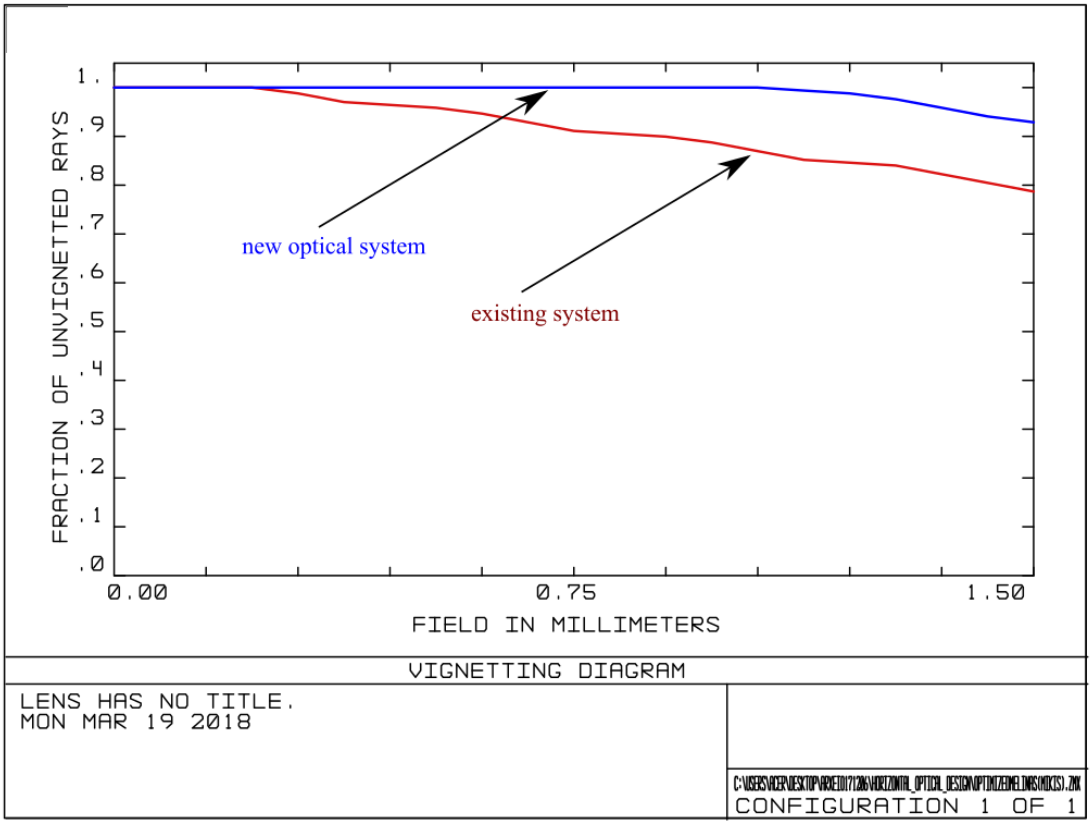

Figure 2.27. The y-axis represents the friction of unvignetted rays and x-axis the radius of the field (in mm).The blue line represents the performance of the new optical setup and the red one of the existing system.

Discussion

To conclude, we designed a new imaging optical system in order to upgrade the existing one in Matter waves laboratory at I.E.S.L, Forth. The resolution of the existing optical system is about 10μm and its numerical aperture is about 0.11. and it is comprised by three lenses. The new optical system has about eight times better resolution and it diffraction limited up to 250μm object height. We achieved to increase the resolution about 8 times since we increased numerical aperture almost three times. The numerical aperture of the new optical setup is about 0.3, which means that the brightness of the image is about 9 times higher (the image brightness is proposal the squared numerical aperture). Finally the new set up consists of three lenses; one less than the existing and this is an obvious benefit for reducing transmission losses. So it is obvious that the new optical system is better by far at these domains than the

existing one. On the other hand the new set up has worse resolution at high fields (up to 1 mm radius of field)but the difference is small, for 1.5 mm field the resolution of the existing optical system is about 23 μm and for the new one is 30μm. . As a future work we will adapt this optical system in the experimental device of the laboratory in order to replace the existing optical system thus the performace of the new optical system will be upgraded.

2.1.4 Implementation

After the successful raytracing simulation analysis that confirmed that the optical design fulfilled the specifications we continued with the opto-mechanical design. At this point is important to refer that the opto-mechanical design concerns all the optical elements including beam guiding mirrors, etc.. Another crucial parameter was that the opto-mechanical design should be functional for two different detection cameras. Thus, besides the custom lens housing tube we designed a new breadboard to layout all beam guiding optical elements (mirror mounts etc.), adapters for both cameras and base for the lens tube. In this opto-mechanical design we also used commercially available mechanical parts as translation stages, mirror mounts and a 90 degrees adaptor. The goal was the successful integration between the commercially available and custom made parts. All the custom made parts were designed in Autodesk 3D CAD software and manufactured in IELS workshop.

Opto-mechanical design

Custom lens housing tube.

The lens housing part was the main custom part and its design was the most demanding by far, since high precision was needed. The most critical part was the first part of the lens housing tube, which was fabricated with 100 μm precision..., This first part (Figure 2.28) houses the two first lenses which are

responsible for the collection of the emitted photons and the elimination of the main part of the optical aberrations. In order to achieve the best possible performance of this system, the distance between the aspherical lens and the glass window of the vacuum cell should be smaller than 1mm.

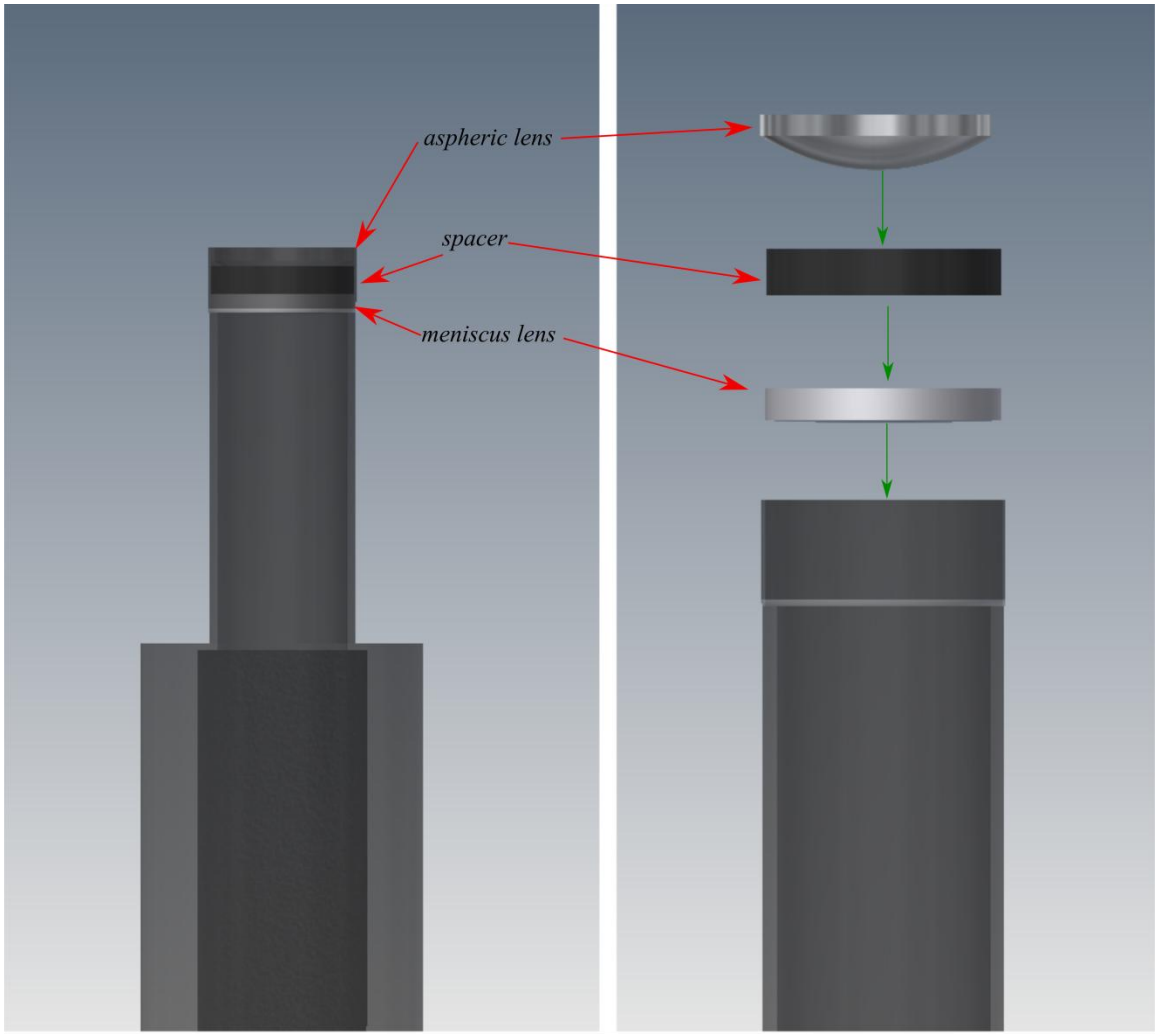

Figure 2.28. Lens housing first part. Right: A side view of the objective's part opto-mechanical design. Left: The way that the optical elements inserted in the lens housing tube. A specific length spacer ensures that the distance between the two lenses is well defined.

This means that the lens housing should be inserted in one of the macor's threaded holes as it can be seen in Figure 2.29. This led us to design a very thin spacer for the part that the 1inch diameter lenses were inserted.

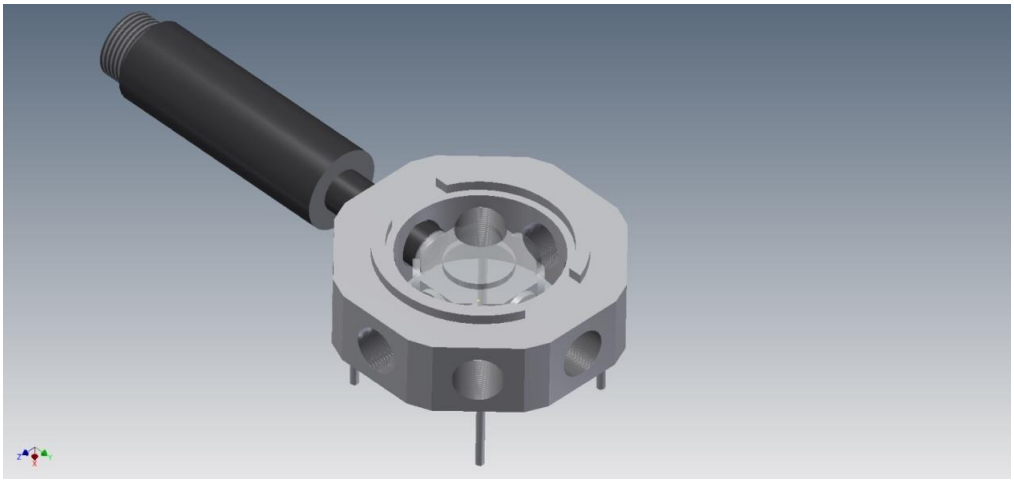

Figure 2.29.Opto-mechanical drawing of the objective, the macor and the vacuum cell. At this figure the way that all the parts are designed to fit together is shown. The lens tube is putted very close to the glass window.

In addition the length of this part was set such that there is no physical contact between the glass window and the aspherical lens to avoid scratches during assembly but also Fabry -Perrot cavity effects. Furthermore the design of the lens tube ensures that the relative distance between the aspheric lens and the glass window will be stable. The mechanical drawing of the lens tube can be shown at Figure 2.30.

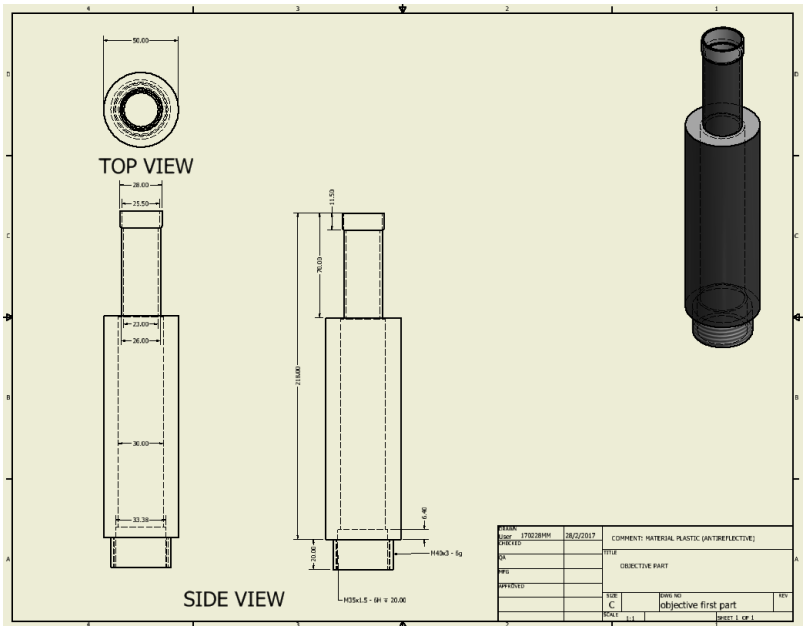

Figure 2.30 Lens housing opto-mechanical drawing. The opto-mechanical drawing that the machine shop used in order to construct the custom design lens mount.

The lens housing should not be metal in order to avoid Eddy-currents near the magnetic trap. Under these circumstances we decided that the most proper material for its construction is the ertacetal (plastic). Especially in matte black color in order to avoid reflections in the tube interior. The bottom part of the lens housing is used in order to mount the third lens of the optical design. The distance between the first lenset and the last lens matches exactly the sum of the focal distances of the first and the last lenset, to ensure the doubly telecentric configuration of the optical setup.

Other custom designed parts.

For a lot of parts it was necessary to design them from scratch. These parts were used as adapters, base for the optical system, adaptor for mirror, spacers, adaptors for both cameras and a breadboard for supporting the whole system. There were a plethora of restrictions and spatial limitations since the available space in the experimental device is confined. An extra complication was that all the custom made parts should fit to the commercial ones and that the whole system should be compatible with two different sensors. In our final design, an adaptor is used to fit each sensor on the system as shown in Figure 2.31.

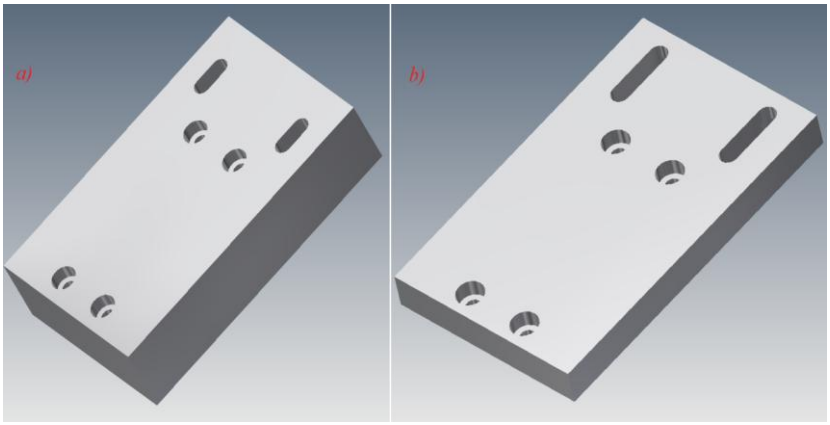

Figure 2.31. Adaptors for cameras holding. Two custom designed aluminum adaptors with different dimensions In both cases the adaptors connected with translation stages in the circular holes and with ccd cameras in slot holes. a) Adaptor for Andor i-Kom camera. b) Adaptor for Andor i-Xon camera.

Except of the adaptors and the lens housing tube we designed and constructed various parts in order to mount the optical and the mechanical items of the setup. Information for these items can be found in the Appendix B.

Adapting to the BEC system (mechanical parts)

As it referred above commercially and custom made parts are combined in order to complete the opto-mechanical design. Every distance is measured and all the items fit together. The optical setup now fits to both ccd cameras. Mechanical drawing of total assembly for Andor i-Kon and i–Xon cameras are presented below. At both drawings, custom designed individual parts are marked with red labels and arrows. First, the opto-mechanical setup with the Andor i-Xon ccd camera is presented (Figure 2.32).

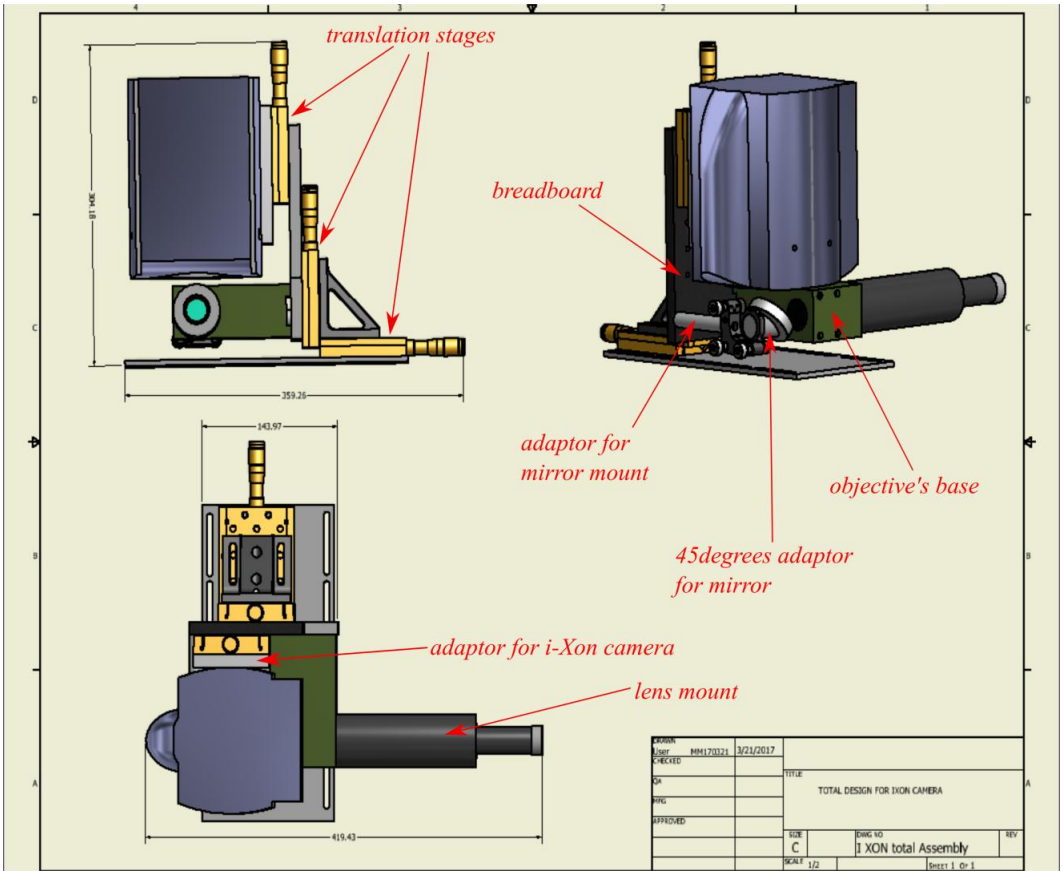

Figure 2.32. Total assembly of the opto-mechanical design for i-Xon ccd camera. Custom designed parts are red marked. All the distances are specific and the parts fit together in order the whole setup get ready to replace the existing one.

The second opto-mechanical drawing shows the total opto-mechanical assembly for the second design for the Andor i-Kom ccd camera (Figure 2.33).

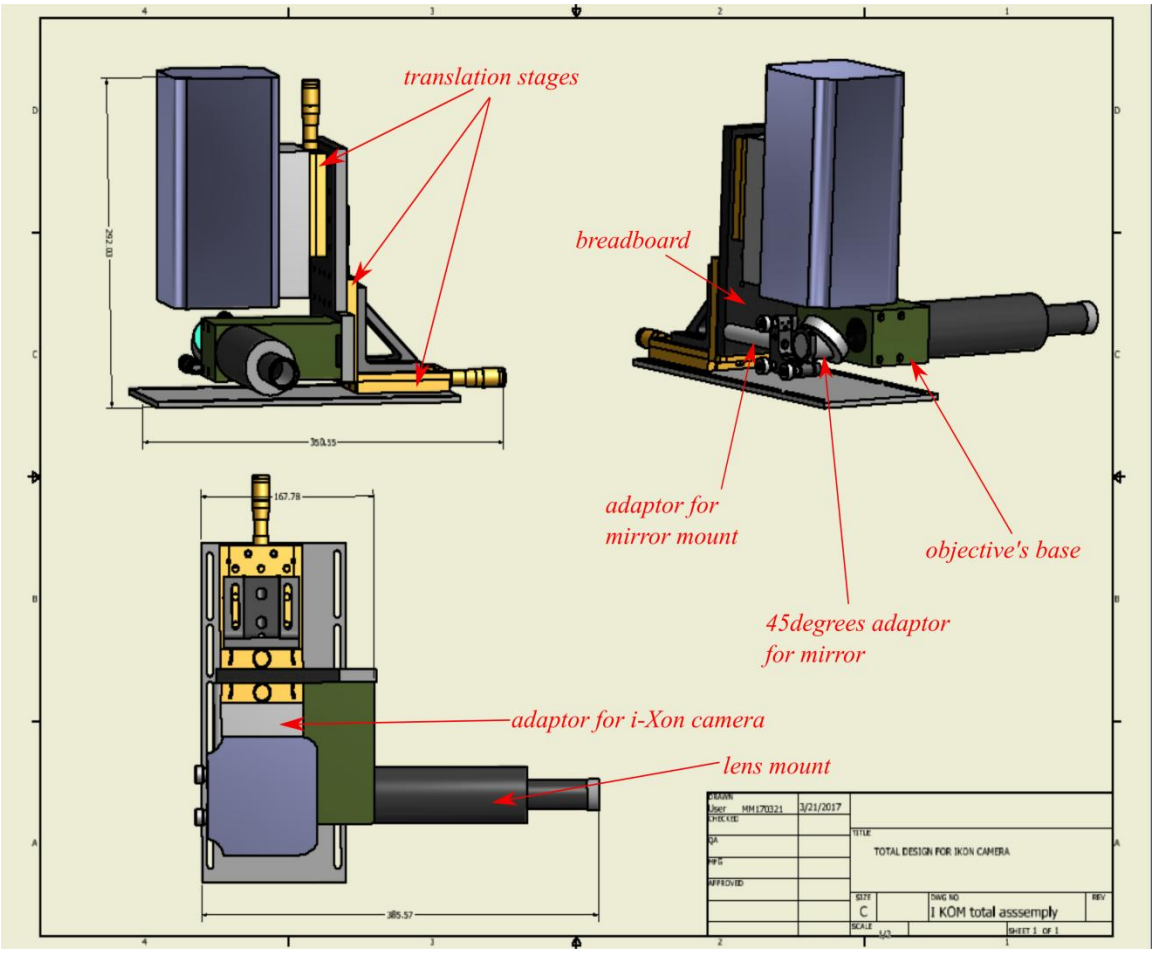

Figure 2.33 Total assembly of the opto-mechanical design for i-Kom ccd camera. Custom designed parts are red marked. All the distances are specific and the parts fit together in order the whole setup get ready to replace the existing one.

2.2 Non-destructive imaging of an atomic cloud: Optical design

2.2.1 Description and aim of this project

Ultra-cold atoms have demonstrated a great potential for both technological and fundamental science applications. Over the last two decades the cold-atom physics has matured from proof-of-principle demonstrations to a versatile platform for precision measurements and study of quantum phenomena. In order to fully exploit the possibilities of cold-atom physics, it is important to have a precise control and characterization of the atomic cloud. In particular, the number of atoms in the ensemble plays a significant role in the interpretation of measurements with cold-atoms. On one hand, in most of the experiments the useful information to be extracted from the system is encoded ultimately in the number of atoms in the ensemble. Uncertainty in the number of atoms is directly translated into imprecision of the measurement. Furthermore, due to atomic interactions, the dynamical evolution of the system depends on the number of atoms in the cloud. Accurate knowledge of the atomic density is therefore required for precision measurements. For instance, uncertainties in the density dependent collisional shifts are currently limiting the precision of atomic clocks. In addition, sensitivity enhancement squeezing techniques rely on atom number characterization either by employing atomic interactions or by measurement-based conditional squeezing. Crucially for these applications, the atom number measurement should be minimally destructive: atomic coherences should not be disturbed by the measurement process and the energy deposited to the atomic cloud should be small compared to the average energy in the trap. Contrary to the case of absorption or fluorescence imaging, atom number measuring techniques that rely on the dispersive interaction of light with the atomic cloud meets these rather stringent requirements. In this thesis, we perform the first steps in exploring the possibility of using dispersive imaging based on polarization rotation of light in order to perform a robust and precise characterization of the atomic density in a minimally disruptive way [17]. We

aim to reach a measurement imprecision below the shot noise of typical atomic clouds (on the order of 10^5 atoms).

2.2.2 Specification of the Optical System

As it was described above the optical setup that will be used in this experiment a Gaussian beam interacts with the atomic cloud. After the interaction between the photons and the atomic cloud this beam should reach a beam splitter that splits the beam in two perpendicularly polarized beams. The intensity difference as measured from two balanced photodiodes is the signal. The setup described in the following pages constitutes the main part of the atom number experiment. An optimization of a plethora of parameters is required for the successful implementation of such an experiment. . After constructive discussion and taking into account the restrictions we decided the expected characteristics of this optical setup.

Expected characteristics of the optical setup- limitations

Resolution

This optical setup will be used for the measurement of the number of atoms. Since it is not aimed for imaging, the optics are not optimized for achieving the highest resolution. Instead the optical setup is designed so that the beam interacts with the atomic cloud in a way that optimizes the signal to noise ratio in the atom number measurement. The atom number characterization is fundamentally limited by the photon shot noise of the probe light and the unavoidable stochastic loss of atoms from the interaction with the optical probe. At the same time the loss rate of atoms should be kept small compared to the (transverse) trapping frequencies, so that the atomic distribution adiabatically follows the probe induced loss of atoms. The exact beam size for best signal to noise ratio goes beyond the scope of this thesis. However, we estimate that the above limitations and constraints point to an optimal probe beam size comparable to the size of the atomic cloud (Figure 2.34). This means that for our experiment the beam waist should be roughly in the range of 8-18μm.

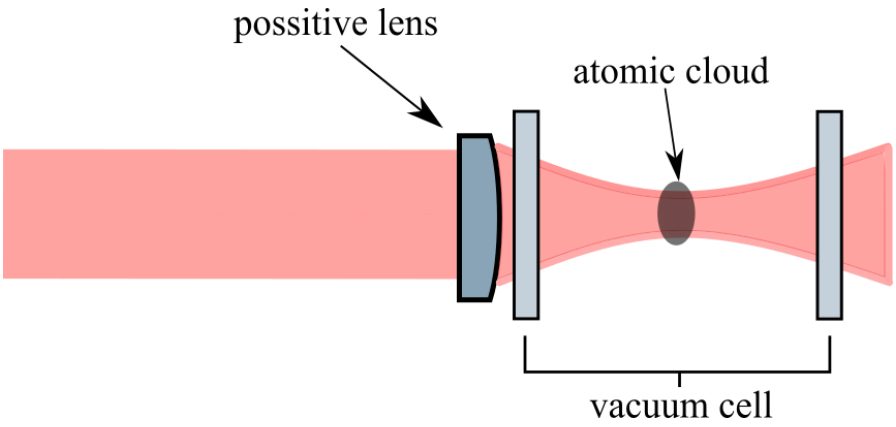

Figure 2.34 A schematic representation of the passing beam and the atomic cloud interaction. The optical setup should ensure that the diameter of the beam there is comparable with size of the atomic cloud.

From the other side if the size of the beam waist is more than 17μm the noise of the measurement goes high. So the resolution at this part was restricted in a lower and an upper limit. Except of this optical setup's part the need for resolution was not very high. The photodiodes, that were used to detect the beam after the interaction with the atomic cloud, have a square 4mm X 4mm photoactive area. This means that the final part of the setup which is responsible for focusing the beam on the photodiodes should ensure that the diameter of the beam will be at least 2-3 times smaller than the area of each photodiode.

Illumination-Transmission losses

In this nondestructive atomic cloud imaging experiment the theoretical prediction for the absolute value of the under detection signal was the order of a few nanoAmps. That means that the under detection signal is really weak so the minimization of the transmission losses is vital for the success of the experiment. This is an important restriction since it the system should by comprised of the minimal number of optical elements possible. Another very important parameter is to use antireflection coated, at the laser beam wavelength (780 nm) optical components. Last but not least, the used optics should be much larger than the beam diameter in order to avoid beam clipping effects

Commercially available optical elements

In the process of optical design, the goal is to design and implement an optical setup that will meet certain criteria. There are two main paths in the optical design process. The first is to use commercially available optical elements. This solution has typically the lowest time and money cost but there are limitations in the items that can be used in the optical setup. The second path to optical design is to develop custom made optics. With this solution the user designs new optics that are suitable for the specific problem. This is time consuming and the cost for the custom designed lenses is typically several times higher than this of the commercially available. In the setup described in this thesis, we decided to use commercially available optical elements since this solution is affordable and simpler than the other. A lot of companies offer high quality optics with the desired characteristics.

Spatial limitations

The nondestructive atom cloud imaging is not the only experiment in this laboratory. In fact the under construction experimental setup should integrate in the main experimental device of the lab. The experimental setup of the new experiment consists of the main experimental device of the laboratory plus the new optical setup and the electronic devices/elements. The atomic cloud is created at the main device of the laboratory; the new optical setup should ensure the efficient light-atomic cloud interaction and the collection of the signal at the photodetectors. Furthermore, electronics' support is necessary for that signal detection and analysis. Spatial restrictions include integration issues within an dense and operational laboratory setup as shown in the figures below.

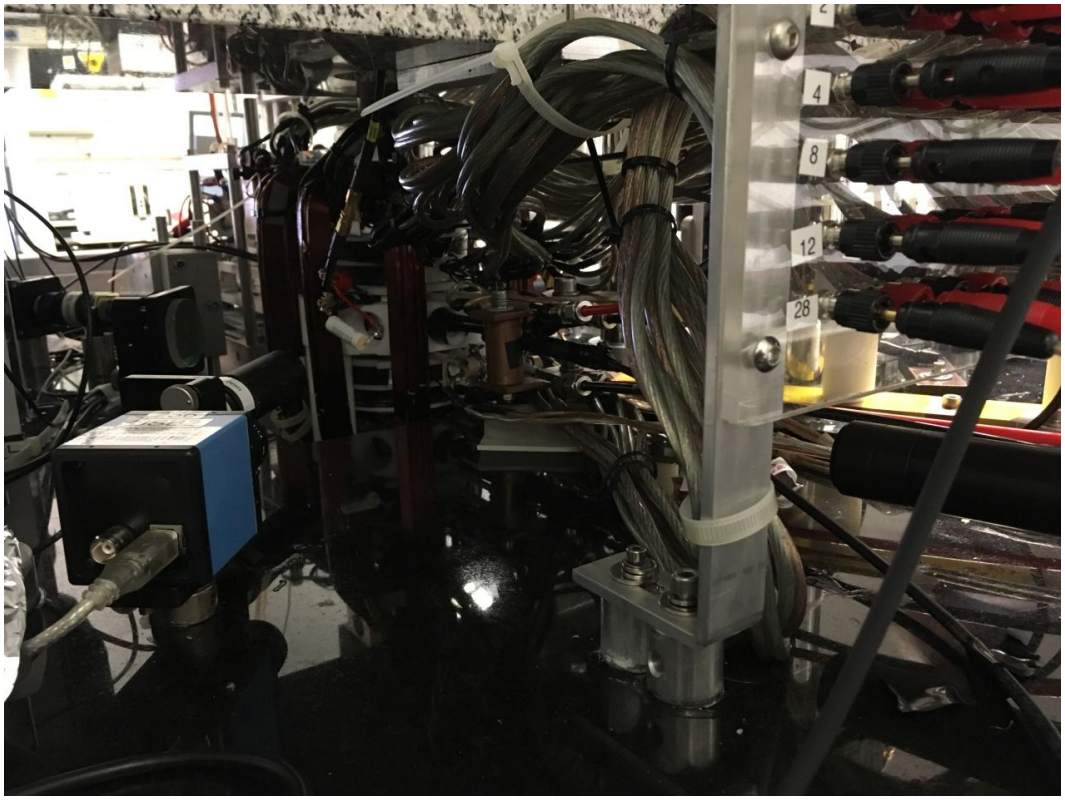

Figure 2.35 A back side photograph of the experimental device. All the extra optical elements should be putted between the existing.

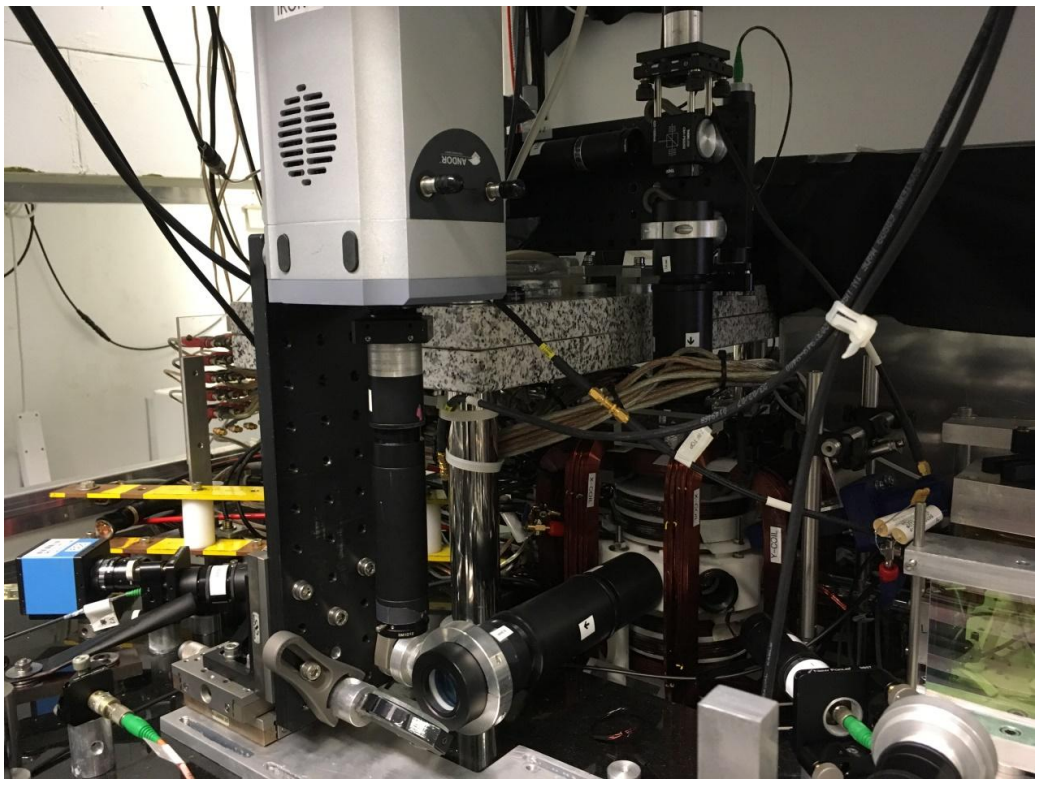

Figure 2.36. A front side photograph of the experimental device.

The initial idea was to design a setup that would use many of the existing optical elements without changing their position. We searched for possible places in the experimental device and we evaluated each one in order to reach the most effective and suitable place to put the extra parts of the optical setup. Finally, we decided the place that the new setup should be located at the red shadowed area in Figure 2.37 below.

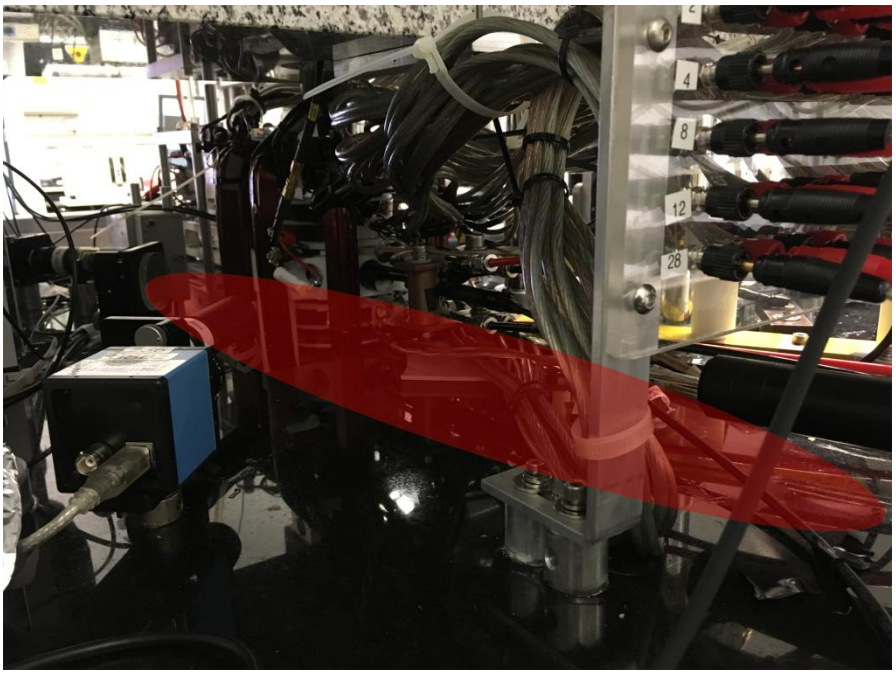

Figure 2.37. An edited photograph that shows the available for new optical elements space. In the optical design process we had to take care about the positions of the other optical elements

The length of the available place for the first part of the system (before the vacuum cell) is about 75cm. After the vacuum cell until the ccd camera we decided that the best-case scenario was to move as fewer parts as possible. This led us to decide that the detection part of the system should be mounted in the ccd camera without moving the existing imaging optical system. The available space for the detection part of the system is shown at the figure below. (red shadowed area at Fig Figure 2.38)

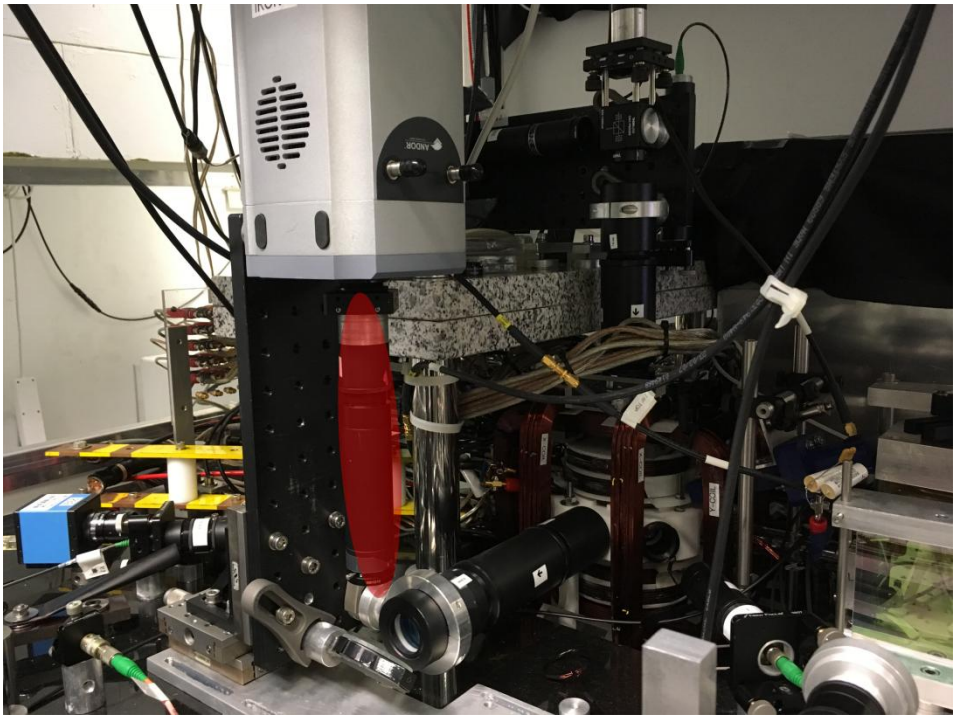

Figure 2.38. An edited photograph that shows the available space for the detection part of the new optical system. The idea was to replace the microscope objective in order to mount the detection part of the new setup.

Except of the restriction that we had in the positioning of the new parts the confined area that was available for the new setup induced several limitations in the optical design process. Some of these are the specific focal length of some lenses and the diameter of the used beam since this affects its waist.

2.2.3 Optical System design

After we defined the specifications of the new optical setup and have carefully considered the constraints the next step was to start the optical design process. At earliest steps we had measured the important distances at the experimental device, we made some calculations in order to have a good estimation for the parameters of the experiment and we started to simulate some parts of the system. At the optical design process firstly we design and simulate a draft optical setup composed by thin paraxial lenses. After some corrections and the optimization of the initial design the second step is to replace the paraxial optics with thick lenses in order to study the realistic system's

behavior taking into account optical aberrations. An iterative process of minimization of optical aberrations then leads to the optimization of the system performance.

The optical design process from the early steps until the final form of the optical setup is presented in this section. The optical setup was designed according to the requirements for the nondestructive imaging of the atomic cloud. We present an optical layout using raytracing analysis software Zemax. Finally, the characteristics and the performance of the new optical setup are described in detail.

Initial design

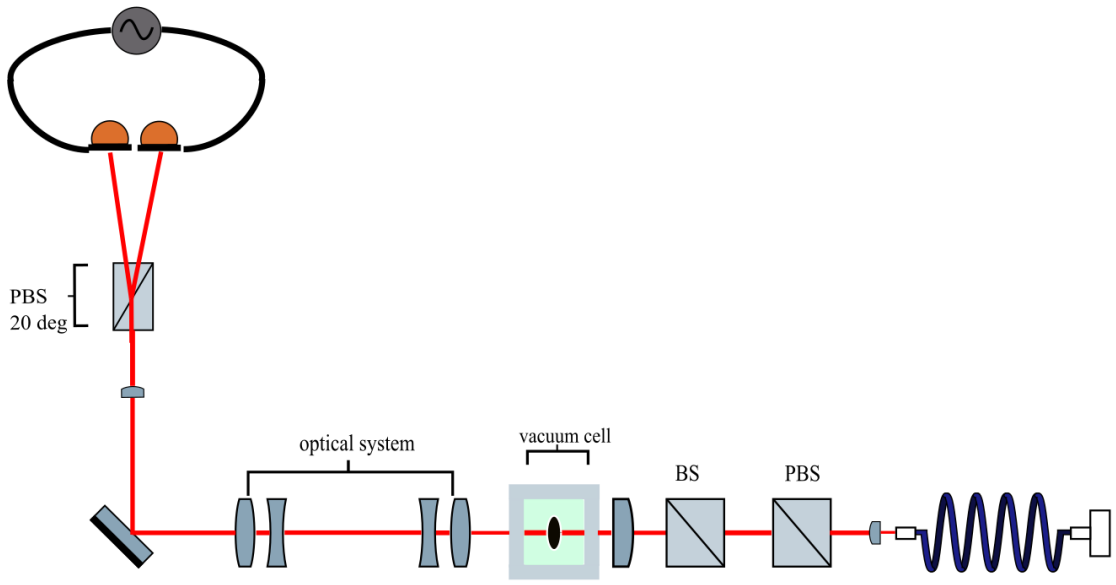

Figure 2.39. A schematic representation of the optical setup.

At this section the final design that we decided to construct is described in detail and an optical layout of this design with thin lenses is presented. As shown in Figure 2.39, the input source of the new system is a single mode polarization maintaining optical fiber of 0.12 NA. A fiber collimator is used to collimate the beam. Next a linear polarizer polarizes the beam at 45^{o}. The beam then goes through a non-polarizing beam-splitter, which sends a small part of the beam into a photodiode detector in order to monitor and record the power that goes

into the experiment. The polarized, collimated beam is then focused in the vacuum cell by a converging lens. We measured that the maximum free space for optics between the optical fiber and this lens is about 750mm. The waist of the beam in the vacuum cell should be at the position of the atomic cloud. That means that probably a mechanism that could translate the waist of the beam in all directions is necessary.. After the vacuum cell there is the optical system that is used, in other experiments of the Matter wave laboratory, for the atomic cloud imaging . We decided that this optical system will be a part of the new optical setup for several reasons. First of all its performance is satisfactory for the non-destructive atomic cloud imaging experiment. Another important reason is that this is the less invasive solution for the other experiments of the laboratory. Normally this optical system images the atomic cloud in a ccd camera. In our case that's not case since the beam will be collected on the balanced photodiodes. We added a short focal lens to make the beam approximately collimated (Rayleigh range much larger than the experimental distance) before the detection . The diameter of the beam should be several times smaller than the photoactive area of the photodetectors. A Wollaston polarization beam splitter splits the beam into two orthogonally polarized beams at propagating at a 20 degrees angle.

Simulation of the initial setup with thin lenses

Following the initial plan for the new optical setup the Zemax software is used in simulation and optimization of the setup. The simulation of a simplified setup is a very useful process since every optical element putted together and then the behavior of the total system is clear. In the beginning all the optical elements placed in correct sequence and arbitrary interspace distance. Next their relative positions are optimized in order to make a functional system. Optical design software, as Zemax, can support and contribute at the optical design process but the initial design and its characteristics are up to the designer. Zemax software gives us a lot of options that related with the input characteristics at the optical system. We choose a Gaussian beam with Numerical aperture 0.12 in order to simulate as better as possible the realistic conditions of

the experiment. We studied various combinations of optical elements until we reached a satisfactory scenario about the optical design. An optical layout of the setup using Zemax software before the optimization process is presented at the Figure 2.40.

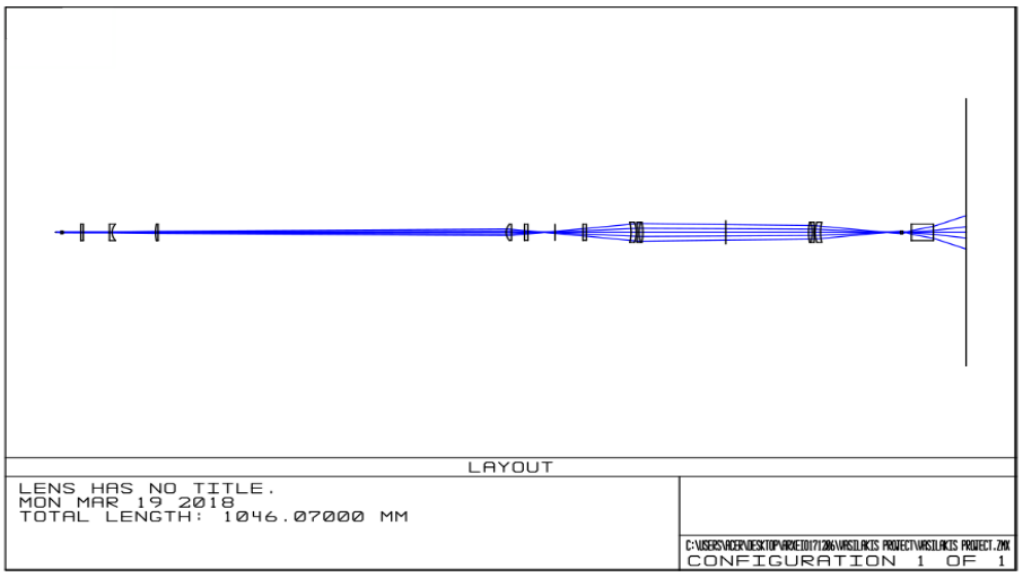

Figure 2.40. An optical layout of the optical system using Zemax software before the optimization process

Since at this stage, the interspacing of all the elements is arbitrary the optical setup is not yet functional. When all the optical elements have the desired characteristics the user optimizes the system in order to obtain the maximum performance possible. At the figure below a comparison of the optical setup before and after optimization process is presented.

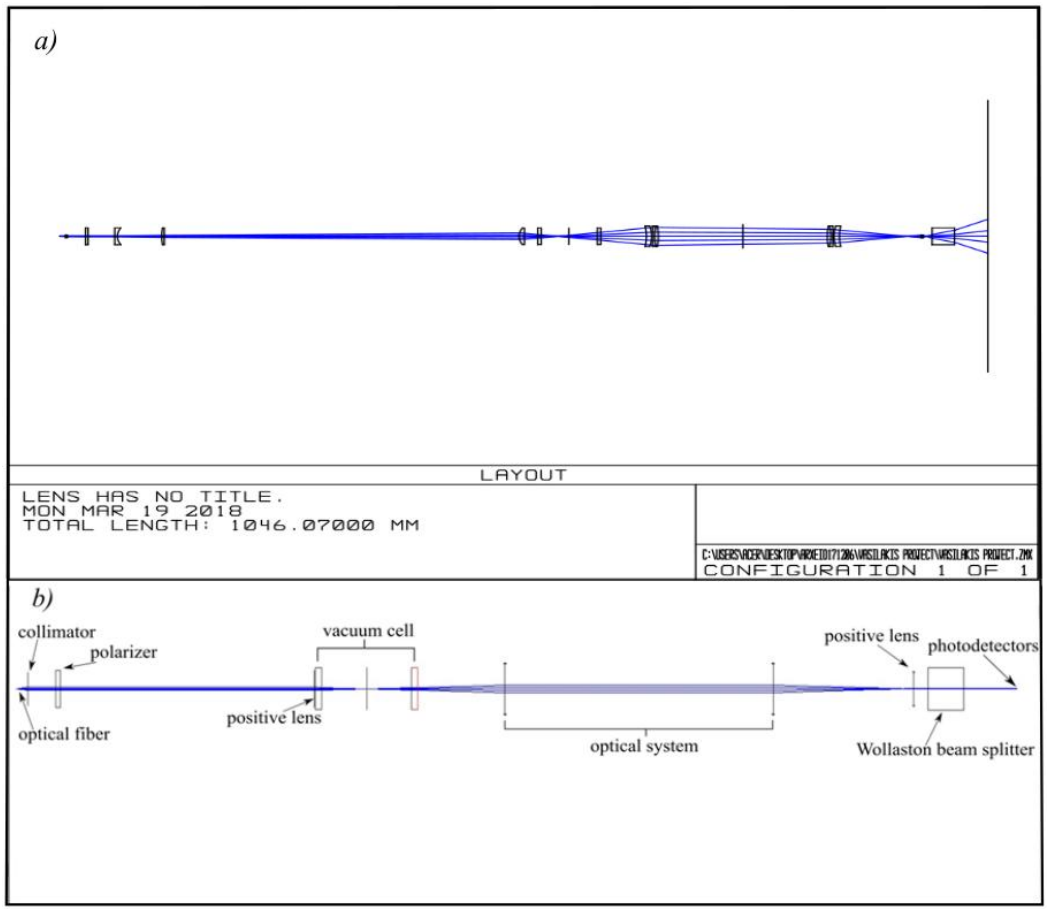

Figure 2.41. A comparison of the same optical setup before and after optimization process. The optical layouts are from Zemax software. a) An optical layout of the optical setup before the optimization process it is not functional. b) A more zoomed in optical layout of the setup after the optimization. There are labels that describe the optical elements.

Layout of the optical system

The initial optical setup using thin paraxial lenses now is ready. At this point we have a clear perspective on the specifications and the required system components. The focal lengths of the lens that we chose are accordingly the commercially available lenses. The next step was to replace the ideal paraxial thin optics with thick ones. The distances between the thick lenses are expected be a little bit different than the thin ones. Zemax software gives the choice to optimize the distances between the thick optics. After searching and testing possible lenses configurations (including combination of spherical lenses of

various focal lengths from 50mm to 75mm), we reached a combination that has the desired characteristics. The layout of the optimized optical setup is presented at the figure below (Figure 2.42)

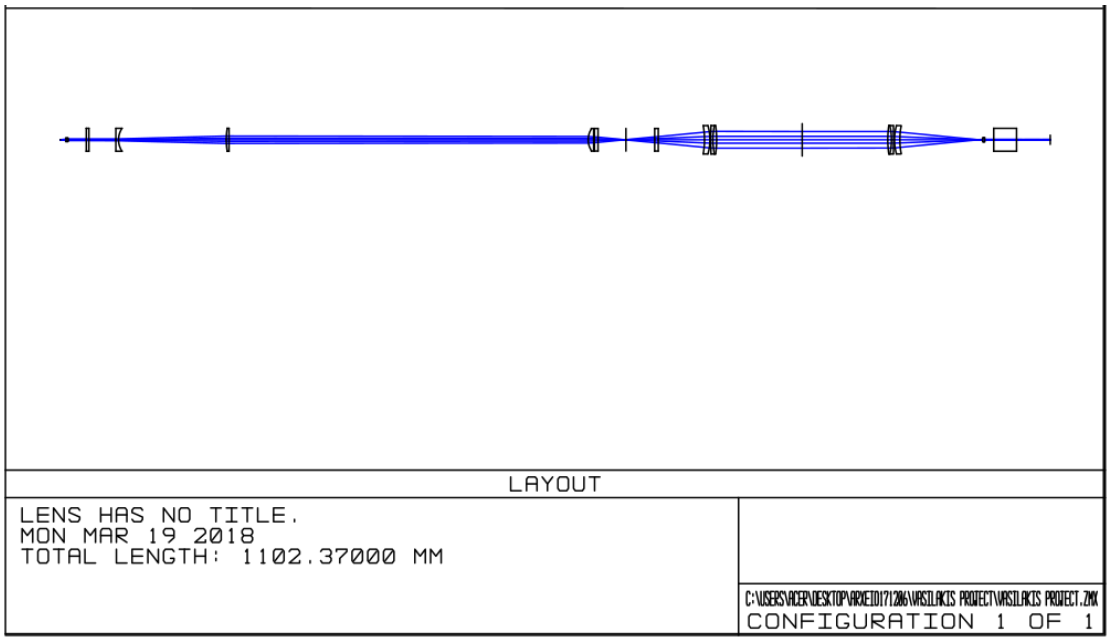

Figure 2.42. An optical layout of the final system with thick lenses after optimization process. All the optical elements are at specific positions and the distances between them are fixed.

The theoretical prediction for the beam waist in the vacuum cell is about 17-18μm. When imaging a thermal cloud this resolution is sufficient. An interaction of a Gaussian beam with a Bose-Einstein condensation demands smaller waist in order to reduce the noise of the measurement. On the other hand the existing imaging system after the vacuum cell sets the lower limit at the minimum waist that can be detected. Taking into account these two parameters, the ideal waist for this case is about 8μm. This led us to design an extra sub component for this optical system in order to reduce the waist of the beam in the vacuum cell. After theoretical calculations and simulations with the optical design software we added a 3x beam expander between the polarizer and the first converging lens(see Figure 2.43). This expander is a Galilean telescope that expands the collimated beam by a 3x factor and is comprised by a concave (-50mm) and a plano-convex lens (+150mm). The Galilean design for the telescope was preferred than a Kepler [24] one since the length of the first (~100mm) is

much smaller than the length of the second (~200mm). After the addition of the expander at the optical design, the waist according to the simulations is about 8μm. At the Figure 2.43 below the final design is presented.

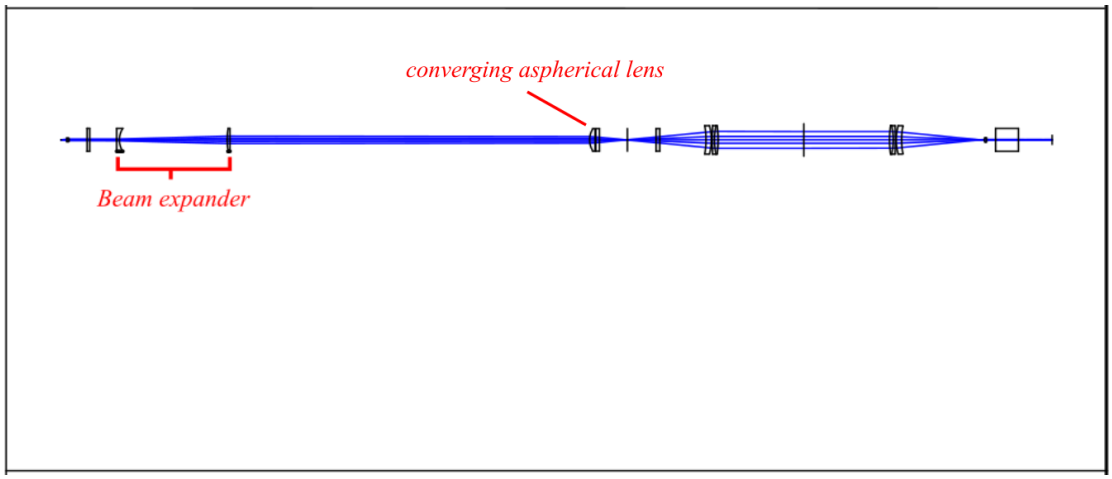

Figure 2.43. An optical layout by Zemax of the total optical setup. A beam expander was added to the optical system in order to change the waist of the beam in the vacuum cell.

Performance of the optical setup

As has been referred above Zemax software gives the capability for some diagnostic tests in order to evaluate the performance of the designed optical system. In any different case the user can find some useful diagnostics tests that evaluates the optical setup depending on the aim that the designer wants to achieve. During optical design the user can perform some of these tests in order to check if some actions, that were done, improve or not the performance of the optical system. At this section the performance of the designed optical system according to Zemax tests is presented.

Resolution

As it mentioned above, this optical setup doesn't aim to image the atomic cloud so the resolution at the output of the system was not the aim of the optical design process. The crucial point was to achieve specific values of the Gaussian

beam waist in the vacuum cell. Figure 2.44 shows the waist of the beam with and without the beam expander.

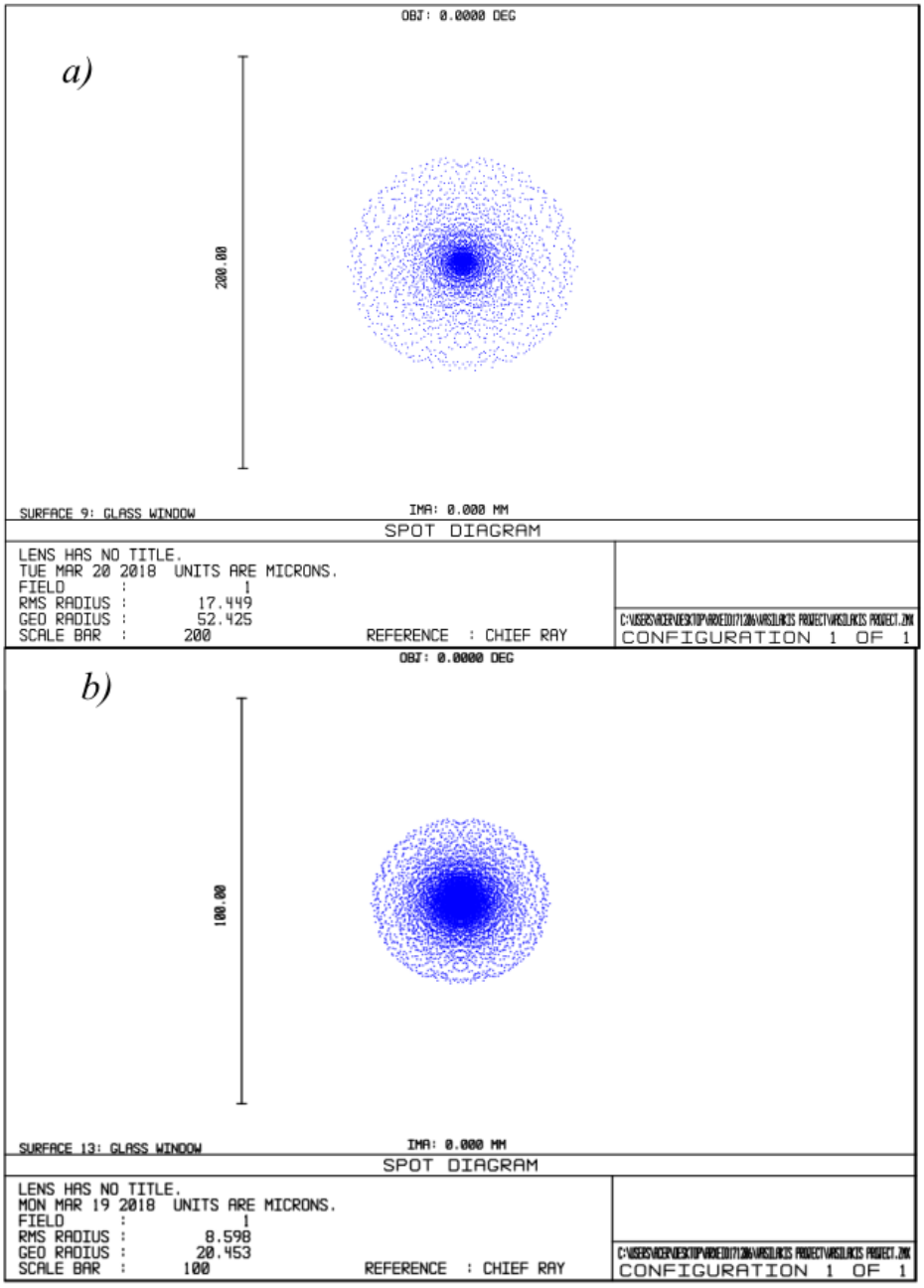

Figure 2.44. Spot size diagram of the passing beam in the vacuum cell. a) The waist of the beam in the vacuum cell without the beam expander is about 17.5μm. b) The waist in the vacuum cell with the beam expander is about 8.5μm.

The resolution in this part of the system seems to fulfil the initial aim for both cases. The waist that the simulations give is very close design specification.

Furthermore the numerical aperture of the beam at this point is less than 0.10 with the addition of the beam expander. The maximum numerical aperture of the imaging optical system is about 0.12 so vignetting effects are insignificant.

Another important specification parameter for this system is that the diameter of the collimated beam illuminating the photodetectors should be many times smaller than 4x4mm the photoactive area in order to avoid clipping effects The beam is collimated after the last positive lens and with Zemax diagnostics we can take information about its diameter on the photodetector plane (Figure 2.45).

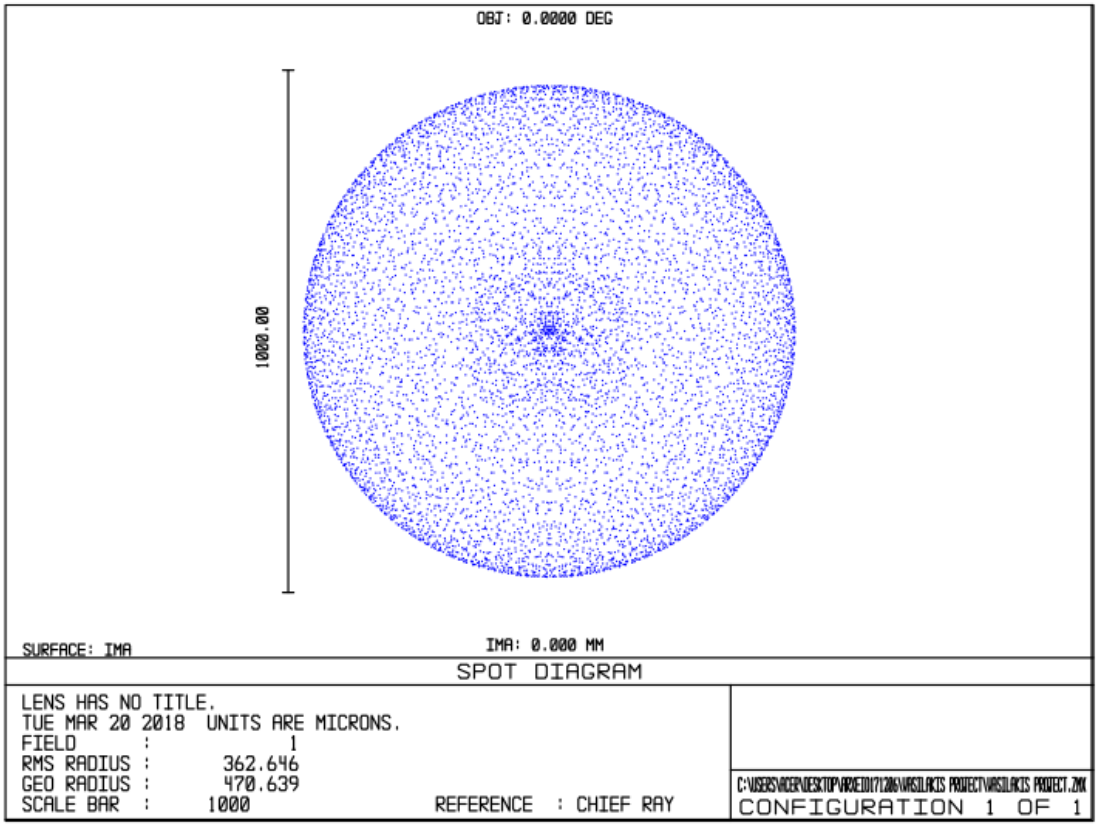

Figure 2.45. Spot size diagram of the beam at the photodetector plane. The diameter of the beam is about 700μm.

The diameter of the beam at the photodetector plane is expected to be about 700μm so it is much smaller than the photoactive area. After the last positive power lens the beam reaches a Wollaston beam splitter. This beam splitter splits the collimated beam in two components .The components remain

collimated and their diameters are the same as the beam before the Wollaston prism.

Illumination

Last but not least another important test is to simulate the behavior of the system if the input beam is tilted in respect to the optical axis of the system It is important to know about the vignetting effect since in this case small misalignments are common.

Another reason is that maybe it will be necessary to translate the beam focus in XYZ to match the position of the cloud. Zemax software simulated the optical system with different inputs (non-zero angle) in order to identify how the maximum acceptable misalignment. The results of this diagnostic test are presented at the

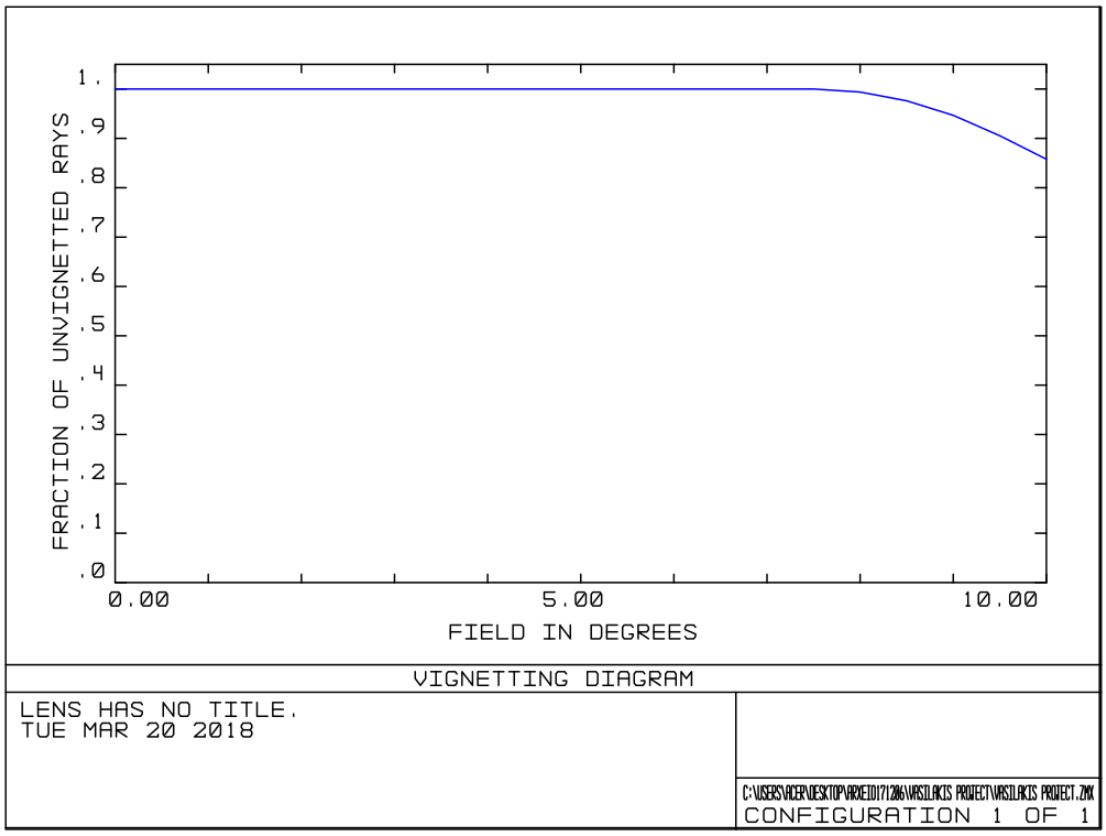

Figure 2.46.

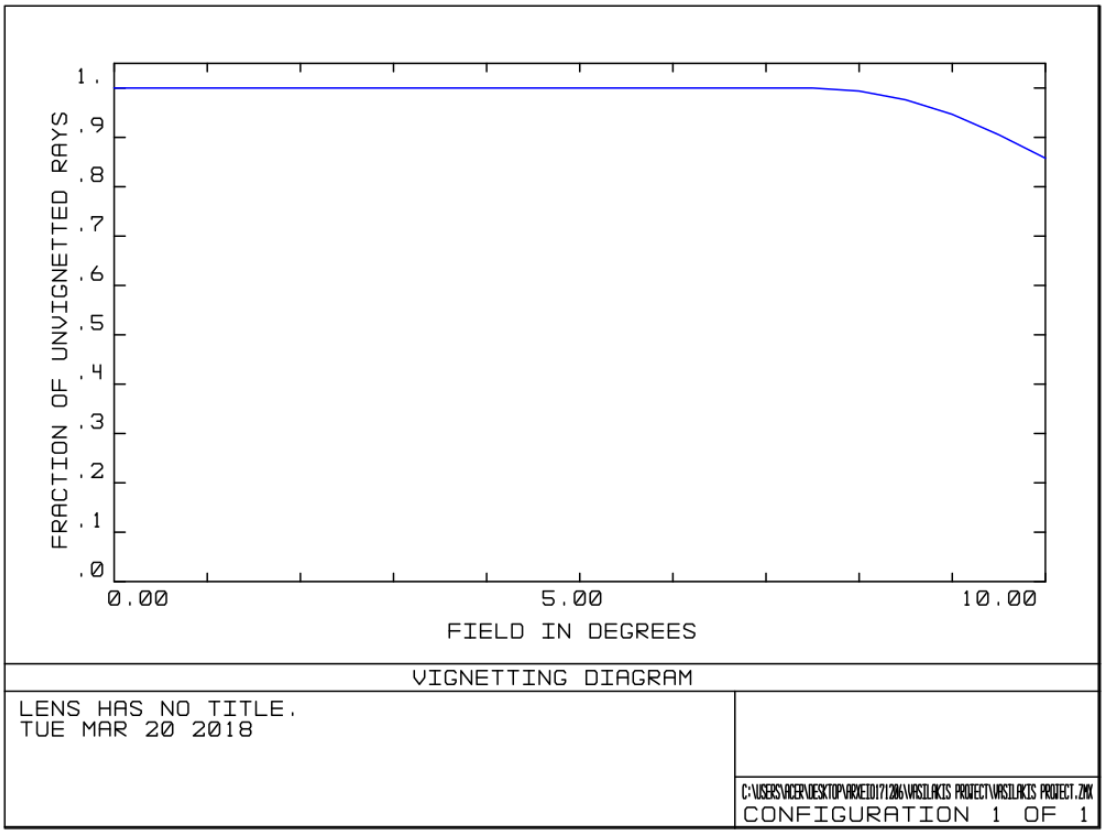

Figure 2.46. The vignetting diagram of the optical system from Zemax software. As it can be shown until 7 degrees field there is no vignetting effect. At 10 degrees the unvignetted rays are the 80%.

The upper limit in the input field is 7 degrees. Below this value there is not vignetting effect or clipping of the Gaussian probe beam. If it is necessary, the beam will be adjusted with a mirror mount

2.2.4 Implementation

When the theoretical design for the optical setup was ready and its performance tested with Zemax diagnostics we started to take care about the mechanical design in order to support the optical setup. The implementation part is separated in two parts. The first is the part of the setup that it is responsible to direct the beam in the vacuum cell and determines the strength of the interaction between the atomic cloud and the beam. The second part of the system is responsible for the detection of the beam after the interaction with the atomic cloud.

Opto-mechanical design

The opto-mechanical setup is separated in two parts. In the beginning we design all the parts using the Autodesk Inventor software. Some parts are custom designed and some others are commercially available. Firstly the mechanical design of the first part that is positioned before vacuum cell is presented. Next we present the detection part of the setup that is positioned after the vacuum cell.

First part of the opto-mechanical setup

As already mentioned a polarization maintaining optical fiber is the input of the setup. Next to the fiber we used a fiber coupler in order to collimate the beam. This fiber coupler consists of an 8mm focal length lens .The diameter of the collimated beam after the coupler is ~1.44mm. The next item is a polarizing beam splitter.

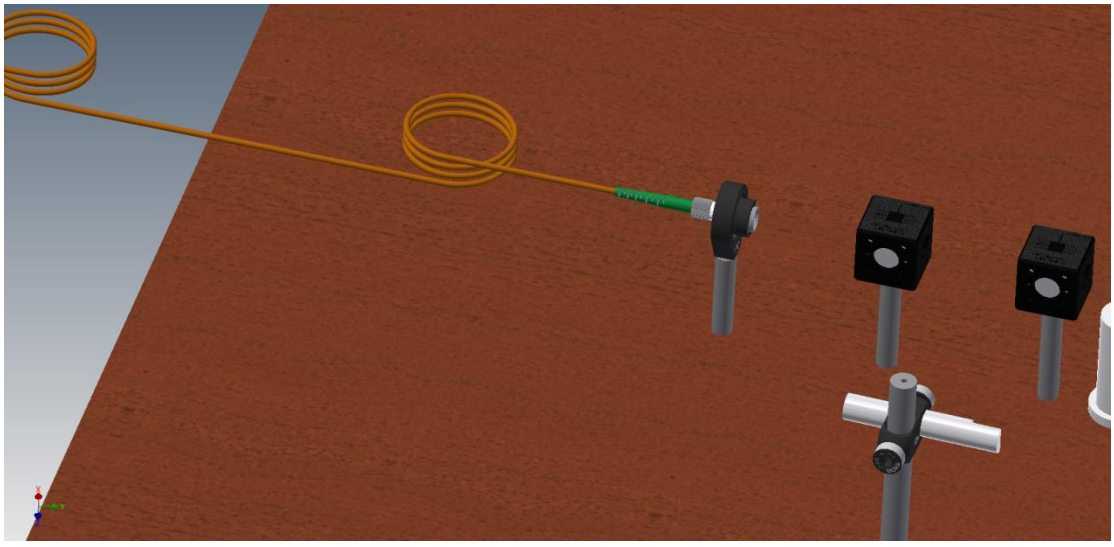

Figure 2.47. Opto-mechanical drawing of the first part of the optical setup. The second beam splitter is used on order to measure with the photodetector the incoming to experiment intensity.

For all these items that were mentioned above we designed aluminum posts for their mounting. These different sized posts guarantee that the height

from the optical table is the same for all the optical elements. The next item is the custom designed beam expander. For the housing of the negative and positive power lenses we used a commercially available lens tube. The expander can easily be removed from the setup. After the beam passes from the beam expander two mirrors mounted in mirror mounts is used to direct the beam in the vacuum cell. Before the vacuum cell and after the second mirror there is an aspherical positive power lens. The housing of these lenses should be something that is easily removable since when the other Matter wave laboratory experiments are activated the space before the vacuum cell must be empty. The other constrain was that in macor's holes there are threads and the clear aperture is about 26mm when the diameter of the lens is 25mm. Finally it is crucial for the experimental process to adjust the distance between the lens and the vacuum cell since the position of the atomic cloud is not stable and known beforehand. Finally we reached a design that enables the user to adjust the distance between the lens and the glass window of the cell. (Figure 2.48)

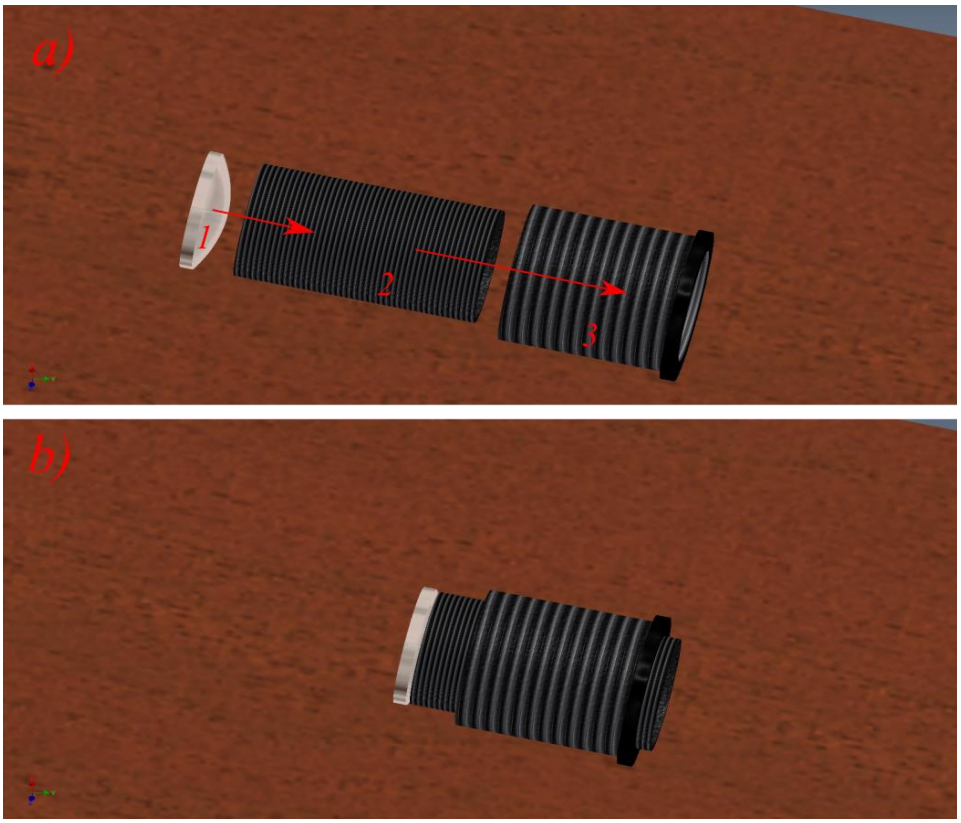

Figure 2.48. The opto-mechanical design of the aspherical lens housing. a) The aspherical lens (1) ,the housing of the lens(2) and the macor adaptor(3) are presented. The red arrows show the way that the part connected between them. b) Total assembly for the aspherical lens housing. The way that the parts fit together is shown.

As it can be shown, an aspheric lens is mounted in an external threaded mount. This mount is constructed by ertacetal plastic in order to avoid eddy currents. There is another mount with internal threads. The last is the adaptor to the macor and can be screwed in this. With this way a relative motion between the two plastic mount is possible. Furthermore, when the aspheric lens is not necessary the assembly that is shown at Figure 2.48 can be easily removed. At Figure 2.49 the way that the aspherical lens mounted in macor is presented.

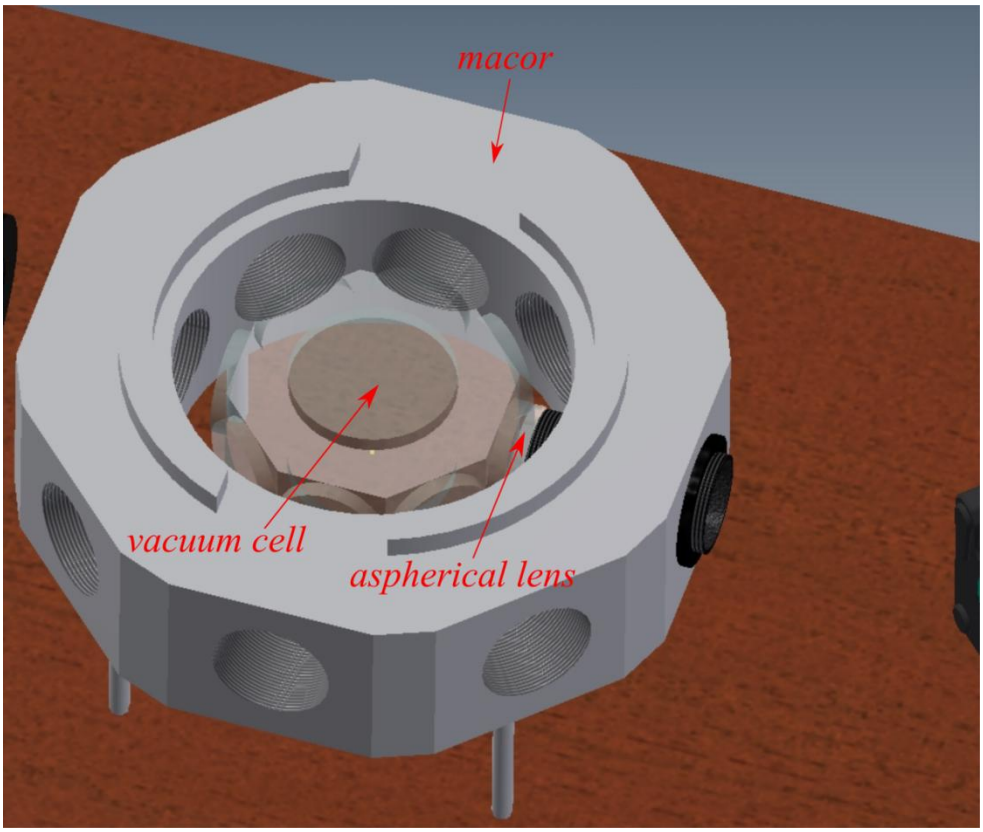

Figure 2.49. Optomechanical design of the aspherical lens mounting. This drawing shows the way that aspherical lens be mounted next to vacuum cell.

Next to the vacuum cell there is the atomic cloud imaging system that is used and for the other experiments in the lab. After the beam leaves the imaging system reaches the detection part of the system. At the section below there is an analytical description of the detection part opto-mechanical design.

Detection part of the opto-mechanical setup

The imaging system focuses the beam on its image plane. Another lens which focal length is about 4.8mm is placed next, in a way that the beam is collimated after and its diameter is about 0.5mm. We designed a custom adaptor for this lens in order to housing it. After the beam collimator lens there is a Wollaston beam splitter that splits the bean in two components. The relative angle between these two components is 20 degrees. We measured the distance between the two photodetectors and we calculated the distance between the Wollaston beam splitter and the photodetectors. The aim was for each beam component to reach the center of each photodetector. The way that the photodetectors are connected between them is shown at the Figure 2.50.

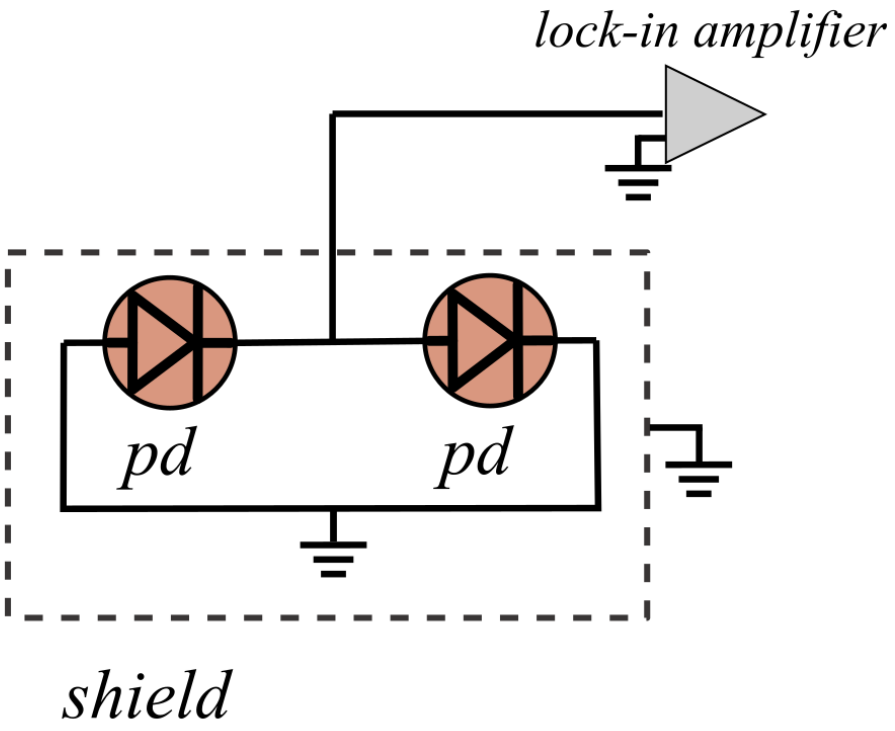

Figure 2.50. Photodetectors electrical connection aimed at subtracting the photocurrents.

Some other parts were designed and manufactured from F.O.R.T.H's workshop. All these parts are necessary since are spacers, adaptors, mounts and

electric isolators. At the figure below (Figure 2.51) the total assembly of the detection part setup is presented.

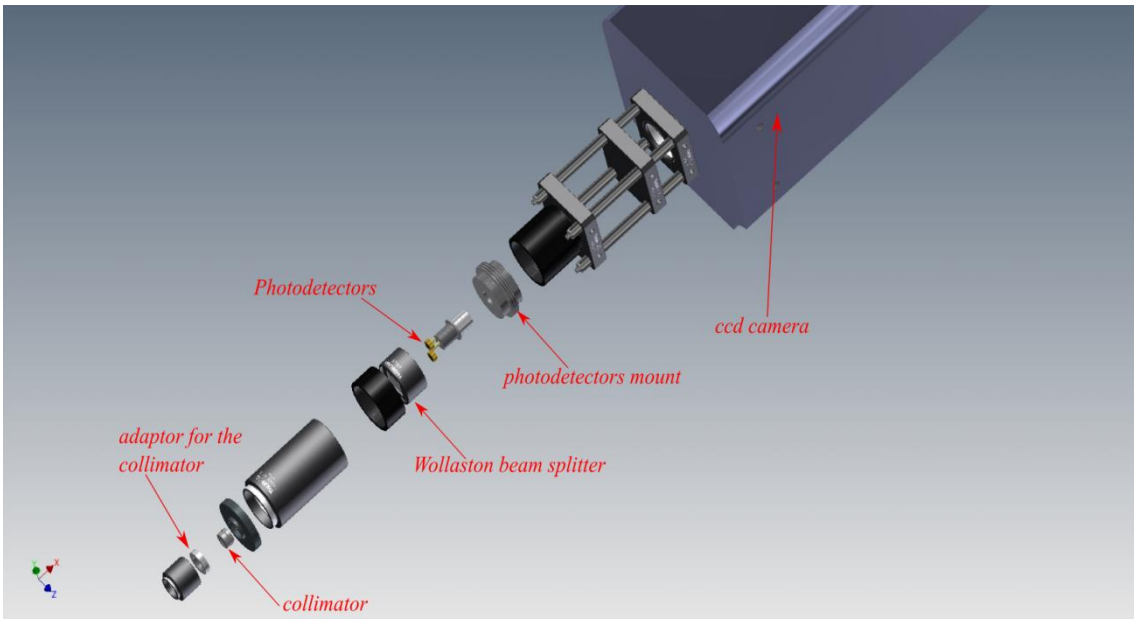

Figure 2.51. Opto-mechanical design of the detection part. This drawing shows the way that the parts fit together. The labels notice the most important parts of the detection part assembly.

All the optical and mechanical items are identified with red labels. Commercially available parts combined with custom designed in order to reach a mechanical structure that meets the constraints and achieve the desired performance. A cage system comprised by four parallel rods, attached to the ccd camera, offer the capability to adjust the distance between the waist of the Gaussian beam at the image plane of imaging system and the detection part's first lens (collimator). The length of these rods is fixed and ensure that the beam will be collimated after the lens collimator (Figure 2.51) as the optical design predicts. A figure of the final form of the detection part opto-mechanical design presented at the figure below (Figure 2.52).

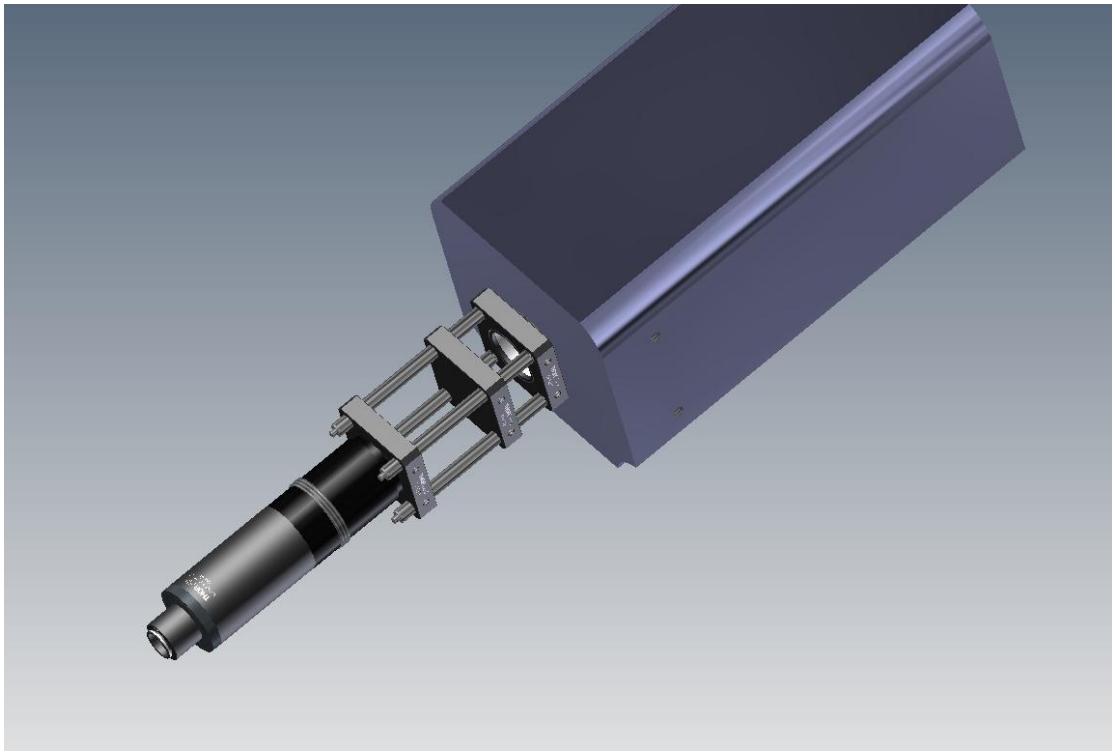

Figure 2.52. An opto-mechanical drawing of the detection part.

Optomechanical system assembly

At this section the total opto-mechanical assembly presented at the Figure 2.53 below with labels for all the important components.

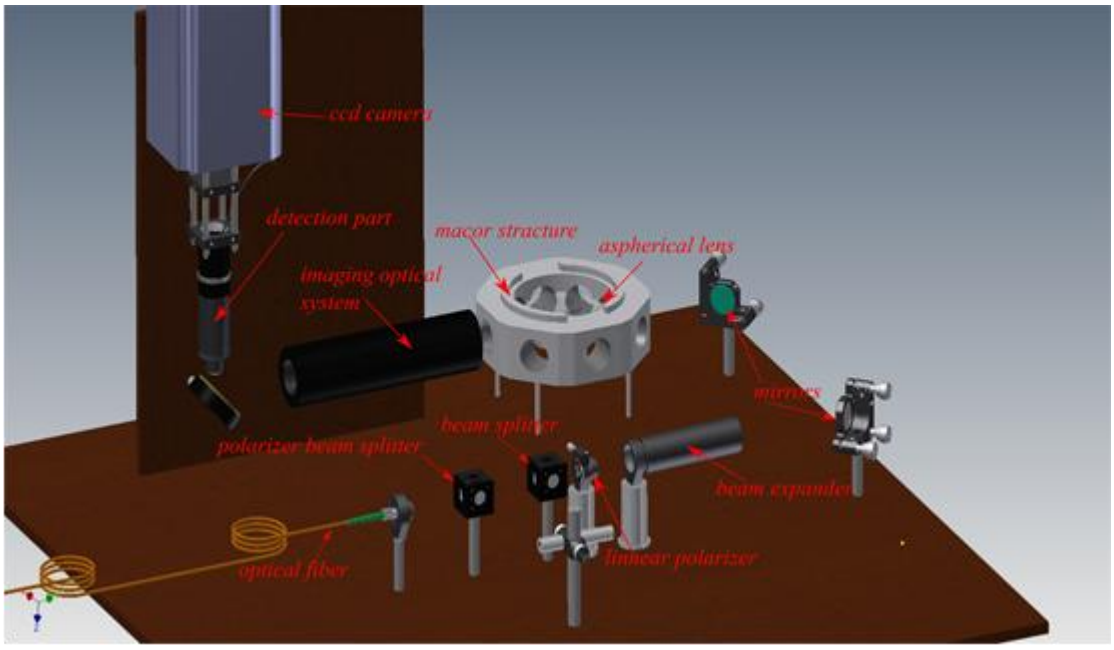

Figure 2.53. . Complete opto-mechanical setup. All the important items that the setup consists of are noticed with labels.

2.2.5 Optical System's performance

In this section the way that the opto-mechanical setup implemented is described and its performance presented. When the theoretical design was ready, we collected all the items and parts that were necessary in order to implement the setup. The implementation setup was performed in two steps: First we implemented the part of the optical system before the vacuum cell and after we continued with the implementation of the detection part. Before we integrate the setup in the experimental device we had to be sure that everything works properly. Some tests were made in order to test the performance of the optical setup in an optical table.

First part implementation –performance

We started with checking if the experimental value for the beam waist in the vacuum cell agreed with the theoretical prediction. For the input beam it was necessary to know the achieved spot size (waist of the beam) at the aspherical lens focus in the vacuum cell in order to create a cold atomic cloud with comparable size. Due to space limitations in the experimental device, the distance between the optical fiber and collimator from the aspherical lens was not known beforehand. In order to check how the distance between the optical elements affected the waist of the beam after the aspheric lens we constructed the simple setup that is shown at the Figure 2.54. We used a collimator that creates as an output a Gaussian beam which diameter(two times the waist) is about 1.5mm, a commercially available mount for the collimator, the aspherical lens after a few centimeters and a beam profiler (Ophir Photonics NS2- Ge/9/5) in order to detect the beam waist.

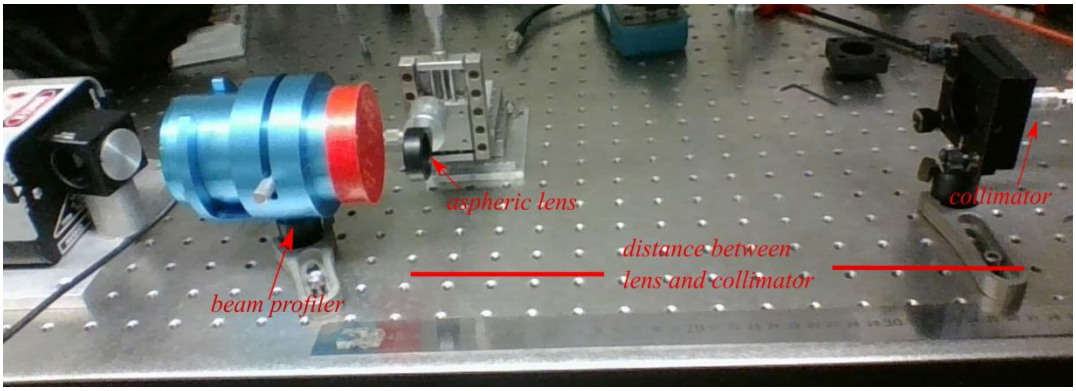

Figure 2.54. The used setup for the measuring the waist of the beam after the aspherical lens. We changed the distance between the lens and the collimator and we measured with the beam profiler the waist of the beam.

We adjust the distance between the fiber collimator and the aspherical lens from 12 cm up to 40cm and we measured the waist with the beam profiler. The waist is practically stable as a function distance as it can be shown in Table 6. These results are very close to theoretical prediction. Actually at the experimental results the diameter is a little bit smaller but that is something expected since in our numerical simulations the glass window was included which is not present in this test. Spherical aberration, induced by this window, can increase the waist of the Gaussian beam.

Distance between lens and collimator(cm)	**Beam diameter ($1/e^2$)(μm)**
12±1	30±1
17±1	29±1
27±1	29±1
30±1	29±1
40±1	29±1

Table 6. The measured beam waist as the distance between the optics changes

Beam size close to the beam waist

Another thing that we had to measure was the diameter of the beam close to the waist for both sides. That was important since it was necessary to have estimation on how the relative distance between the focus of the lens and the atomic cloud should be controlled in order to achieve maximize interaction of the probe the atomic cloud. The idea is that if we want to measure a bigger atomic cloud we will defocus the aspheric lens . This means that the waist of the beam is some millimeters displaced relative to the cold atomic cloud position. That could be done since we are not interested about the phase distribution of the interacting beam. The setup is presented at the Figure 2.55. Firstly we placed the beam profiler at the waist of the beam and after that we were moving at the longitudinal direction the lens with the translation stage. The step was 1mm each time. The beam profiler was at the same position so with this way we were measuring the beam diameter both sides close to the waist. In this measurement we added a 3mm glass (B-K7) in order to simulate as better as possible the conditions of the real experiment.

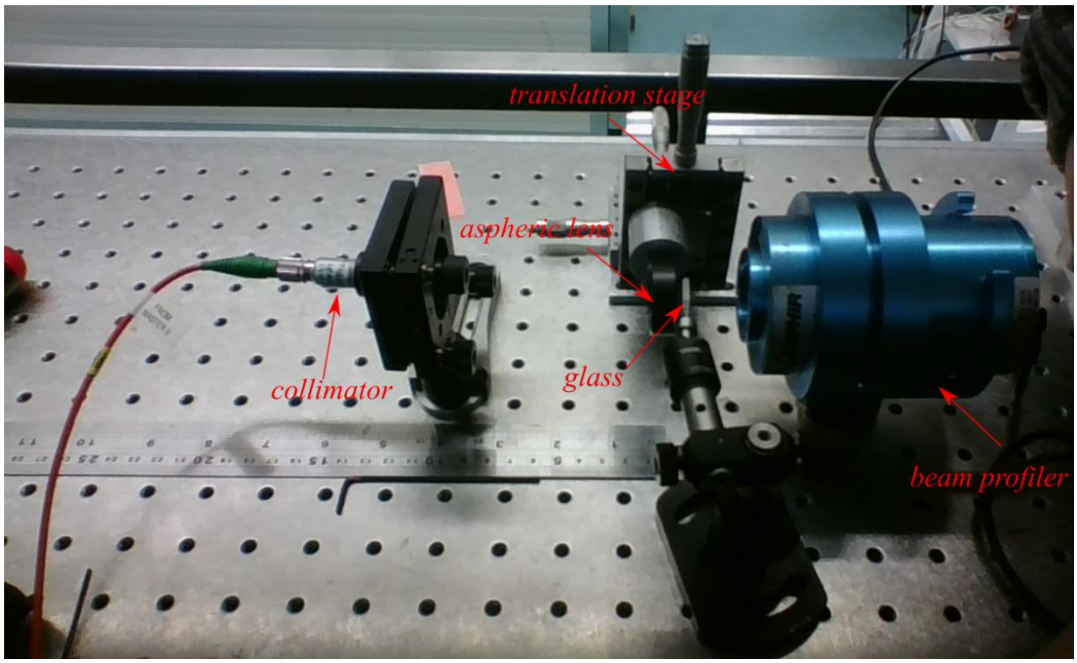

Figure 2.55. The used setup for the measuring the beam diameter close the waist. The beam profiler was putted at the waist of the beam and we moved the lens, left and right at the transverse direction. For each movement we were measuring the beam diameter (two times the beam waist) with beam profiler.

The results of these measurements are presented at the Plot 1 below. The error in the distance from the beam waist is 50μm since that determined by the translation stage that we used in order to move the lens. The beam size estimation error was ~2 μm. The size of the beam is referred at to the waist of the beam in which the power is of the maximum.

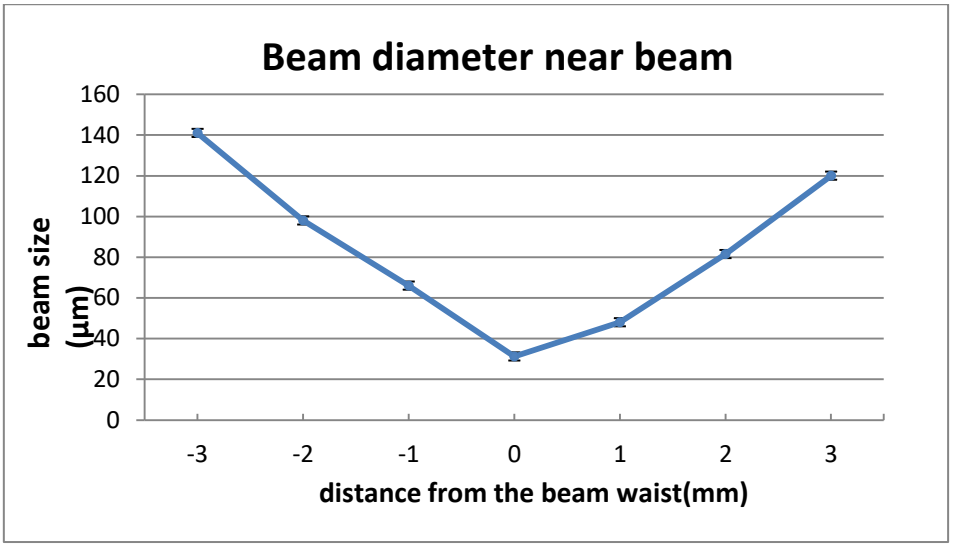

Plot .2. Beam size ($1/e^2$) as a function of the distance from the beam waist.

Total optical setup measurements

The next step was to implement all the optical setup at the optical table in order to take measurements for the system with as closer as possible realistic conditions. Firstly we glued, using a UV curing glue, the aspheric lens in the special ertacetal mount. After that we aligned the mount with a translation stage relatively with the lens and when the proper position was found we cured the glue with a UV lamp for 5 minutes. (Figure 2.56)

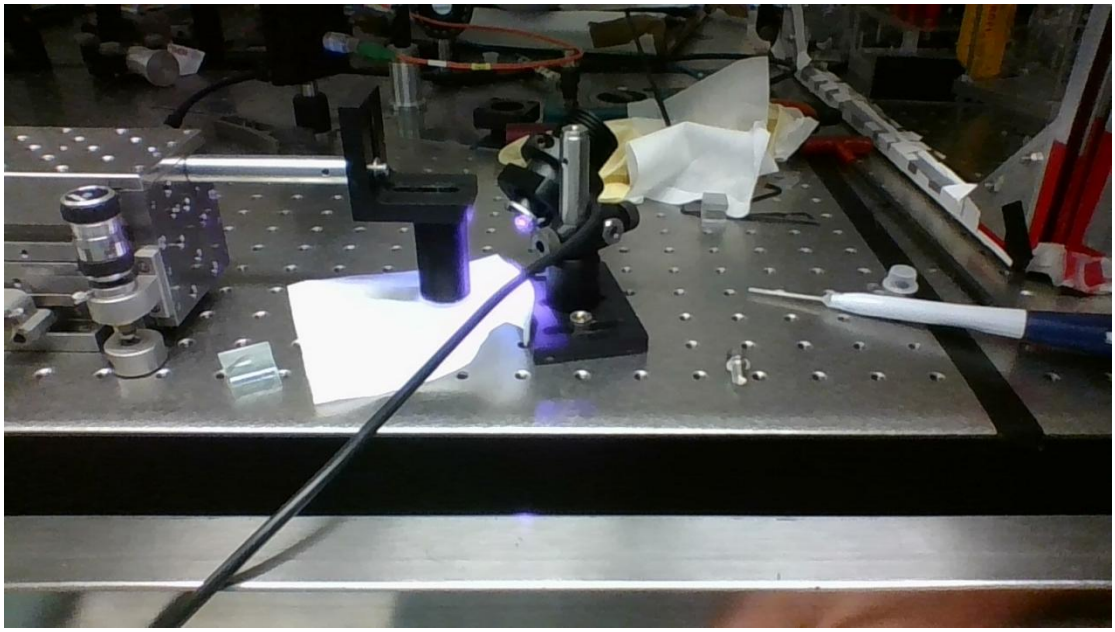

Figure 2.56. Glue curing process.

After the successful gluing of the aspherical lens we implemented the total optical system at the optical table. We aligned all the optical elements in order to achieve the theoretical prediction for the performance of the optical setup. We implemented the setup with and without the 3x beam expander as it can be shown at the figures below (Figure 2.57 & Figure 2.58). Firstly is presented a top view photograph of the optical setup without the beam expander.

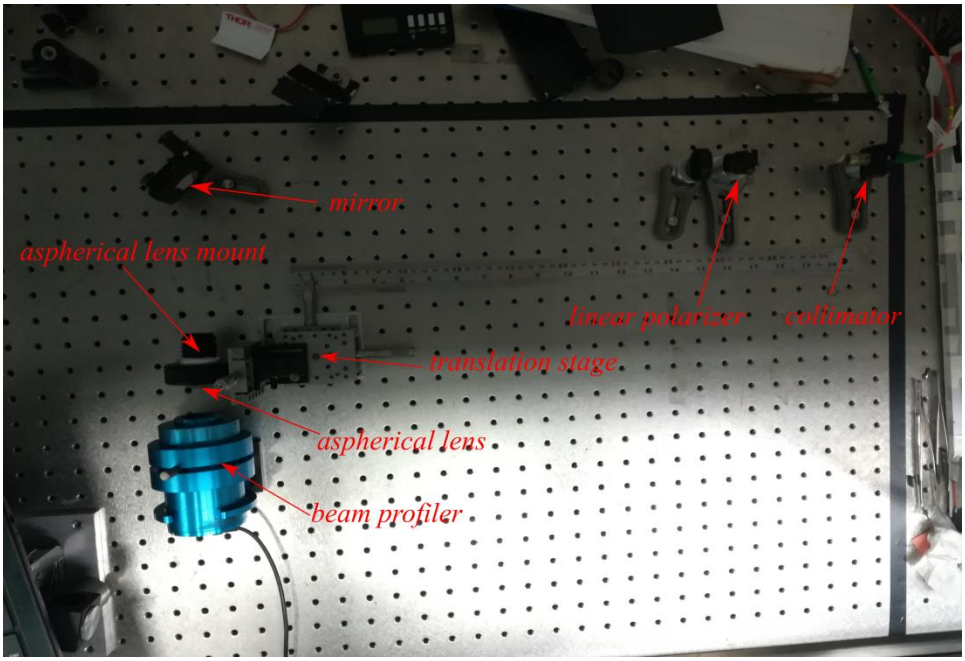

Figure 2.57. Photograph of the total optical setup without beam expander. All the used items are noticed with red labels.

Following we present a photograph of the setup with the beam expander. The beam expander is constructed with such a way that easily can be inserted in the optical setup. All the other items remain the same.

Figure 2.58. Photograph of the total optical setup with the 3x beam expander.

The beam expander is placed at the focal plane of the aspherical lens in order to experimentally measure the beam waist for both cases (with and without the beam expander). We moved slightly with the translation stage the lens along the beam propagation axis until the beam profiler measured the beam waist (minimum measured beam size). We repeated the measurement after the addition of the beam expander.

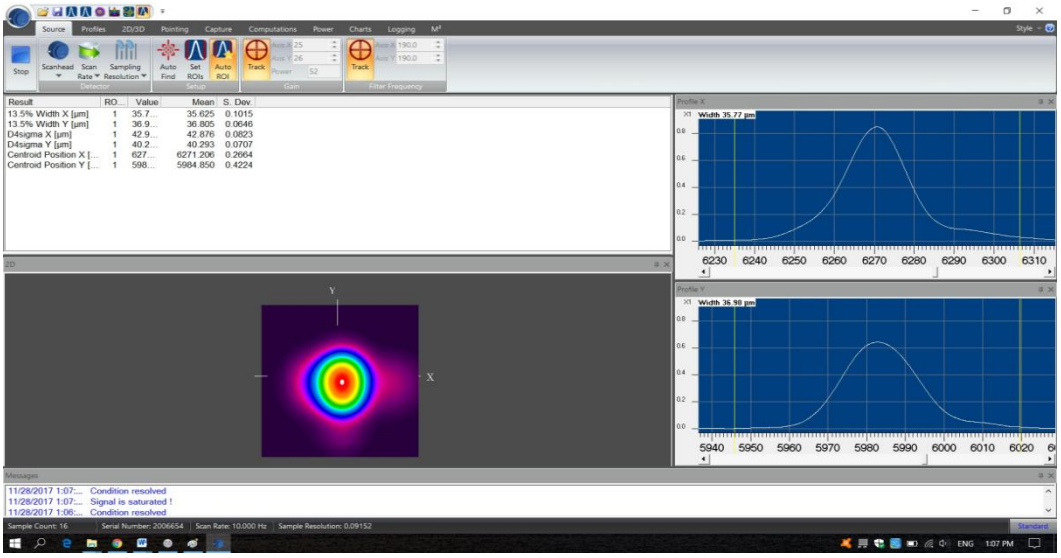

Figure 2.59. A figure of the beam profiler measurement without beam expander. The waist of the beam is about 17.5μm

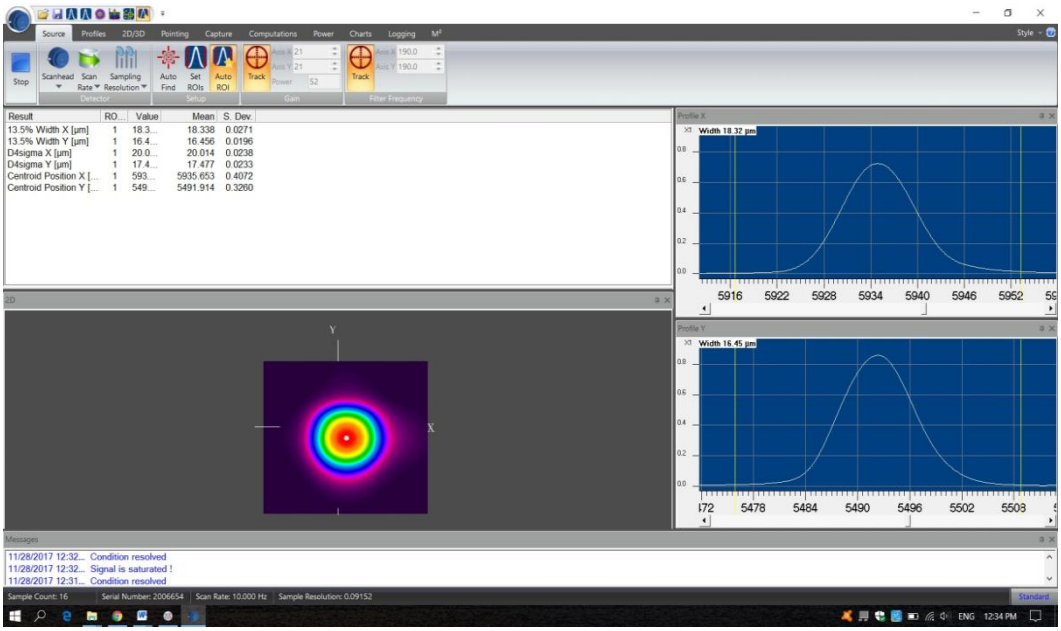

Figure 2.60. A figure of the beam profiler measurement with the beam expander. The waist of the beam is about 9 μm.

As it is obvious from the beam profiler measurements, after the addition of the beam expander the waist drops about 2.5 times. Furthermore the results show great agreement with the theoretical prediction.

Detection part performance-implementation

The next step was to implement the detection part of the setup. We tested that all the custom made parts fit with the commercially available and we started to build the setup. The most important test that we had to do in order to ensure the proper functioning of the detection part, related to the capability of the setup to detect the signal after the interaction between the cold atomic cloud and the probe beam.

At the beginning we tried to align the axis that the Wollaston splits the beam with the photodiodes. After that we placed all the elements on an optical table. We used a polarization maintaining optical fiber, a collimator which make the beam diameter about 0.5mm (the same diameter as that we have in the experiment), an adaptor for the collimator, a mount for the optical system and a voltmeter (Figure 2.61).

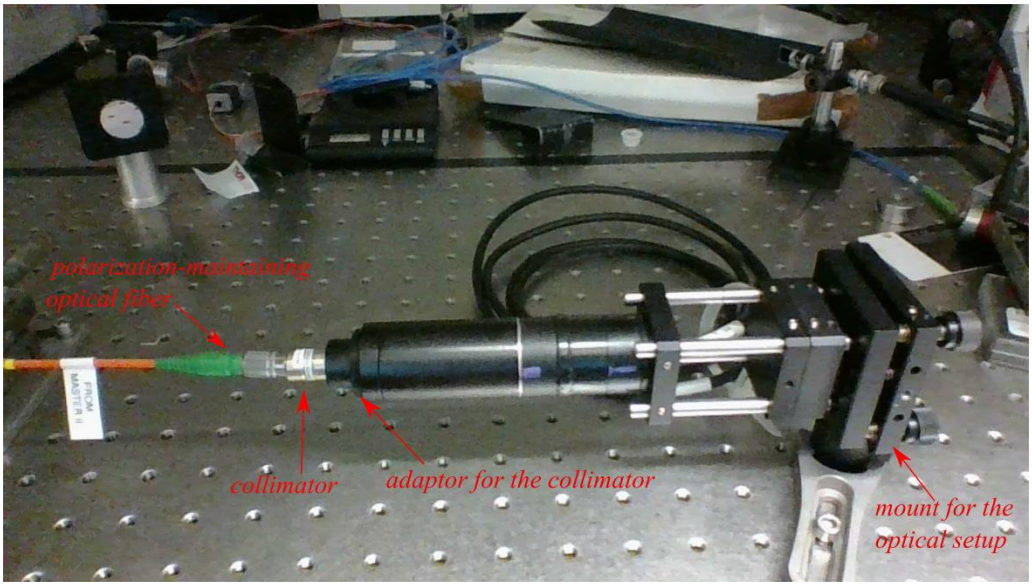

Figure 2.61. A photograph of the test that we made in order to align the Wollaston prism with the photodiodes and check if the optical setup is able to detect the signal.

The lens tubes and the cage mounts ensure that the probe beam, the Wollaston and the photodiodes are collinear. However the challenge was to align

the axis that the Wollaston prism splits the beam with the photodiodes axis of symmetry as can be seen in Figure 2.62.

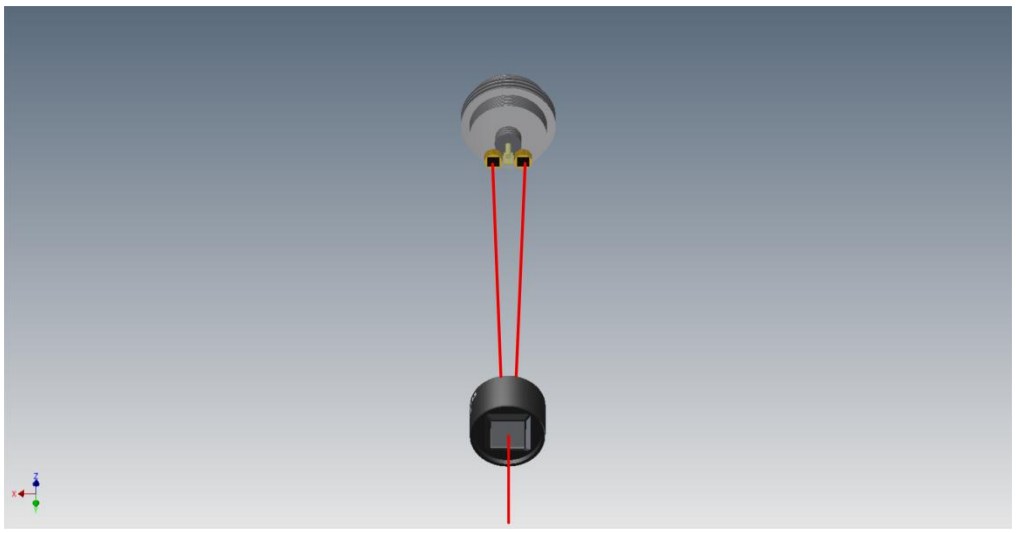

Figure 2.62. A drawing that shows the way that the Wollaston prism splits the inserted beam in 20 degrees angle. The aim was to direct each separated beam in the corresponding photodiode.

As it is referred above the polarization maintaining optical fiber delivers light linear polarized parallel to it's axis. The Wollaston prism separates the incident beam into two orthogonally polarized outputs. So when the polarization of the probe beam is aligned to one of the two Wollaston polarization axes only one photodiode receives signal. The photodiodes are electrically connected with such a way in which every time the measured signal is equal difference of the two photodiode signals. So in the case that all the light reaches only to one photodiode we expected the maximum measured value in the power meter. Ideally when the axis of the fiber is aligned with the one or the other photodiode the signal's absolute value should be the same. The only thing that changes is the sign before the measured value.

A simple way to test that is to mount the collimator in an adaptor which is external threaded. After that, this assembly can be screwed and unscrewed in the same tube that the Wollaston prism and photodiodes are mounted. As the optical fiber rotates light polarization rotates too.

In the setup the photodiodes are held in a fixed position, whereas the Wollaston can be rotated. The position of the beam at the photodiodes depends on the angle of the Wollaston prism. A correctly aligned Wollaston prism results in two orientations of the fiber sending all the incoming power to one or another photodiode. In order to align the Wollaston prism, we seek to find a position of the prism which, when rotating 180 degrees the fiber we get two approximately equal and opposite, maximum (absolute value) readings in the voltmeter, with the maximum value corresponding to the power of the incoming beam. A photograph of the experiment presented below. (Figure 2.63)

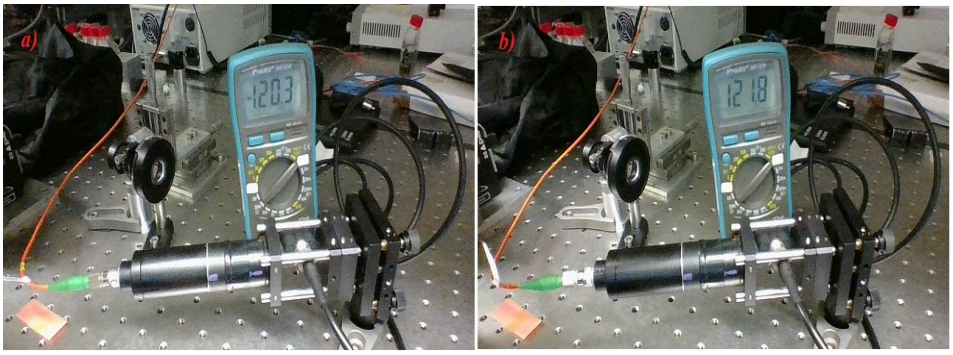

Figure 2.63. Photograph of the tests results. The signal at the two photodiodes is almost the same. Each photodiode detected all the light when the polarization of the light after the fiber is aligned with one of the axis that Wollaston splits the beam. The measured signal was 120.3 nAmps and 121.8 nAmps respectively.

The signal at the two photodiodes was 120.3 nAmps and 121.8nAmps respectively. The difference in measured signal (1.2%) was not due to misalignments. Finally after we found the right relative position between the Wollaston and the photodiodes we removed the lens tube and we aligned the optical fiber with one of the Wollaston axis. This means that in this axis the signal was maximum and in the other axis the signal was zero. Then we measured the passing beam first with the one photodiode and after with the other. The result was the same, there was an about 1.2% difference between the measured values .So the two photodiodes measure the same beam with a small difference at least in this range of power.

Discussion

All the tests showed that the system is ready to be inserted in the experimental device. Its resolution performance in the vacuum cell is satisfying since the achieved waist could be adjusted with the addition of a beam expander. From the other side the Wollaston beam splitter is aligned with the photodetectors and we are sure that each beam component reaches the corresponding photodetector. All these tests and the implementation of the parts were carried out in an optical table.As a future work we will further develop this system in order to be able to translate the beam waist in the vacuum cell in the longitudinal direction without sacrificing resolution. Another future plan is to insert the optical system that we describe in Section 2.1 in the experimental device. This will upgrade the resolution, the illumination and the detection ability not only for non-destructive cold atoms imaging experiment but also for absorption imaging and fluorescence imaging.

3 Conclusions

We studied ways in which optical systems for ultra-cold atoms experiments can be designed and implemented. A detailed theoretical study was conducted on how to mitigate spherical aberrations introduced by the glass window of the vacuum cell in ultra-cold atom experiments. We introduced a new strategy in optical design that pertains to how positive spherical aberrations in an optical system can be balanced by the use of a flat plate. We derived an analytic formula for the optimal thickness of the glass plate that balances the spherical aberrations of an optical system. We also discussed the limitations of this technique and the cases it may be useful in the optical design process.

Furthermore, we designed and implemented a diffraction-limited optical system that is intended for use in absorption and fluorescence imaging in ultra-cold atom experiments. This optical system can be integrated in the existing setup of the Cretan Matter Waves lab, without any further modification in the current setup. The design and fabrication took into account the constraints of the existing setup, set mainly by the size of the vacuum cell where atoms are held; optimum performance of the new system was achieved given the limitations. The new optical system presents a significant improvement compared to the current optical system in use; it has about 8 times better resolution, almost 9 times better photon collection efficiency whilst consisting of one optical element less. The optical system has been fully constructed and characterized and will be soon incorporated in the Cretan Matter Wave BEC experiment.

The thesis also explores a novel method for imaging ultra-cold atoms based on the Faraday polarization rotation that light experiences as it travels through an atomic medium. Unlike the conventional absorption/fluorescence method, this imaging method does not destroy the quantum state of the atoms and causes minimal heating and therefore it can be used to monitor atomic dynamics and create squeezed states. We performed the first steps towards implementing this method by developing the optical setup for the probe beam and constructing the detection system. Special care was taken in order to develop a highly versatile and easily modifiable system, which can be readily integrated into the experimental setup that is currently in use. We performed off-

line experiments that confirmed that the designed system should meet the requirements of the non-destructive imaging experiment.

4 Appendices

Appendix A

A1 .Components list

Type	Product id	Specifications	Supplier
First Lens	49-116	Aspheric Lens EFL=37.5mm,600-1050nm coated, glass:L-BAL35	Edmund Optics
Second Lens	LF1544-B	Meniscus lens,EFL= -400mm,650-1050coated Glass:N-BK7	Thorlabs
Third Lens	LAO-155	Doublet lens,EFL=160mm,780nm coated,Glass: SSK4A & SF8	Melles griot
Mirror mount	KS1	Precision Kinematic Mirror mount Ø1" with three adjasters	Thorlabs
Objective's tube	-	Homemade, ertacetal tube designed to mount first ,second and third lenses	F.O.R.T.H workshop
Objective's base	-	Homemade, ertacetal orthogonal base for the objective	F.O.R.T.H workshop
Adaptor for mirror	-	Homemade 45 degrees aluminum Ø1" cylinder	F.O.R.T.H workshop
Base for mirror mount	-	Homemade aluminum cylinder with thread at each flat side	F.O.R.T.H workshop
Breadboard 1	-	Homemade aluminum plate with threads at specific points that holds the objective and the ccd camera	F.O.R.T.H workshop
Adaptor for I KON ccd	-	Homemade aluminum piece with holes for I KON ccd and translation stage mounting	F.O.R.T.H workshop

Adaptor for I XON ccd	-	Homemade aluminum piece with holes for I KON ccd and translation stage mounting	F.O.R.T.H workshop
Translation stage(x3)	M-UMR8.25	Steel ,1μm sensitivity	Newport
Right-angle plate	AP90	Holding between two breadboards	Thorlabs
Micrometer Heads(x3)	BM17.25	Micro scale resolution for translations stages motion	Newport
Breadboard 2	-	Homemade aluminum plate with threads at specific points that plays the role of a base of the whole optomechanical system	F.O.R.T.H workshop
Ring 1	-	Homemade plastic cylindrical spacer for the first and second lenses	F.O.R.T.H workshop
Ring 2	-	Homemade plastic cylindrical spacer with throws for mounting third lens	F.O.R.T.H workshop
i Kon-M ccd camera	iKon-M 934 BR-DD		Andor Technology
iXon Ultra 897 ccd camera	iXon –Ultra 897		Andor Technology

Table A1*. List of ordered and homemade components.*

A2. Review of materials and technologies

Ertacetal

In order to achieve large numerical aperture, the objective was designed to be placed very close to the vacuum cell's window. This introduces some constraints at materials that could be used for the lens mount. At the most of the steps, in cold atoms experiments , a combination of magnetic fields are used. The abrupt switch off of all magnetic fields is very important for a successful BEC atom imaging experiment. This means that in order to avoid eddy currents, the components that will be placed near the vacuum cell should be non-metallic materials. This led us to choose a carbonylic plastic for the objective's construction. Another important parameter is that the temperature outside the vacuum cell is almost constant, so thermal expansion phenomena can be ignored in this case.

Aluminum

As it was referred above most of the parts that were used for the final assembly are homemade. The components, except of the objective, are far enough from the magnetic fields and the vacuum cell, so the materials that were made doesn't affect experiment's resolution .This made simpler the material choice so the other homemade components were made of aluminum .Aluminum combines a lot of benefits in our case : it is lightweight, strong enough for this application, non-corrosive ,easy to handle and less expensive than other metals.

Lens Coating

As it was referred in the main part of this thesis the signal from atom cloud photon emission in an atom cloud imaging experiments is very weak. This affects in many ways the optical design of a system that is designed to observe atomic clouds. Transmission losses during the imaging process is something that must be taken into consideration and be limited as best as possible. In order to achieve this we chose commercially available suitable antireflected coated lens for the objective .The wavelength that is used in the experiment is 780nm so that the

lenses do not reflect a range at electromagnetic spectrum that contains the main wavelength.

Antireflection coating specifications for each lens:

- *49116 (Edmund Optics)*

  NIR coating

  R_{avg} ≤1.5% at the range 600nm-1050nm

- *LF1544-B(Thorlabs)*

  AR coating

  R_{avg} <0.5% at the range 650nm-1050nm

- *LAO-155(Melles Griot)*

  Custom antireflection coated at a central wavelength of 780 nm with R_{avg}<0.03%

Appendix B

At this appendix all the technical drawings are attached. At the first part are attached the homemade components that were made with the I.E.L.S's workshop help and at the second part the ordered components. Finally at the third part are shown the total assemblies for both cameras.

Part 1

The technical drawings are shown in a arbitrary order. These are the technical drawings that were used by the IESL workshop to machine the parts.

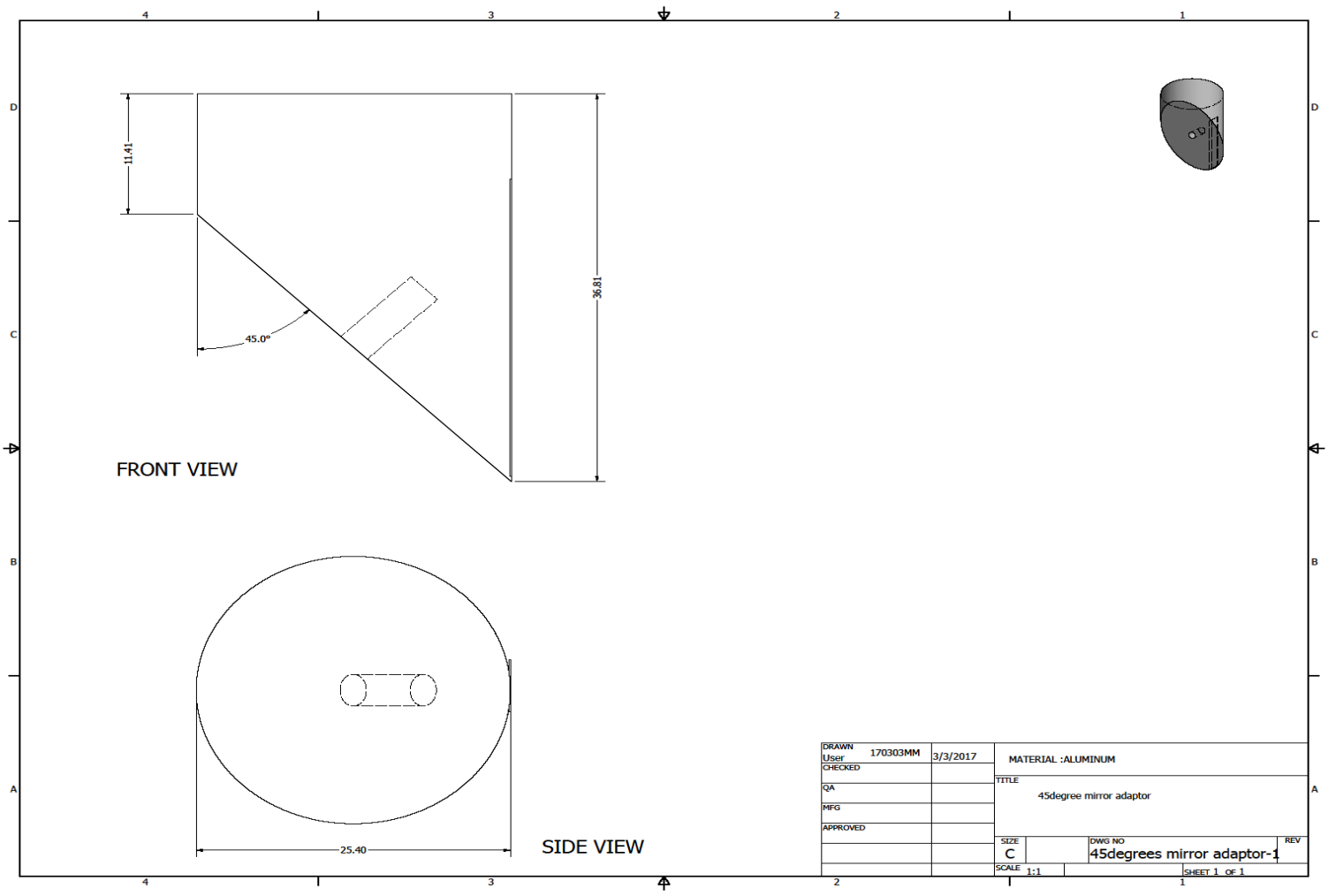
11.41
36.81
45.0°
FRONT VIEW
25.40
SIDE VIEW
DRAWN
User 170303MM
3/3/2017
CHECKED
QA
MFG
APPROVED
MATERIAL :ALUMINUM
TITLE
45degree mirror adaptor
SIZE
C
DWG NO
45degrees mirror adaptor-1
REV
SCALE 1:1
SHEET 1 OF 1

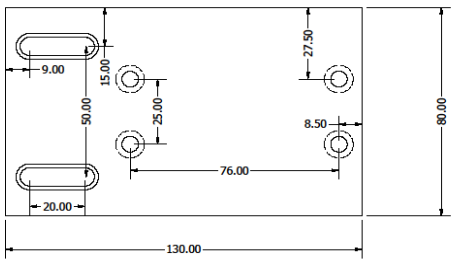

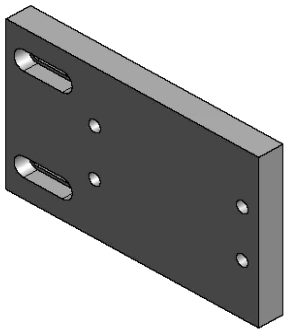

TOP VIEW

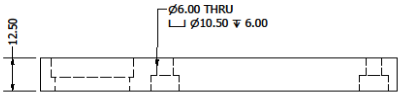

SIDE VIEW

DRAWN User 170303MM	3/3/2017	MATERIAL ALUMINUM	
CHECKED		TITLE: ADAPTOR FOR I XON	
QA			
MFG			
APPROVED		SIZE: C	DWG NO: Adaptor for i Xon — REV
		SCALE: 1:1	SHEET 1 OF 1

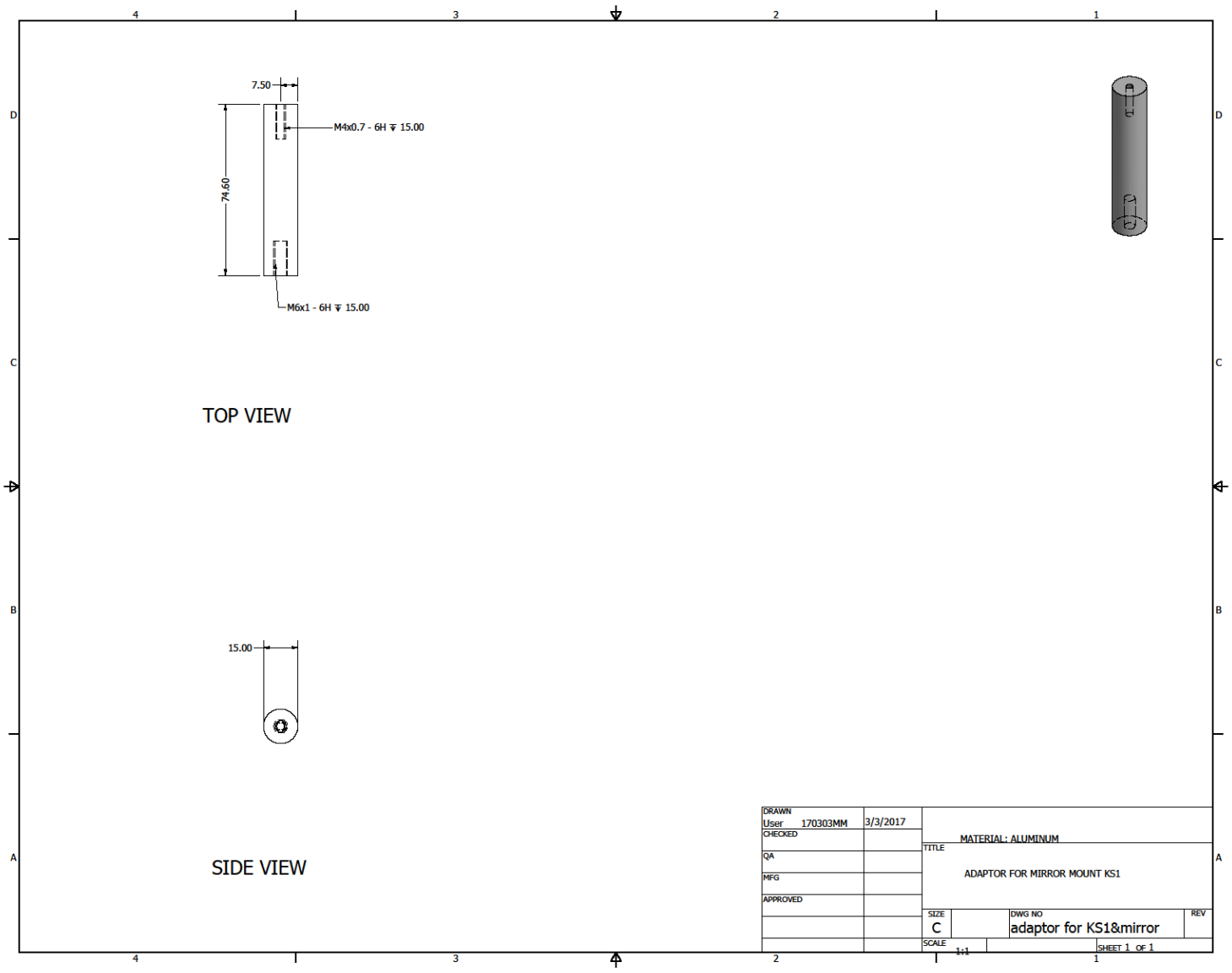
7.50
M4x0.7 - 6H ↧ 15.00
74.60
M6x1 - 6H ↧ 15.00
TOP VIEW
15.00
SIDE VIEW
DRAWN
User 170303MM
3/3/2017
CHECKED
QA
MFG
APPROVED
MATERIAL: ALUMINUM
TITLE
ADAPTOR FOR MIRROR MOUNT KS1
SIZE
C
DWG NO
adaptor for KS1&mirror
REV
SCALE
1:1
SHEET 1 OF 1

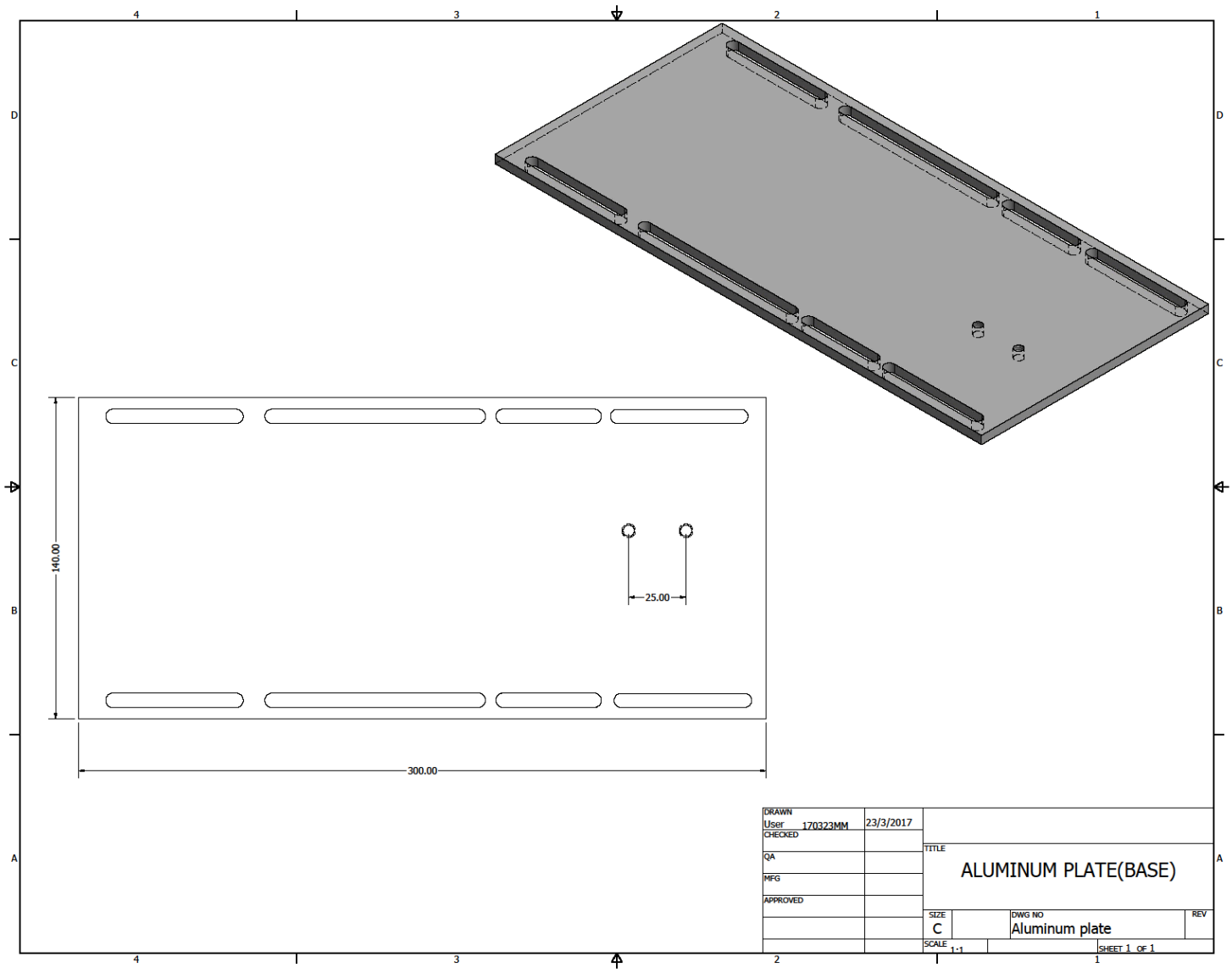

DRAWN User 170323MM	23/3/2017		
CHECKED		TITLE	ALUMINUM PLATE(BASE)
QA			
MFG			
APPROVED		SIZE C	DWG NO Aluminum plate REV
		SCALE 1:1	SHEET 1 OF 1

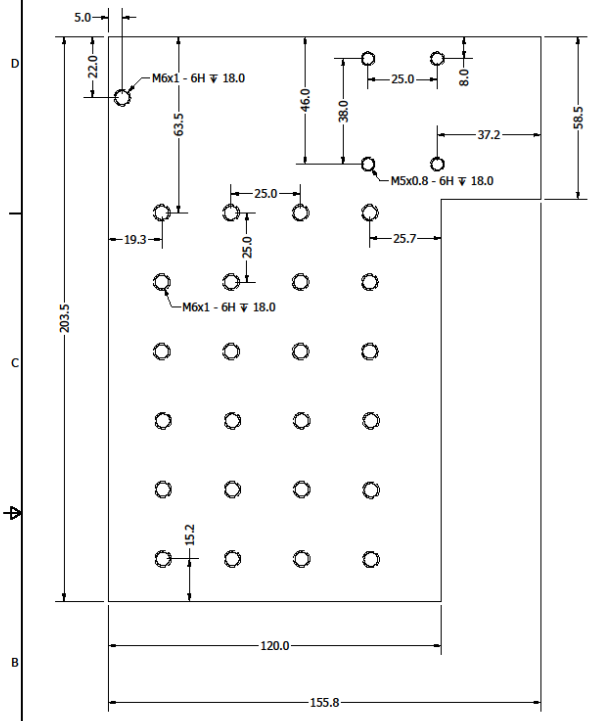

TOP VIEW

SIDE VIEW

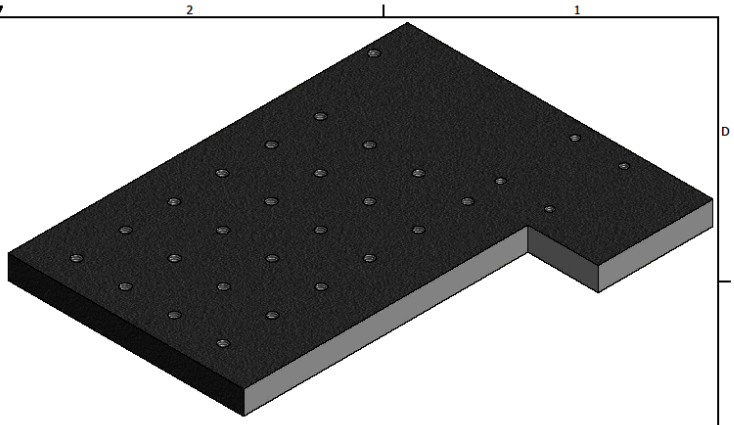

DRAWN User 170303MM	3/3/2017	MATERIAL: ALUMINUM	
CHECKED		TITLE	
QA		BREADBOARD	
MFG			
APPROVED		SIZE C	DWG NO breadboard-1 REV
		SCALE 1:1	SHEET 1 OF 1

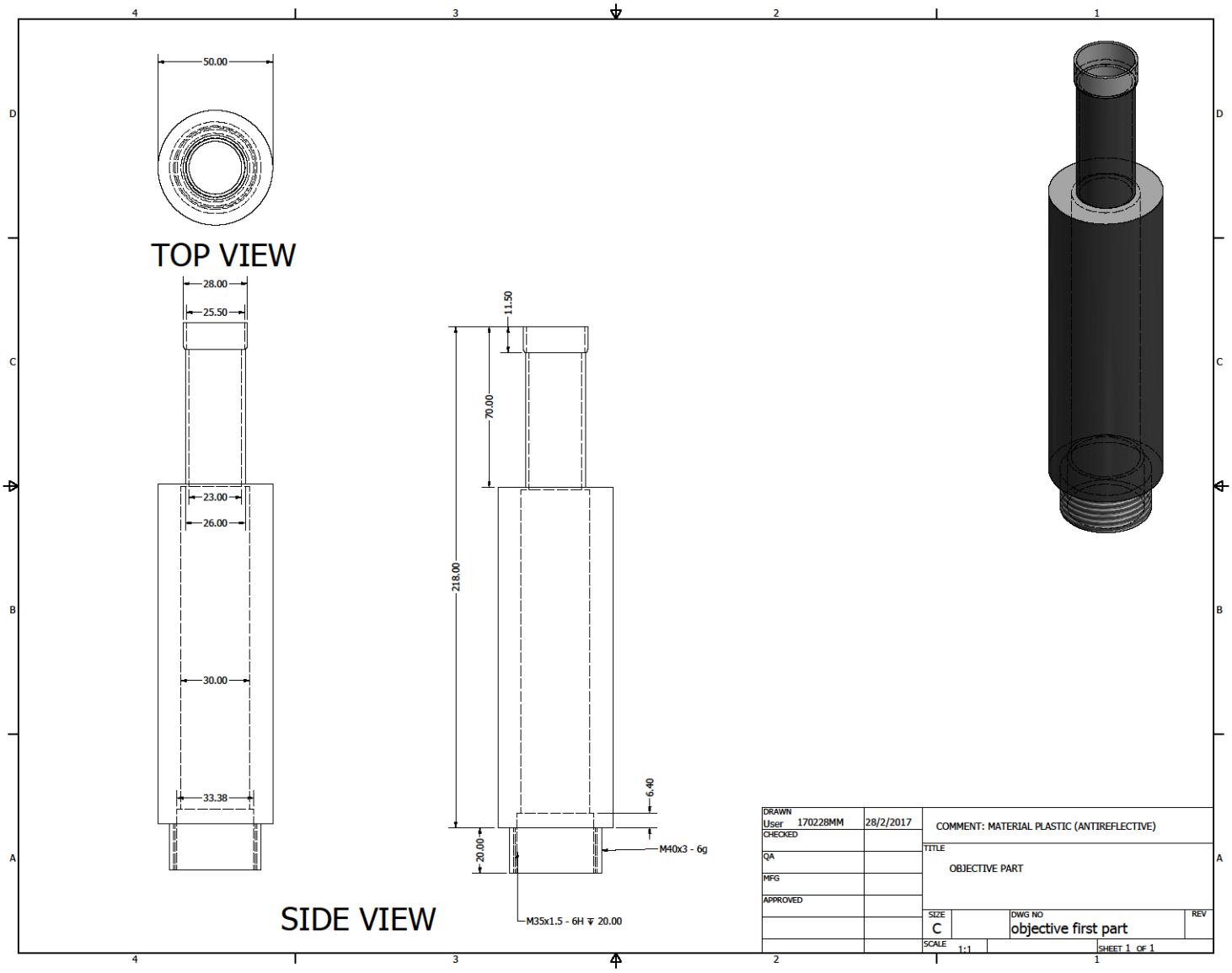
50.00
TOP VIEW
28.00
25.50
23.00
26.00
30.00
33.38
11.50
70.00
218.00
6.40
20.00
M40x3 - 6g
M35x1.5 - 6H ↧ 20.00
SIDE VIEW
DRAWN
User 170228MM
28/2/2017
CHECKED
QA
MFG
APPROVED
COMMENT: MATERIAL PLASTIC (ANTIREFLECTIVE)
TITLE
OBJECTIVE PART
SIZE
C
DWG NO
objective first part
REV
SCALE 1:1
SHEET 1 OF 1

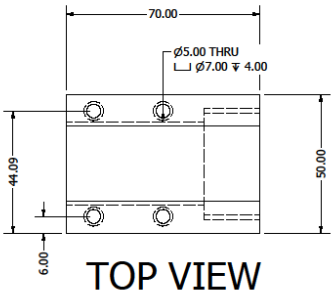

TOP VIEW

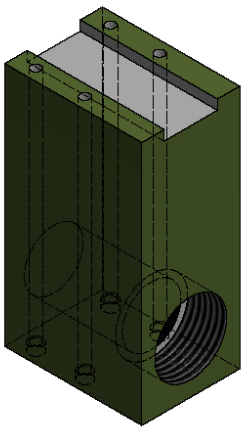

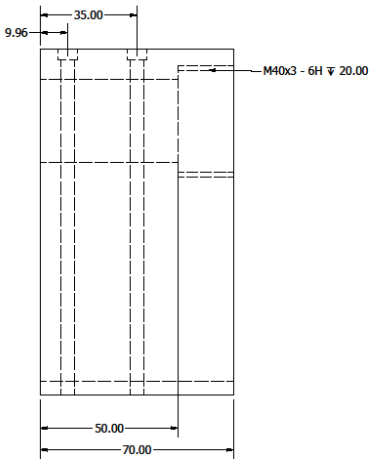

SIDE VIEW

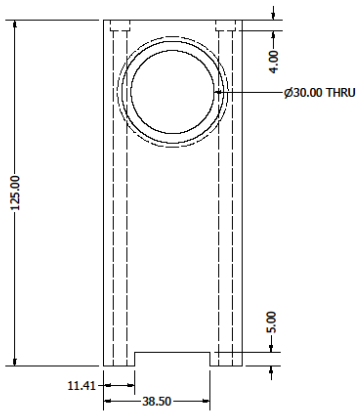

FRONT VIEW

DRAWN User 170228MM	28/2/2017	COMMENT:MATERIAL PLASTIC (ANTIREFLECTIVE)	
CHECKED		TITLE: OBJECTIVE BASE	
QA			
MFG			
APPROVED		SIZE C	DWG NO qubic part (objective)side1 REV
		SCALE 1:1	SHEET 1 OF 1

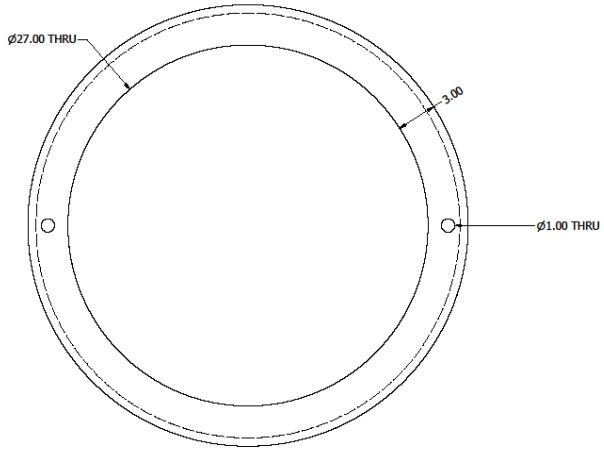

TOP VIEW

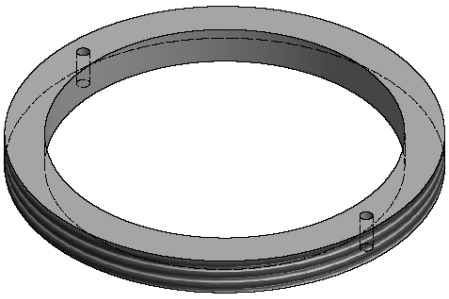

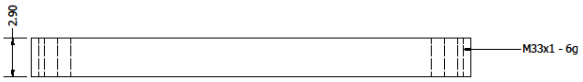

SIDE VIEW

DRAWN User 170228MM	28/2/2017	COMMENT: MATERIAL PLASTIC	
CHECKED		TITLE	
QA		RING 1	
MFG			
APPROVED		SIZE C	DWG NO Ring 1 REV
		SCALE 1:1	SHEET 1 OF 1

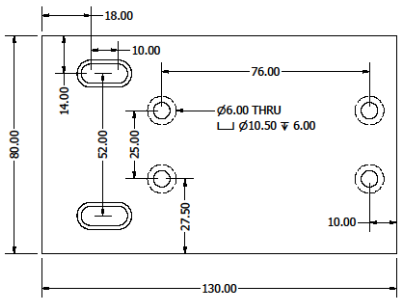

TOP VIEW

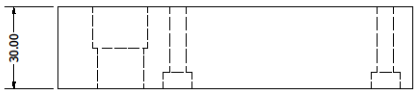

SIDE VIEW

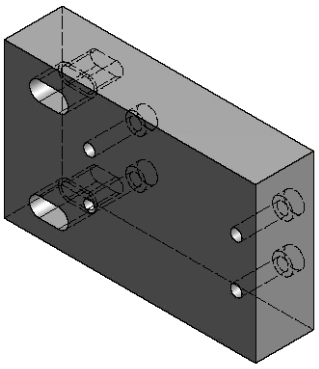

DRAWN User 170303MM	3/3/2017	MATERIAL ALUMINUM	
CHECKED		TITLE ADAPTOR FOR I KON	
QA			
MFG			
APPROVED		SIZE C	DWG NO 170215MM_Adaptor for iKon-1 REV
		SCALE 1:1	SHEET 1 OF 1

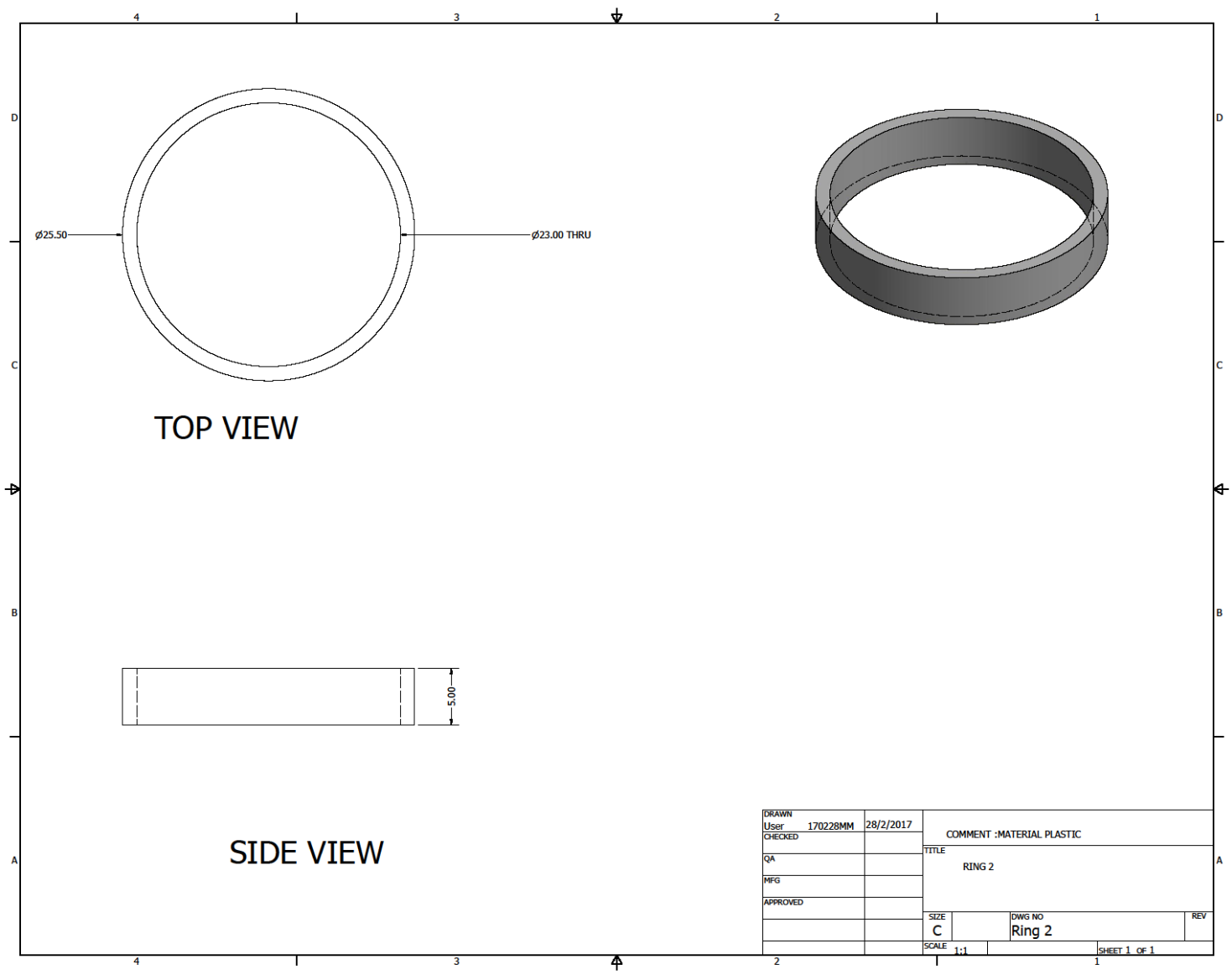

Part 2

At the second part of this appendix are shown the technical drawings of the ordered components that were used in a random order.

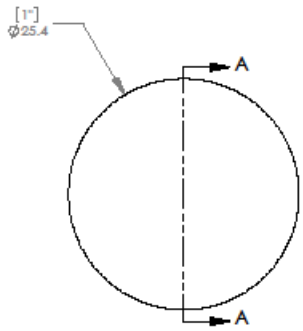

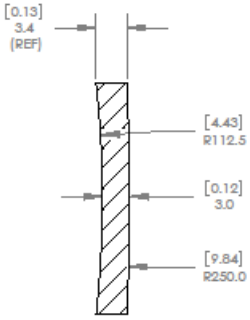

SECTION A-A

1:1 ISOMETRIC VIEW FOR REFERENCE ONLY

NOTES/SPECIFICATIONS:
1. DESIGN WAVELENGTH: 587.6nm
2. FOCAL LENGTH: f=-398.6mm ± 1%
3. BACK FOCAL LENGTH(REF): bf=-397.0mm
4. CLEAR APERTURE: >90%
5. SURFACE QUALITY: 40-20 SCRATCH-DIG
6. CENTRATION: <3arcmin
7. DIAMETER TOLERANCE: +0.0/-0.1mm
8. THICKNESS TOLERANCE: ±0.1mm
9. COATING: BBAR Ravg<0.5% FROM 650nm-1050nm, 0° AOI, ON OUTER OPTICAL SURFACES

ALL DIMENSIONS ARE IN THE FORM [in] / mm.

THIS DRAWING IS FOR INFORMATION ONLY
NOT INTENDED FOR MANUFACTURING

	NAME	DATE
DRAWN	WD	11/19/2009
ENG APPR.	BW	11/24/2009
MFG APPR.	DD	12/09/2009

THORLABS INC. PO BOX 366 NEWTON NJ

TITLE: D=25.4 F=-400.0 N-BK7 B COAT - MENISCUS LENS

MATERIAL: N-BK7 | SIZE: A | REV.: B

SCALE: 2:1 | SHEET 1 OF 1

DWG. NO. 4893-E01 | PART NO. LF1544-B

5 4 3 2 1

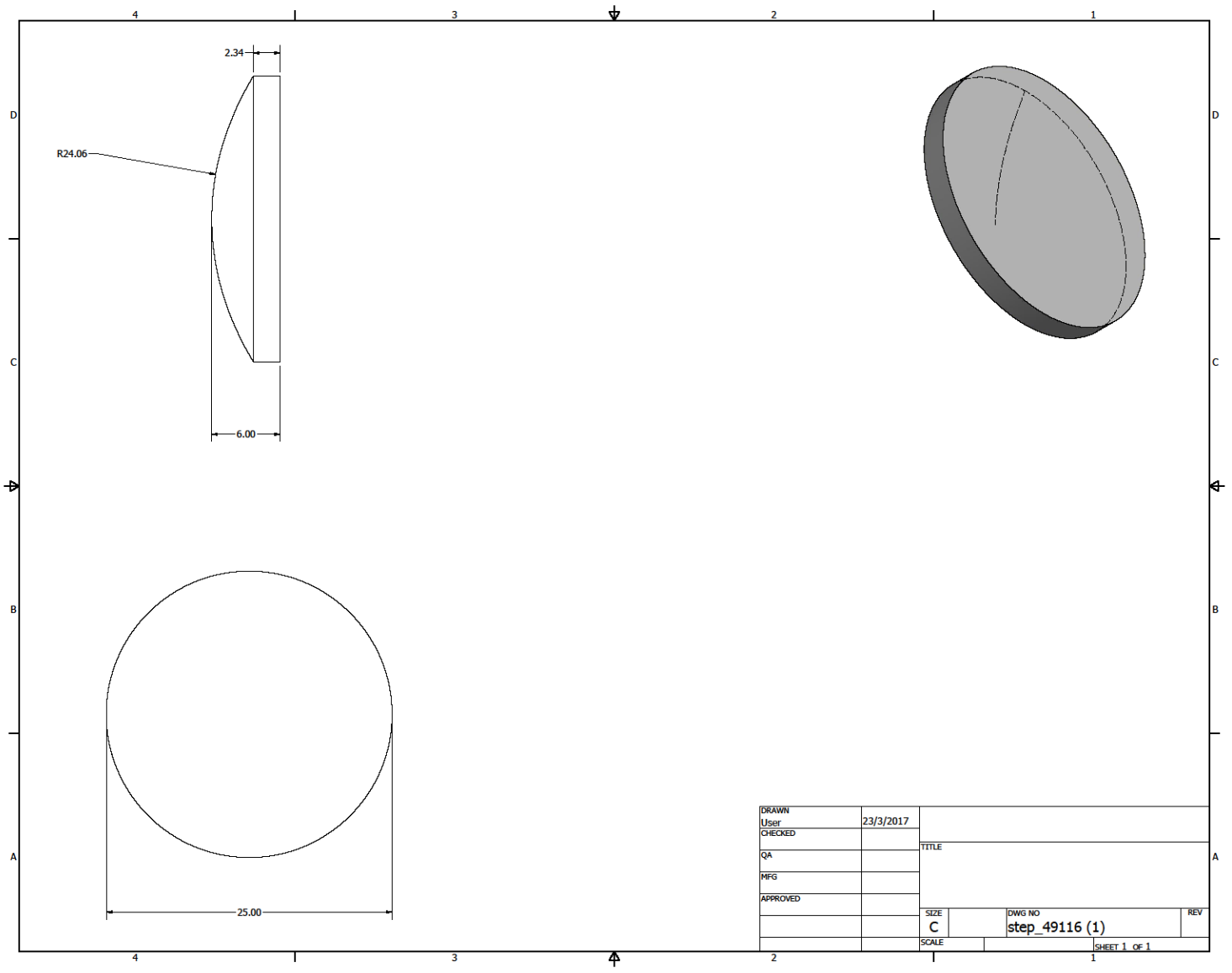
2.34
R24.06
6.00
25.00
DRAWN
User
23/3/2017
CHECKED
QA
MFG
APPROVED
TITLE
SIZE
C
DWG NO
step_49116 (1)
REV
SCALE
SHEET 1 OF 1

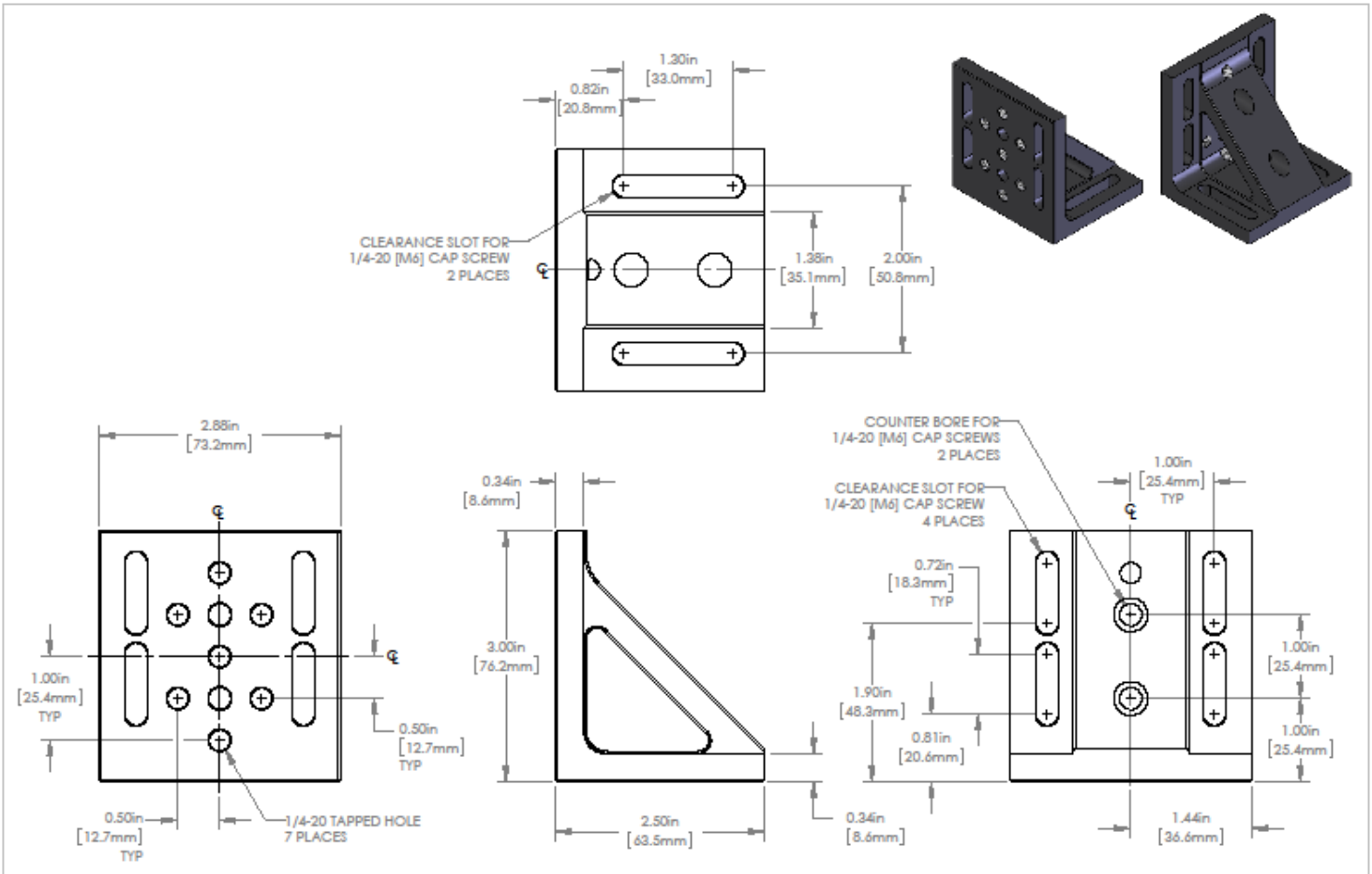

DRAWING PROJECTION		
	NAME	DATE
DRAWN	AV	06/JUN/13
APPROVAL	BM	20/FEB/13

VALUES IN PARENTHESIS ARE CALCULATED AND MAY CONTAIN ROUNDOFF ERRORS

THORLABS
www.thorlabs.com

ANGLE PLATE

MATERIAL	REV
BLACK ANODIZED ALUMINUM	C

ITEM #	APPROX WEIGHT
AP90	0.26 kg

FOR INFORMATION ONLY
NOT FOR MANUFACTURING PURPOSES

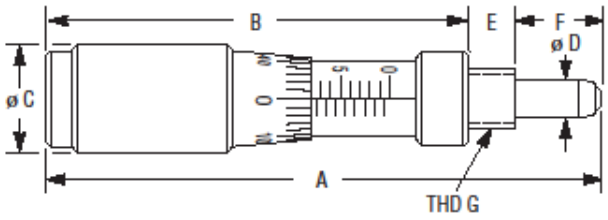

Dimensions [in. (mm)]									Thread
Model	**A**	**B Min**	**B Max**	**C**	**D**	**E**	**F Min**	**F Max**	**G**
BM11.5	1.36 (34.5)	1.00 (25.5)	1.20 (30.5)	0.43 (11)	0.16 (4)	0.13 (3.2)	0.03 (0.8)	0.23 (5.8)	M6 x 0.50
BM11.10	2.01 (51)	1.40 (35.5)	1.79 (45.5)	0.43 (11)	0.16 (4)	0.19 (4.7)	0.03 (0.8)	0.43 (10.8)	M6 x 0.50
BM11.16	2.24 (57)	1.40 (35.5)	2.03 (51.5)	0.43 (11)	0.16 (4)	0.19 (4.7)	0.03 (0.8)	0.66 (16.8)	M6 x 0.50
BM11.25	3.00 (76.2)	1.81 (46)	2.80 (71)	0.43 (11)	0.16 (4)	0.19 (4.7)	0.02 (0.5)	0.98 (25)	M6 x 0.50
BM17.25	3.25 (82.5)	1.95 (49.5)	2.93 (74.5)	0.67 (17)	0.28 (7.2)	0.28 (7.2)	0.03 (0.8)	1.01 (25.8)	M12 x 0.50
BM17.51	5.43 (138)	3.04 (77.1)	5.04 (128.1)	0.67 (17)	0.28 (7.2)	0.28 (7.2)	0.09 (2.4)	2.10 (53.4)	M12 x 0.50
BM25.40	4.92 (125)	2.72 (69)	4.29 (109)	0.98 (25)	0.31 (8)	0.57 (14.5)	0.12 (3)	1.69 (43)	M18 x 1.00
BM25.63	6.79 (172.5)	3.70 (94)	6.18 (157)	0.98 (25)	0.31 (8)	0.57 (14.5)	0.04 (1)	2.52 (64)	M18 x 1.00
BM32.80	8.35 (212)	4.17 (106)	7.32 (186)	1.26 (32)	0.47 (12)	0.94 (24)	0.08 (2)	3.23 (82)	M22 x 1.00

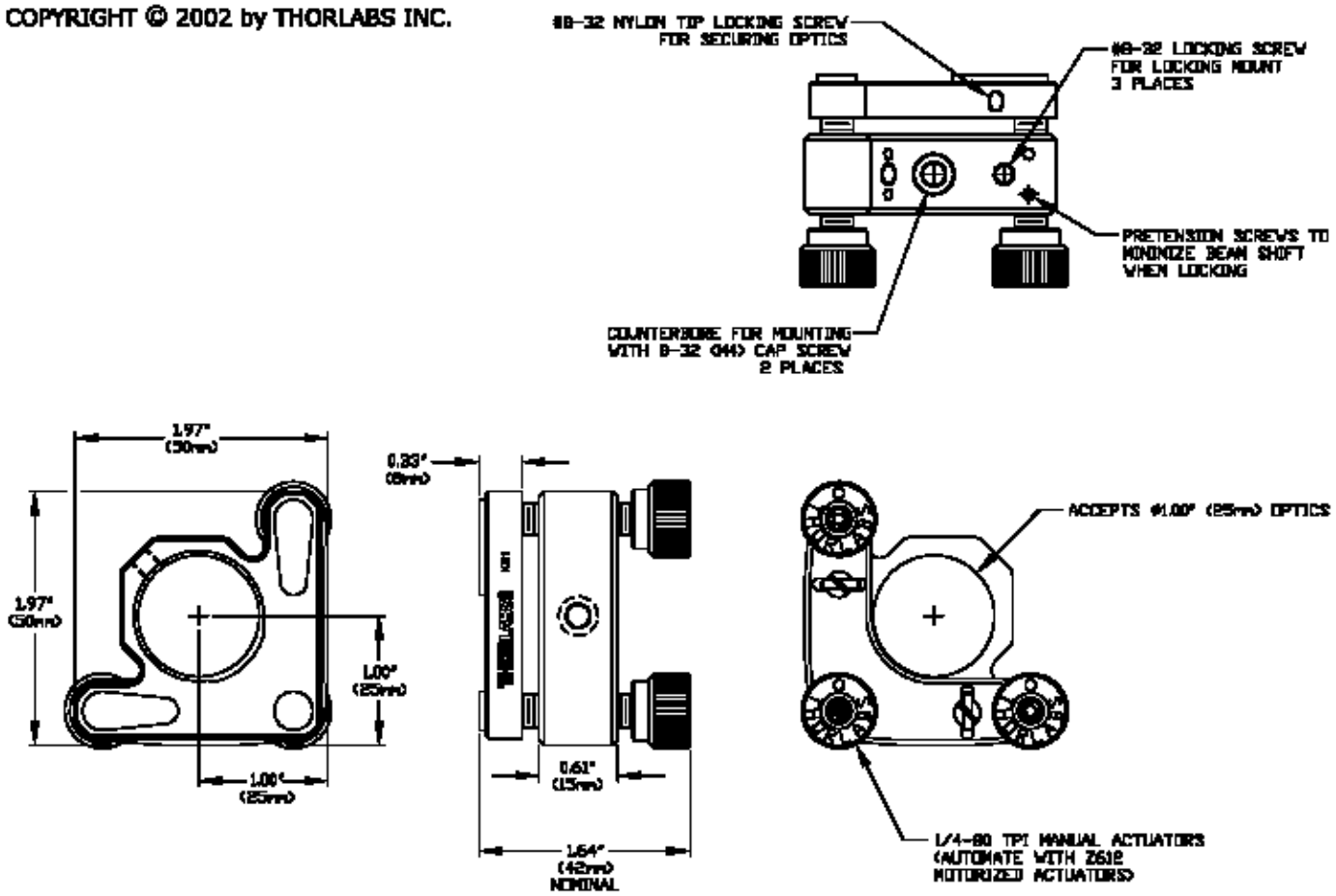

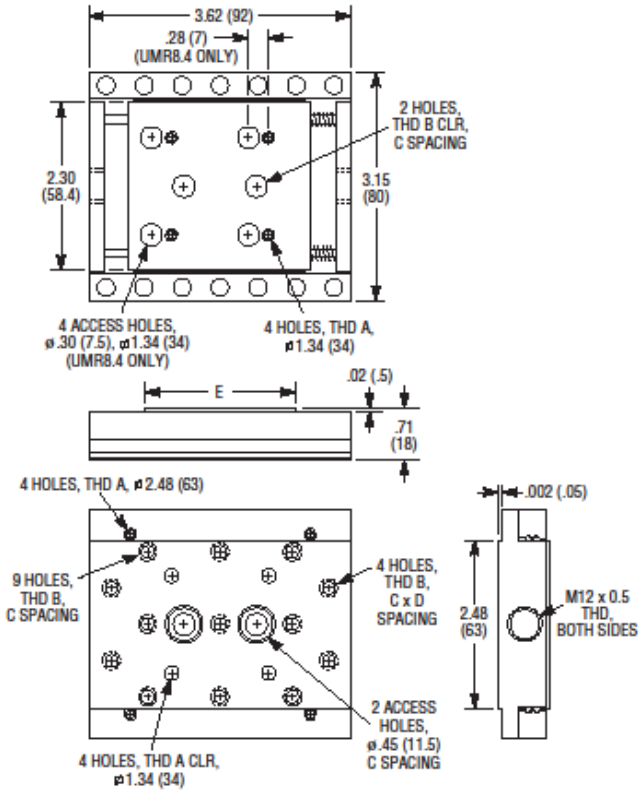

Model (Metric)	Thread A	Dimensions [(mm)] B	C	D	E
UMR8.4	8-32 (M4)	1/4-20 (M6)	1.00 (25.0)	3.000 (75.0)	2.52 (64)
UMR8.25	8-32 (M4)	1/4-20 (M6)	1.00 (25.0)	3.000 (75.0)	2.09 (53)
UMR8.51	8-32 (M4)	1/4-20 (M6)	1.00 (25.0)	3.000 (75.0)	

Newport

Part 2

Total assemblies for both cameras :

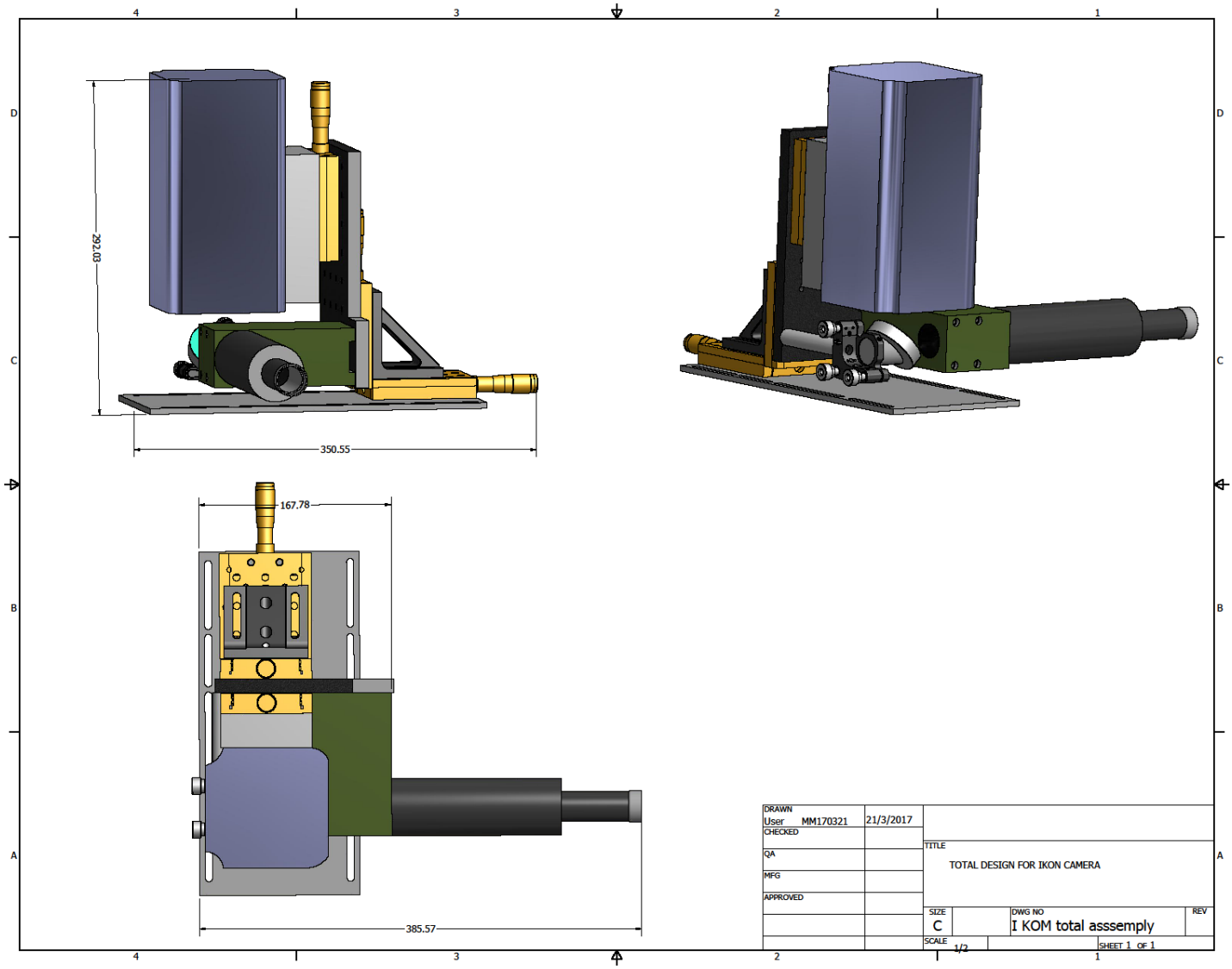

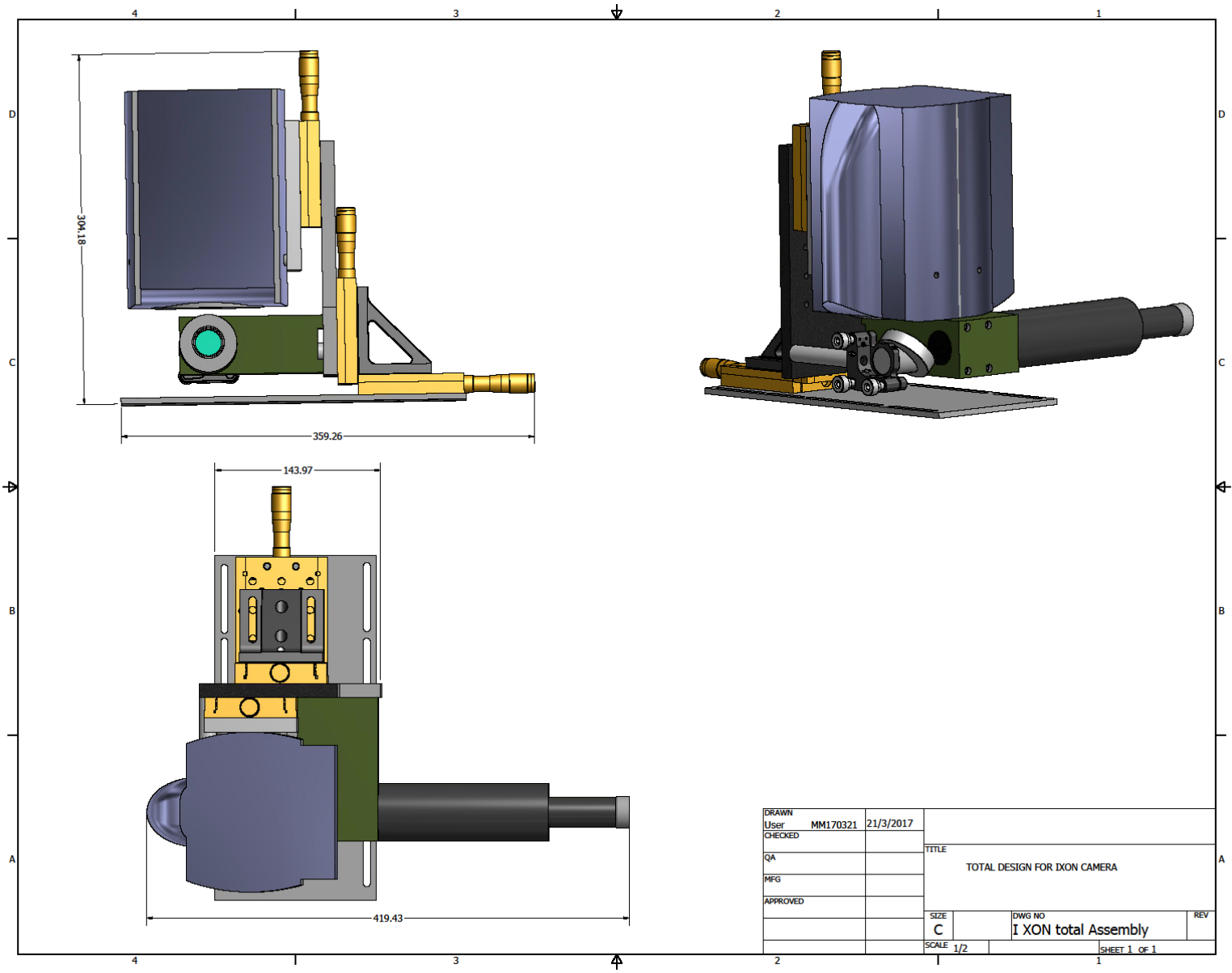
304.18
359.26
143.97
419.43
DRAWN
User MM170321
21/3/2017
CHECKED
QA
MFG
APPROVED
TITLE
TOTAL DESIGN FOR IXON CAMERA
SIZE
C
DWG NO
I XON total Assembly
REV
SCALE 1/2
SHEET 1 OF 1

Appendix C

Zemax is a software which can model, analyze, and assist in the design of optical systems. A more detailed description of the raytracing Zemax software that we used in order to design, optimize and characterize optical systems presented at this appendix. Diagrams and diagnostics that are presented at the main text of this thesis described below.

Optical Layout

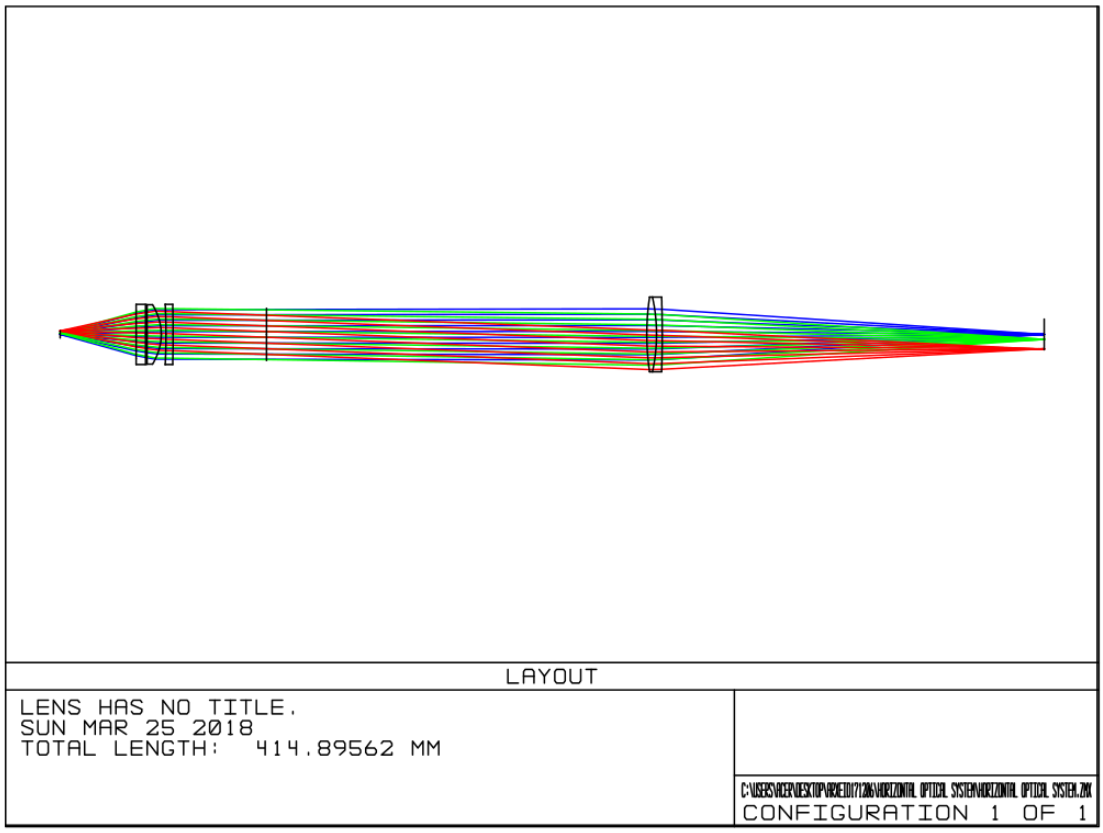

Figure C.1. Optical layout at Zemax software. This is a YZ cross section through the lens.

One of Zemax widely used diagrams is the optical layout. Optical layout is a perpendicular to the optical axis cross section through the lens. Different colors stand for rays that start from different heights at the object space which are

defined different fields at Zemax dialog boxes. Optical layout gives a schematic representation of the designed optical system.

Spot size diagram

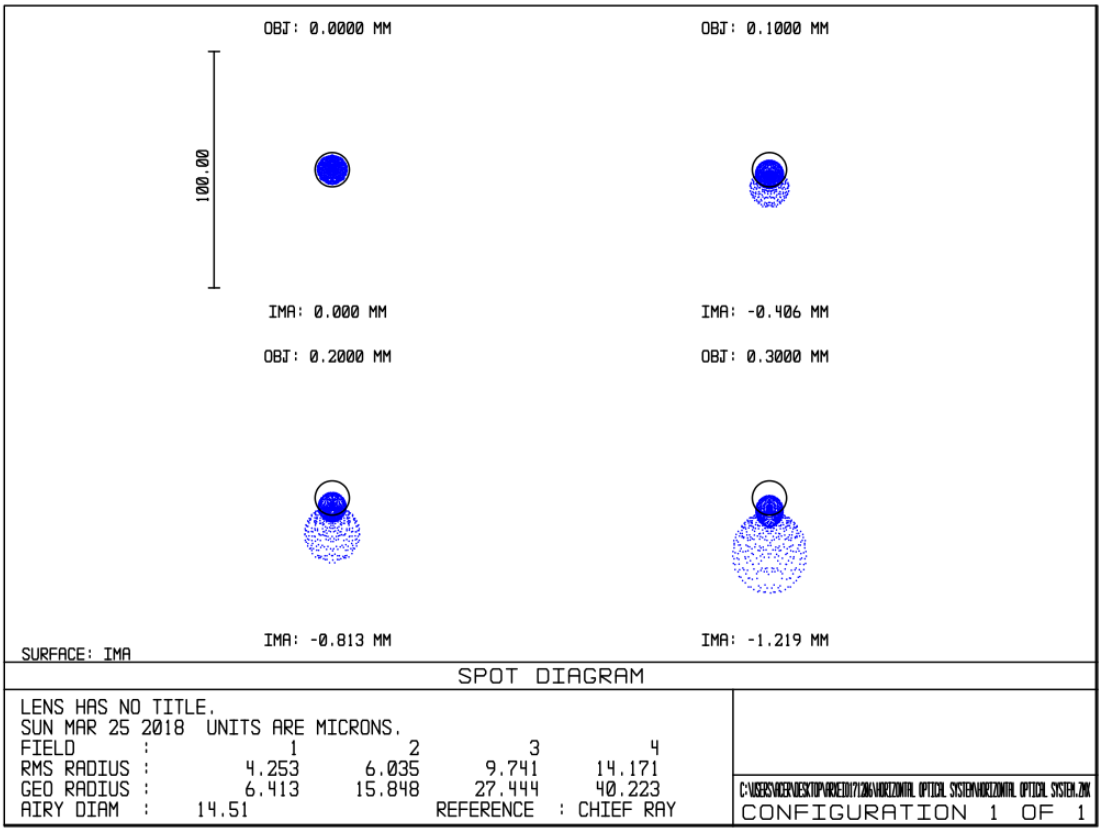

Figure C.2.Spot size diagram at Zemax software.

One of the most basic analysis diagnostics in Zemax is the spot diagram. This feature traces many rays from a single source point in object space, propagates all the rays through the optical system, and plots the (x, y) coordinates of all the rays at the image plane. Spot size diagram is a collection of points. Each point representing a single ray. There is no interaction or interference between the rays. Each spot at this diagram corresponds to a different field at object space. The spot diagram is very effective at showing the effects of the ray aberrations. The black circle at each field spot diagram represents the Airy disk diameter.(diffraction limit). The spot size diagram is

reliable only if the spot size of a field is larger than diffraction limit. The spot diagram is useful if the aberrations are large and the optical system is not diffraction limited.

RMS vs field diagram

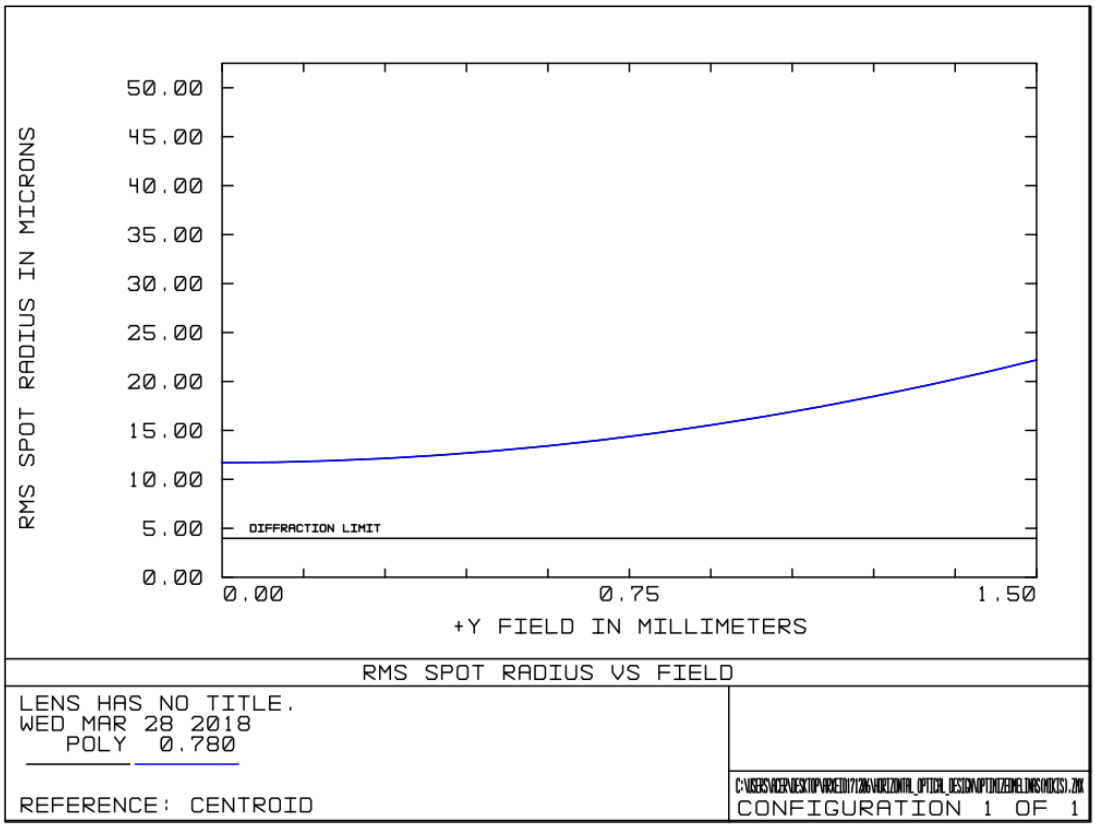

Figure C.3. Rms vs field diagram at Zemax software.

Another useful tool at Zemax software is the Rms spot radius vs field diagram. This diagram represents how the rms spot radius evolves as the field increases. This enables to the user a clear view regarding to the performance of the optical setup in different fields. At the bottom of the diagram the user can select to

appear the diffraction limit (black line at the diagram above). The Rms spot diagram is reliable if the Rms spot radius is larger than the diffraction limit.

Vignetting diagram

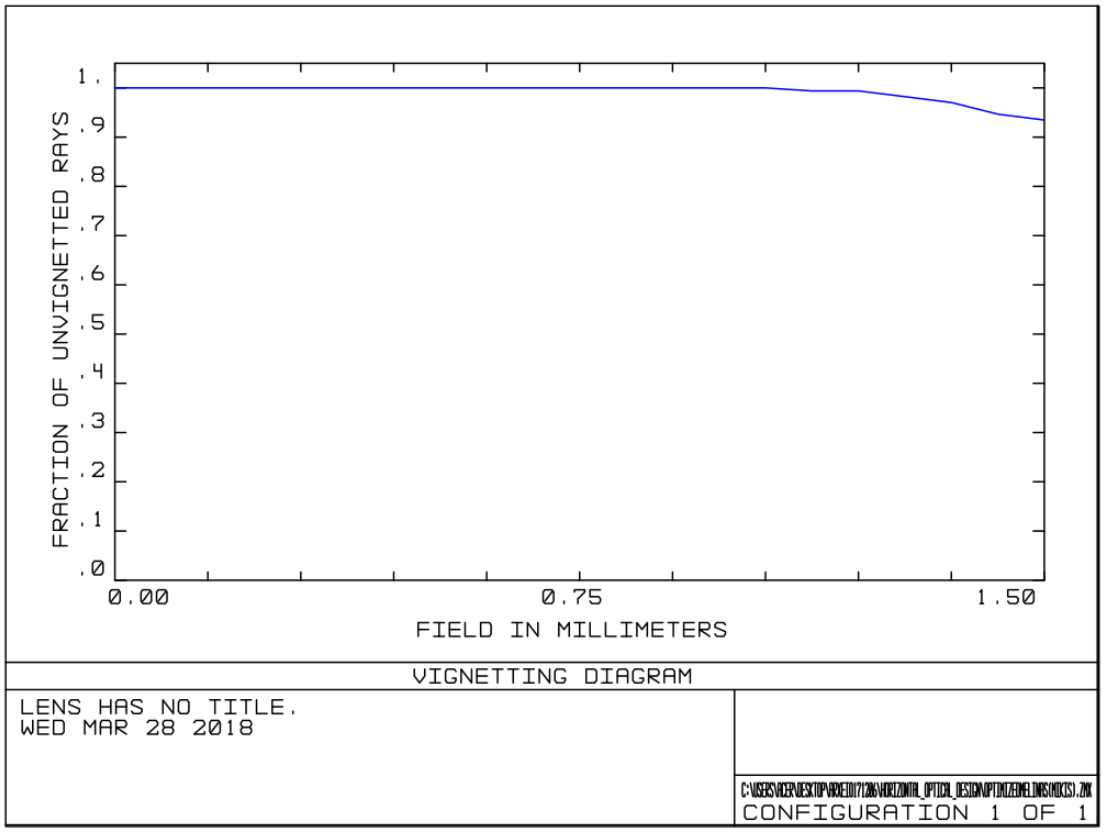

Figure C.5. Vignetting diagram at Zemax software

Vignetting diagram calculates vignetting as a function of field position. At this graph, user can observe the fraction of the rays that reach the image plane. Generally speaking this diagnostic is valid only for rotationally symmetric optical systems.

5 Bibliography

[1] M. H. Anderson, J. R. Ensher, M. R. Matthews, C. E. Wieman, and E. A. Cornell, "Observation of bose-einstein condensation in a dilute atomic vapor.," *Science*, vol. 269, no. 5221, pp. 198–201, Jul. 1995.

[2] I. Bloch, J. Dalibard, and W. Zwerger, "Many-body physics with ultracold gases," *Rev. Mod. Phys.*, vol. 80, no. 3, pp. 885–964, Jul. 2008.

[3] A. Ramanathan, K. C. Wright, S. R. Muniz, M. Zelan, W. T. Hill, C. J. Lobb, K. Helmerson, W. D. Phillips, and G. K. Campbell, "Superflow in a Toroidal Bose-Einstein Condensate: An Atom Circuit with a Tunable Weak Link," *Phys. Rev. Lett.*, vol. 106, no. 13, p. 130401, Mar. 2011.

[4] B. Zimmermann, T. Müller, J. Meineke, T. Esslinger, and H. Moritz, "High-resolution imaging of ultracold fermions in microscopically tailored optical potentials," *New J. Phys.*, vol. 13, no. 4, p. 43007, 2011.

[5] A. L. Gaunt and Z. Hadzibabic, "Robust Digital Holography For Ultracold Atom Trapping," *Sci. Rep.*, vol. 2, p. 721, Oct. 2012.

[6] N. Schlosser, G. Reymond, I. Protsenko, and P. Grangier, "Sub-poissonian loading of single atoms in a microscopic dipole trap," *Nature*, vol. 411, p. 1024, Jun. 2001.

[7] J. F. Sherson, C. Weitenberg, M. Endres, M. Cheneau, I. Bloch, and S. Kuhr, "Single-atom-resolved fluorescence imaging of an atomic Mott insulator," *Nature*, vol. 467, no. 7311, pp. 68–72, 2010.

[8] M. J. Piotrowicz, M. Lichtman, K. Maller, G. Li, S. Zhang, L. Isenhower, and M. Saffman, "Two-dimensional lattice of blue-detuned atom traps using a projected Gaussian beam array," *Phys. Rev. A*, vol. 88, no. 1, p. 13420, Jul. 2013.

[9] F. Nogrette, H. Labuhn, S. Ravets, D. Barredo, L. Béguin, A. Vernier, T. Lahaye, and A. Browaeys, "Single-Atom Trapping in Holographic 2D Arrays of Microtraps with Arbitrary Geometries," *Phys. Rev. X*, vol. 4, no. 2, p. 21034, May 2014.

[10] M. Pappa, “Imaging Bose-Einstein Condensates at Ultra-Low Atom-Numbers and Time Averaged Adiabatic Potentials,” no. June, 2011.

[11] J. R. Anglin and W. Ketterle, “Bose–Einstein condensation of atomic gases,” *Nature*, vol. 416, p. 211, Mar. 2002.

[12] M. Pappa, P. C. Condylis, G. O. Konstantinidis, V. Bolpasi, A. Lazoudis, O. Morizot, D. Sahagun, M. Baker, and W. Von Klitzing, “Ultra-sensitive atom imaging for matter-wave optics,” *New J. Phys.*, vol. 13, 2011.

[13] A. Fuhrmanek, A. M. Lance, C. Tuchendler, P. Grangier, Y. R. P. Sortais, and A. Browaeys, “Imaging a single atom in a time-of-flight experiment,” *New J. Phys.*, vol. 12, no. 5, p. 53028, 2010.

[14] Andrews, Mewes, van D. NJ, Durfee, Kurn, and Ketterle, “Direct, Nondestructive Observation of a Bose Condensate,” *Science*, vol. 273, no. 5271, pp. 84–87, Jul. 1996.

[15] M. R. Andrews, D. M. Kurn, H.-J. Miesner, D. S. Durfee, C. G. Townsend, S. Inouye, and W. Ketterle, “Propagation of Sound in a Bose-Einstein Condensate,” *Phys. Rev. Lett.*, vol. 79, no. 4, pp. 553–556, Jul. 1997.

[16] C. C. Bradley, C. A. Sackett, and R. G. Hulet, “Bose-Einstein Condensation of Lithium: Observation of Limited Condensate Number,” *Phys. Rev. Lett.*, vol. 78, no. 6, pp. 985–989, Feb. 1997.

[17] M. Gajdacz, A. J. Hilliard, M. A. Kristensen, P. L. Pedersen, C. Klempt, J. J. Arlt, and J. F. Sherson, “Preparation of Ultracold Atom Clouds at the Shot Noise Level,” *Phys. Rev. Lett.*, vol. 117, no. 7, p. 73604, Aug. 2016.

[18] J. Pérez-Ríos and A. S. Sanz, “How does a magnetic trap work?,” *Am. J. Phys.*, vol. 81, no. 11, pp. 836–843, 2013.

[19] D. V Vasilyev, K. Hammerer, N. Korolev, and A. S. Sørensen, “Quantum noise for Faraday light–matter interfaces,” *J. Phys. B At. Mol. Opt. Phys.*, vol. 45, no. 12, p. 124007, 2012.

[20] D. Budker, W. Gawlik, D. F. Kimball, S. M. Rochester, V. V Yashchuk, and A.

Weis, “Resonant nonlinear magneto-optical effects in atoms,” *Rev. Mod. Phys.*, vol. 74, no. 4, pp. 1153–1201, Nov. 2002.

[21] W. Petrich, M. H. Anderson, J. R. Ensher, and E. A. Cornell, “Stable, Tightly Confining Magnetic Trap for Evaporative Cooling of Neutral Atoms,” *Phys. Rev. Lett.*, vol. 74, no. 17, pp. 3352–3355, Apr. 1995.

[22] J. M. Geary, *Introduction to Lens Design: With Practical ZEMAX Examples*. Willmann-Bell, 2002.

[23] D. G. Papazoglou, “Notes for course’’Foundation of Modern Optics’’.”

[24] E. Hecht, *Optics*. Addison-Wesley, 2002.

[25] J. E. Greivenkamp, *Field Guide to Geometrical Optics*. 2004.

[26] W. Smith, *Modern Lens Design*. Mcgraw-hill, 2004.

[27] R. Kingslake, *Applied Optics and Optical Engineering*, no. $τ$. 1. Academic Press, 1965.

[28] V. N. Mahajan, *Optical Imaging and Aberrations: Ray geometrical optics*, no. $μ$. 1-2. SPIE Optical Engineering Press, 1998.

[29] D. S. Simon, *A Guided Tour of Light Beams: From Lasers to Optical Knots*. Morgan & Claypool Publishers, 2016.

[30] A. E. Siegman, *Lasers*. University Science Books, 1986.

[31] I. Drougkakis, “Vibrational and Angular Stability of Optical Systems for Space Applications,” 2016.

[32] K. Mavrakis, “Novel optical breadboard beam steering techniques for space applications.”

[33] G. Baldwin, F. Gonzales, and C. Perez-Santos, “First Peruvian Binoculars,” in *Optical Design and Fabrication 2017 (Freeform, IODC, OFT)*, 2017, p. JTu5A.4.

[34] K. J. Kasunic, *Optomechanical Systems Engineering*. Wiley, 2015.

[35] P. Yoder, D. Vukobratovich, and R. A. Paquin, *Opto-Mechanical Systems Design, Second Edition,*. Taylor & Francis, 1992.

[36] T. E. Jeffries, W. T. Perkins, and N. J. G. Pearce, "Comparisons of infrared and ultraviolet laser probe microanalysis inductively coupled plasma mass spectrometry in mineral analysis," *Analyst*, vol. 120, no. 5, pp. 1365–1371, 1995.